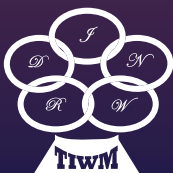


A photograph of a welding process, showing bright blue sparks and a glowing blue light emanating from a welding torch. The background is dark, making the sparks stand out.

Transactions on Intelligent Welding Manufacturing

Volume IV No. 1 2020



 Springer

The Springer logo, which consists of a stylized chess knight (horse) facing left, positioned above the word 'Springer' in a serif font.

Transactions on Intelligent Welding Manufacturing

Editors-in-Chief

Shanben Chen
Shanghai Jiao Tong University
PRC

Yuming Zhang
University of Kentucky
USA

Zhili Feng
Oak Ridge National Laboratory
USA

Honorary Editors

G. Cook, USA
K. L. Moore, USA
Ji-Luan Pan, PRC

S. A. David, USA
S. J. Na, KOR
Lin Wu, PRC

Y. Hirata, JAP
J. Norrish, AUS

T. Lienert, USA
T. J. Tarn, USA

Guest Editors

H. P. Chen, USA
J. C. Feng, PRC
H. J. Li, AUS

X. Q. Chen, NZL
D. Hong, USA
W. Zhou, SGP

D. Du, PRC
X. D. Jiao, PRC

D. Fan, PRC
I. Lopez-Juarez, MEX

Regional Editors

Asia: L. X. Zhang, PRC
America: Y. K. Liu, USA

Australia: Z. X. PAN, AUS
Europe: S. Konovalov, RUS

Associate Editors

Q. X. Cao, PRC
B. H. Chang, PRC
J. Chen, USA
H. B. Chen, PRC
S. J. Chen, PRC
X. Z. Chen, PRC
A.-K. Christiansson, SWE
Z. Q. Feng, PRC
Z. G. Li, PRC
Y. Han, PRC
X. M. Hua, PRC

Y. Huang, USA
S. Konovalov, RUS
W. H. Li, PRC
X. R. Li, USA
Y. K. Liu, USA
L. M. Liu, PRC
H. Lu, PRC
Q. H. Lu, PRC
Z. Luo, PRC
G. H. Ma, PRC
Pedro Neto, PRT

G. Panoutsos, UK
Z. X. Pan, AUS
X. D. Peng, NL
Y. Shi, PRC
S. M. Sharma, India
A. N. Siddiquee, India
J. Wu, USA
J. X. Xue, PRC
L. J. Yang, PRC
X. H. Yang, PRC
Z. S. Yu, PRC

M. Wang, PRC
S. Wang, PRC
X. W. Wang, PRC
Z. Z. Wang, PRC
G. J. Zhang, PRC
H. J. Zhang, PRC
H. Zhang, B, PRC
H. Zhang, N, PRC
L. X. Zhang, PRC
W. J. Zhang, USA

Academic Assistant Editors

J. Cao, PRC
B. Chen, PRC
Z. Y. Chen, USA
Y. S. He, PRC
Y. M. Huan, PRC
Y. Luo, PRC

N. Lv, PRC
F. Li, PRC
S. B. Lin, PRC
Y. Shao, USA
Y. Tao, PRC
J. J. Wang, PRC

H. Y. Wang, PRC
S. L. Wang, PRC
J. Xiao, PRC
J. J. Xu, PRC
Y. L. Xu, PRC
C. Yu, PRC

D. Wu, PRC
M. H. Wu, PRC
H. W. Yu, PRC
K. Zhang, PRC
W. Z. Zhang, PRC
Z. F. Zhang, PRC

Editorial Staff

Executive Editor (Manuscript and Publication):
Responsible Editor (Academic and Technical):

Dr. Yan Zhang, PRC
Dr. Jing Wu, USA

More information about this series at <https://link.springer.com/bookseries/15698>

Shanben Chen · Yuming Zhang ·
Zhili Feng
Editors

Transactions on Intelligent Welding Manufacturing

Volume IV No. 1 2020

 Springer

Editors

Shanben Chen
School of Materials Science and Engineering
Shanghai Jiao Tong University
Shanghai, China

Yuming Zhang
Department of Electrical
and Computer Engineering
University of Kentucky
Lexington, KY, USA

Zhili Feng
Oak Ridge National Laboratory
Oak Ridge, TN, USA

ISSN 2520-8519 ISSN 2520-8527 (electronic)
Transactions on Intelligent Welding Manufacturing
ISBN 978-981-19-3901-3 ISBN 978-981-19-3902-0 (eBook)
<https://doi.org/10.1007/978-981-19-3902-0>

© The Editor(s) (if applicable) and The Author(s), under exclusive license
to Springer Nature Singapore Pte Ltd. 2022

This work is subject to copyright. All rights are solely and exclusively licensed by the Publisher, whether the whole or part of the material is concerned, specifically the rights of translation, reprinting, reuse of illustrations, recitation, broadcasting, reproduction on microfilms or in any other physical way, and transmission or information storage and retrieval, electronic adaptation, computer software, or by similar or dissimilar methodology now known or hereafter developed.

The use of general descriptive names, registered names, trademarks, service marks, etc. in this publication does not imply, even in the absence of a specific statement, that such names are exempt from the relevant protective laws and regulations and therefore free for general use.

The publisher, the authors, and the editors are safe to assume that the advice and information in this book are believed to be true and accurate at the date of publication. Neither the publisher nor the authors or the editors give a warranty, expressed or implied, with respect to the material contained herein or for any errors or omissions that may have been made. The publisher remains neutral with regard to jurisdictional claims in published maps and institutional affiliations.

This Springer imprint is published by the registered company Springer Nature Singapore Pte Ltd.
The registered company address is: 152 Beach Road, #21-01/04 Gateway East, Singapore 189721,
Singapore

Editorials

This issue of the Transactions on Intelligent Welding Manufacturing (TIWM) is also a collection in part selected from the high-quality contributions recommended by “The 2020 International Conference on Robotic Welding Intelligence and Automation (RWIA’2020) and the 2021 International Workshop on Intelligentized Welding Manufacturing (IWIWM’2021)”. It includes two feature articles and three research papers.

The first featured article in this issue “Defect Detection and Process Monitoring for Wire Arc Additive Manufacturing using Machine Learning” is contributed by Haochen Mu Zhonghao Chen and Fengyang He from University of Wollongong. This paper provides an in-depth review of process monitoring approaches suitable for a Wire Arc Additive Manufacturing (WAAM) system related to defect detections. Particular focus is given to the machine learning (ML)-based monitoring systems and how they could be implemented into the WAAM process to improve the detecting accuracy reliability and efficiency.

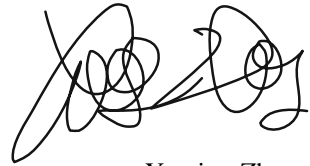
The second featured article in this issue “Research Evolution on Intelligentized K-TIG Welding” is contributed by Yanxin Cui Yonghua Shi from South China University of Technology. This paper introduces the intellectualization and improvement progress of the K-TIG welding. Many sensing techniques such as arc spectroscopic analysis and multi-information fusion are elucidated with great potential for identifying penetration states and analyzing dynamic K-TIG welding processes. The first research article “Segmentation-based Automatic Recognition for Weld Defect in Radiographic Testing Image” is contributed by Ming Zhu Xiaohua Chen and Hulong Zhang all from Lanzhou University of Technology. This paper proposes a defect recognition algorithm based on image segmentation which was divided into three stages: image preprocessing, weld segmentation, and defect segmentation. The results of the study show that the extracted parameters can reflect the shape features of actual defects.

The second research paper entitled “MLD Classification Model of Visual Features of Multi-layer and Multi-pass Molten Pool during Robotic MAG Welding of Medium-thick Steel Plates” is contributed by Hao Zhou Shanben Chen and Huabin Chen from Shanghai Jiao Tong University. The Geodesic active contour

model (GAC) method is used for the molten pool image (MPI) in the multi-layer and multi-pass welding process, and the MLD classification model is established. The experimental results show that the image segmentation method based on GAC can effectively obtain the edge of MAG weld pool. The characteristics of weld pool are exactly corresponding to the seven types of multi-layer and multi-pass welding.

The third research paper titled “Deep Learning Based Robot Detection and Grinding System for Veneer Defects” is contributed by a research team from East China University of Science and Technology. This paper proposes the method using industrial robot combined with vision detection system. Based on the object detection network RetinaNet, the detection model is trained to detect the defects of different categories in the whole veneer. The pixel coordinates will be transformed into robot coordinates, and PLC uses these coordinate values to control the robot for grinding. The results show that the model has high recognition accuracy in the tested veneer data.

This issue of TIWM shows the new perspectives and developments in the field of intelligent welding research as well as the topics related to the RWIA’2020 and IWIWM’2021 conferences. The publication of this issue will certainly give readers new inspiration as we always hope so.

A handwritten signature in black ink, consisting of several loops and strokes, positioned above the name Yuming Zhang.

Yuming Zhang

Contents

Feature Articles

Defect Detection and Process Monitoring for Wire Arc Additive Manufacturing Using Machine Learning	3
Haochen Mu, Zhonghao Chen, Fengyang He, Yuxing Li, Chunyang Xia, Philip Commins, and Zengxi Pan	

Research Evolution on Intelligentized K-TIG Welding	23
Yanxin Cui and Yonghua Shi	

Research Papers

Segmentation-Based Automatic Recognition for Weld Defect in Radiographic Testing Image	43
Ming Zhu, Xiaohua Chen, Hulong Zhang, Yu Shi, and Ding Fan	

MLD Classification Model of Visual Features of Multi-layer and Multi-pass Molten Pool During Robotic MAG Welding of Medium-Thick Steel Plates	56
Hao Zhou, Yinshui He, Huabin Chen, and Shanben Chen	

Deep Learning Based Robot Detection and Grinding System for Veneer Defects	82
Xuewu Wang, Zhongwang Zhang, and Huafeng Liu	

Author Index	97
---------------------------	----

Feature Articles



Defect Detection and Process Monitoring for Wire Arc Additive Manufacturing Using Machine Learning

Haochen Mu, Zhonghao Chen, Fengyang He, Yuxing Li, Chunyang Xia, Philip Commins, and Zengxi Pan^(✉)

School of Mechanical, Materials, Mechatronic and Biomedical Engineering, University of Wollongong, Wollongong, NSW 2522, Australia
zengxi@uow.edu.au

Abstract. Wire Arc Additive Manufacturing (WAAM) is a promising manufacturing technology that has been used to build medium to larger-sized components. The recent progress of Artificial Intelligence (AI) technology has led to Machine Learning (ML) algorithms being widely implemented for modeling, control, monitoring, and simulation processes in WAAM. However, current defect detection systems are limited due to the types of detectable defects, and a real-time micro-defect detection system is yet to be developed. This paper aims to provide an in-depth review of process monitoring approaches suitable for a WAAM system related to defect detections. Particular focus is given to the ML-based monitoring systems, and how they could be implemented into the WAAM process to improve the detecting accuracy, reliability, and efficiency. The paper concludes by discussing the current challenges and future work for developing a real-time monitoring system.

Keywords: WAAM · Additive manufacturing · Defect detection · Process monitoring · Machine learning

1 Introduction

Additive Manufacturing (AM), which is also known as the 3D printing technique, is an emerging manufacturing technology that usually fabricates parts layer-by-layer. As a sub-category of metallic AM process, Wire Arc Additive Manufacturing (WAAM) is a wire-feed system that utilizes metal wire and electrical arc as the deposition material and heating source, respectively [1] (as illustrated in Fig. 1.). WAAM is a more cost-effective manufacturing technique that features a higher buy-to-fly ratio, lower equipment costs compared with other wire-feed, powder-feed, or powder-bed metallic AM systems [2]. Additionally, being capable of manufacturing components with full density is also a major advantage for structural applications [3].

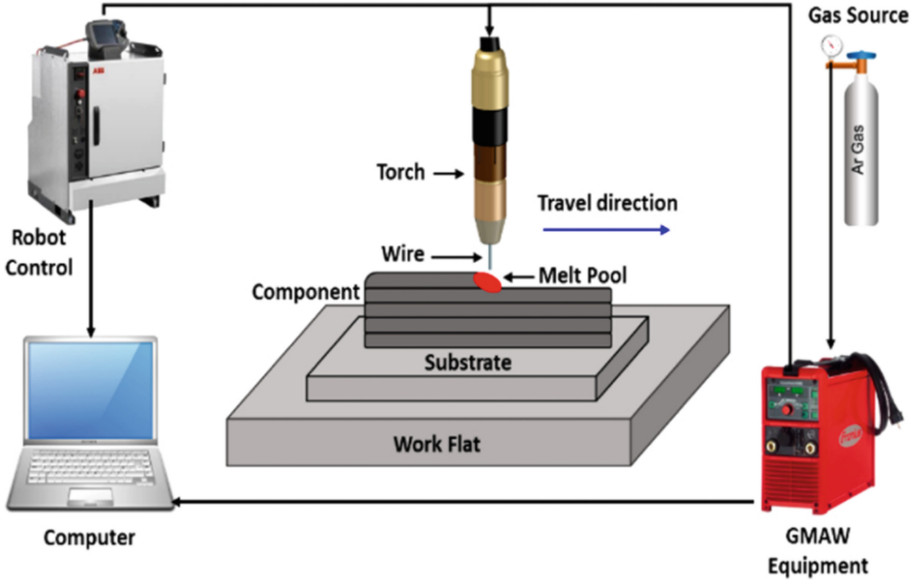


Fig. 1. Schematic of the WAAM system [4].

The research history of WAAM can be traced back to 2010 and presents an exponential growth in research interest since 2016, as shown in Fig. 2. The development of WAAM can be classified into three stages. In stage one (from 2010 to 2013), the research objectives were highly targeted to the welding technology, including material properties [5], deposition modeling [6], and process analysis [7]. In stage two (from 2014 to 2018), automation has become a focused research topic for WAAM. More technologies and areas (i.e., control theory [8], modeling [9], monitoring [10], and simulation [11]) were involved to develop an automatic WAAM system. In stage three (from 2019 till present), as the Artificial Intelligence (AI) revolution has impacted the structure of the modern industry, applications of ML and AI algorithms have a boosted development in WAAM. So far, WAAM has been widely applied to the manufacture of large components in aerospace [12], shipbuilding [13], and defense industries.

Several issues remain and inhibit WAAM from widespread commercial adoptions. Multiple types of defects are commonly found in WAAM, including geometric inaccuracy, residual stress, porosity. Traditional approaches have been developed to detect these defects. For example, IR camera [14], eddy current [15], ultrasonic [16, 17], x-ray [18, 19], microscopy [20], etc. Those research efforts provide valuable reference and inspiration for future work, however, the processing latency and low cost-efficiency are still limiting the online monitoring of WAAM.

ML is an emerging technology and is commonly utilized for real-time data processing. Compared to traditional physics-based or data-based models, ML-based models can significantly accelerate the processing speed [21]. Therefore, this study aims to provide

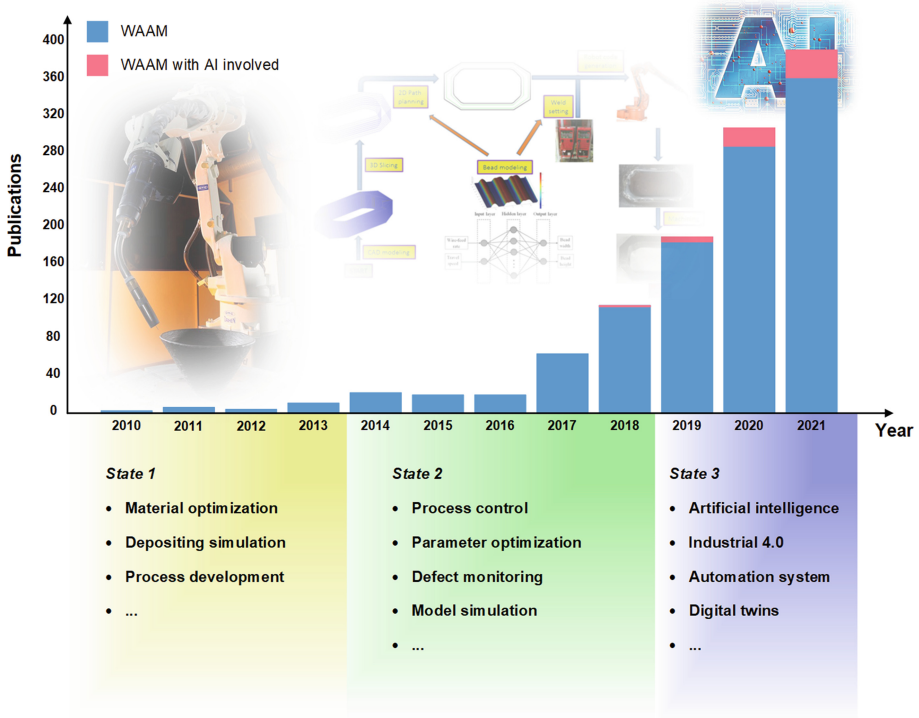


Fig. 2. Publication trend and percentage of publications in research topics of WAAM.

inspiration, knowledge, and strategy for a defect detecting and process monitoring system using ML. Additionally, ML applications in other metallic AM monitoring processes are also introduced and could be adopted in the WAAM process.

This paper is organized as follows: Sect. 2 reviews the defects in WAAM processes. Section 3 introduces the current applications of ML in the WAAM system from modeling, control, and simulation aspects. Section 4 reviews the state-of-the-art ML-based defect detection approaches in AM. Section 5 summarizes the challenges and future work for a monitoring system for WAAM. Section 6 concludes this paper.

2 Defects in WAAM Systems

The common defects in WAAM include cracks, delamination, porosity, deformation, residual stress, oxidation, and poor surface finish. As shown in Fig. 3., the types of defects are strongly correlated to the deposition material [22]. In this section, the generation, influence, and control strategies of these common defects will be discussed.

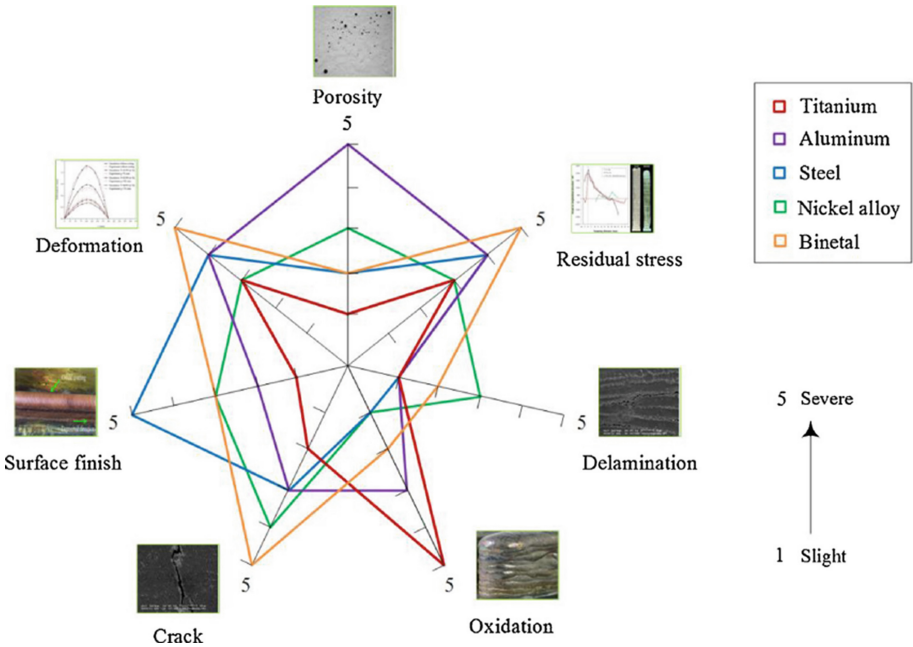


Fig. 3. The correlation between deposition materials and defects in WAAM processes [22].

2.1 Crack and Delamination

Crack and delamination are common defects that are present in all AM manufactured products. In WAAM, cracks can be categorized as solidification cracks and grain boundary cracks. Solidification cracks are mainly caused by the obstruction of solidified grain flow or the high strain in the molten pool, while grain boundary cracks are often generated by the differences between boundary morphology and potential precipitate formation or dissolution. The expansion of cracks is uncontrollable and can result in fractures of the component. To solve this, current technical solutions include ultrasonic vibration, electromagnetic stirring, magnetic arc oscillation, and inoculation [23].

Delamination is generally caused by the insufficient re-melting of the previously deposited layer or the incomplete melting of the currently deposited layer. However, this macro defect cannot be repaired by post-processing treatments, which eventually leads to a lack of fusion. Thus, pre-processing treatments need to be considered before each layer's deposition process to avoid delamination, such as preheating [22]. Examples of cracks and delamination are shown in Fig. 4.

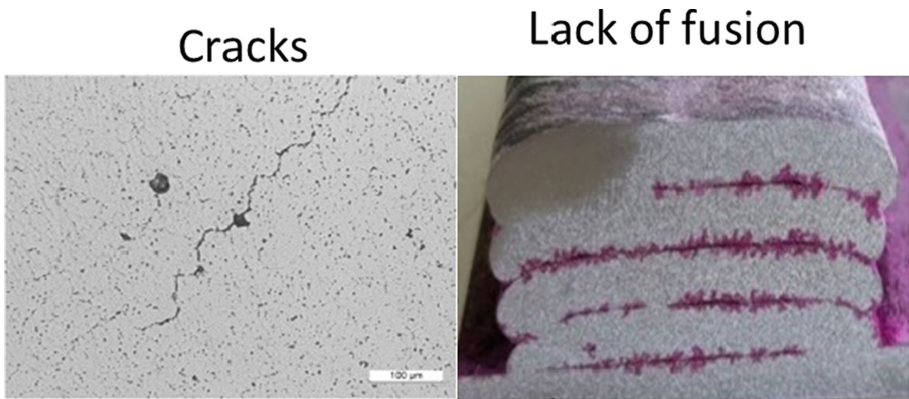


Fig. 4. Examples of cracks [24] and delamination [15].

2.2 Porosity

Porosity in AM can be classified as raw material-induced pores and process-induced pores. During the deposition, the moisture, oil, and other hydrocarbons on the surface of the feed wire can be combined into the molten pool, which finally will lead to porosity. The process-induced pores are caused by the dramatic change of temperature field and incorrect or unstable process parameters, such as metal transfer mode and heat input [25]. Porosity can damage the manufactured part and result in low mechanical strength. Besides, the accumulation of pores can lead to micro-cracks and macro-voids, as shown in Fig. 5.

To control porosity, it is important to clean the feedstock and deposited layers. Adjusting process parameters such as shielding gas flow, metal transfer mode, and heat input is also found to be helpful. For the post-processing treatments, the inter-layer rolling and re-melting technology can also decrease the presence of pores [23].

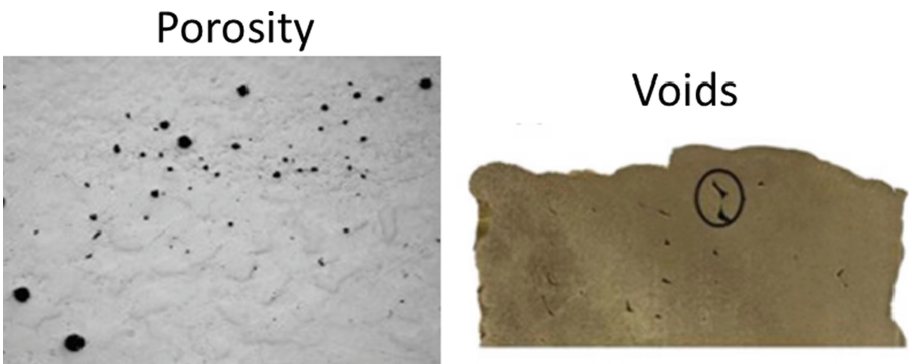


Fig. 5. Examples of porosity [26] and voids [27].

2.3 Deformation and Residual Stress

Deformation and residual stress are inherent defects that cannot be avoided. Various deformation types exist in WAAM, including longitudinal and transverse shrinkage, bending distortion, angular distortion, and rotational distortion. During repeated melting and cooling processes, deformation and residual stress are generated and accumulated due to the thermal expansion and shrinkage of the component. When the external load on the baseplate is removed after finishing the deposition, the residual stress remains and will significantly influence the fatigue performance, especially for thin-wall structures [22]. Current approaches to control the deformation and residual stress include adjusting path-planning, depositing additional material, post-process milling, vertical and side rolling, intermediate stress relief anneal, and active interpass cooling [23]. An example of thermal distortion is shown in Fig. 6.

Thermal distortion

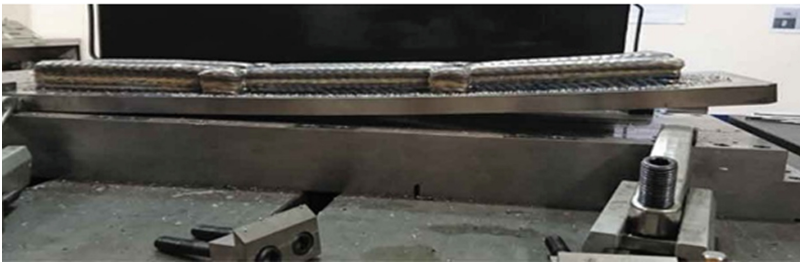


Fig. 6. Example of thermal distortion [28].

2.4 Oxidation and Poor Surface Finish

Oxidation is a significant defect, however, it receives less attention than porosity and cracks. The formation of oxidation is strongly related to the properties of the deposition material. For a highly reactive element that has a strong binding affinity for oxygen, such as aluminum, it is impossible to avoid oxidation during welding. The high melting temperature of oxidation film on the surface of the deposited bead can affect the welding arc, eventually leading to pores, cracks, delamination, and poor surface finish, as shown in Fig. 7. Oxidation can be reduced by controlling the shielding gas flow. Since an increase in gas velocity can increase the mixing of the shielding gas with the atmosphere, a proper range of gas flow must be controlled for different materials [29].

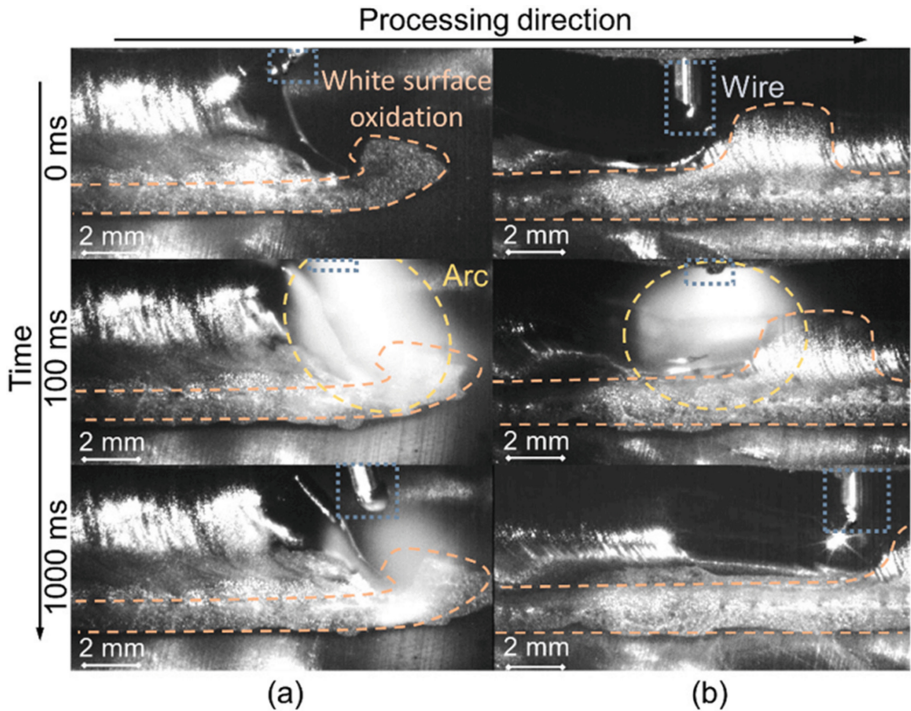


Fig. 7. High-speed images of the processing zone in the (a) first and (b) second layer which show the white surface oxidation (marked orange), the arc (marked yellow), and the wire (marked blue) [29].

3 Machine Learning Applications in WAAM

ML is a data-based modeling technology that aims to reveal relationships in a system with unknown physics. Typically, ML can be categorized into 4 groups: supervised learning, unsupervised learning, semi-supervised learning, and reinforcement learning [30]. The difference between these groups is whether the training dataset is labeled. For supervised learning, each training point contains one label, thus the model is designed to predict input features for desired outputs [31]. In contrast, training points in an unsupervised learning algorithm do not contain any label, so this type of model is often used to detect hidden or unknown relationships among the data [32]. The semi-supervised learning algorithm is a combination of both supervised learning and unsupervised learning. The presence of a small set of labeled data can significantly improve the detecting performance [33]. As for reinforcement learning, it iteratively gains experience by interacting with the monitoring environment, thus the optimal solution can be achieved with hundreds of iterations [34]. As shown in Fig. 8., ML applications have covered many areas in WAAM, including modeling, control, simulation, and detection. In this section, the ML applications in those aspects will be reviewed.

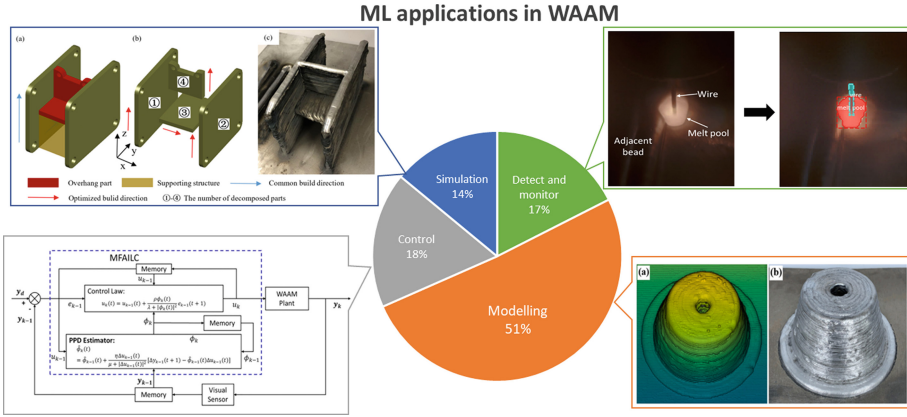


Fig. 8. ML applications in WAAM.

3.1 Modeling

Modeling is a fundamental application of ML. In WAAM, modeling tasks include geometrical models, physical models, and process models. The most frequently used model is the geometrical model, which is utilized to predict the bead geometry based on the welding inputs. For example, Tang et al. used a deep learning algorithm to model the bead geometry [35]. Barrionuevo et al. compared the geometrical modeling accuracy of different ML-based regression models [36]. Yaseer and Chen implemented Random Forest (RF) and Multilayer Perceptron (MLP) to model the surface roughness of deposited bead based on welding parameters [37]. The physical model is an important application as well because it can effectively reveal the welding physics or the product properties. For example, Wu et al. utilized RF and Artificial Neural Network (ANN) to model the residual stress and analyze the significance of input influential variables [38]. Maurya et al. used the ANN model to correlate the hot deformation process parameters and flow stress [39].

Process models are used to generate process parameters based on existing welding examples. For example, Hu et al. combined genetic algorithm (GA) and forward ANN (FANN) to predict the welding parameters based on desired bead geometry [40]. Compared to the traditional modeling technologies such as physics-based models [41] and regressive models [42], ML-based models have the benefits of accuracy, reliability, and flexibility. The model accuracy and reliability are improved because of the support of a relatively large training dataset, and the flexibility is improved because of the ML's ability that can learn from iterations.

3.2 Control

The ML-based controller is an advanced application that usually is combined with ML-based models. Similar to conventional controllers, ML-based controllers are generally used to achieve geometrical control based on single or multiple welding inputs. For example, Dharmawan et al. proposed a reinforcement learning framework to achieve

in-situ geometric control and model learning for multi-layer and multi-bead processes [43]. Xia et al. developed an ML-based model-free adaptive iterative learning control to solve the geometrical inaccuracy of thin-wall structures [44]. Kulkarni et al. controlled the deposition speed based on welding circumstances using an unsupervised learning algorithm [45]. Wang et al. used an EPNet algorithm to control the bead width based on the real-time weld pool image [46]. Through all these applications, it has been proved that the ML-based controller greatly improves the control adaptiveness and flexibility compared to traditional controllers (for example PID [47] and MPC [48]).

3.3 Simulation

The simulation process can be regarded as a combination of model and controller, where the controller generates the welding inputs, while the model predicts the virtual feedbacks based on the outputs from the controller, thus the future system can be predicted. For example, Nalajam and Varadarajan developed a simulation system based on the Convolutional Neural Network (CNN) and Long Short-Term Memory (LSTM) to predict the melt pool temperature [49]. Ding et al. built a backward model using the Support Vector Machine (SVM) to predict the bead geometries of the whole deposition process [50].

ML plays an important role in the simulation process. Though traditional physics-based simulations can achieve higher accuracy, they are significantly time-consuming and cost-sensitive. In contrast, ML-based simulations offer a more flexible solution to adjust the balance between time and accuracy depending on the simulation environment. Furthermore, the combination of ML and physics-based models [51] can significantly reduce processing time while maintaining simulation accuracy.

4 ML-Based Monitoring Systems

To date, defect detection algorithm plays an important role in the monitoring of AM processes. For WAAM, samples from the deposition part are usually required for traditional defect detection approaches, such as x-ray [18, 19] and microscopy [20], which are destructive to the manufactured part. To develop an online monitoring system, sensors used in nondestructive detecting approaches, such as IR camera [14], eddy current [15], and ultrasonic [16, 17], are generally considered. In this section, defect detection approaches using ML algorithms will be introduced and classified according to the sensor used.

4.1 Defect Detection Using Welding Electrical Signal

The voltage and current waveforms of the welding process are important because they imply heat input and welding physics, though they are not often collected as geometric data. In the research from Li et al. [52], an incremental learning model was developed to detect defects using electrical signals. The welding electrical data are collected by voltage and current sensors. The collected signals are then sent to the pre-processing procedure, where the features are extracted and the noise is reduced, as shown in Fig. 9.

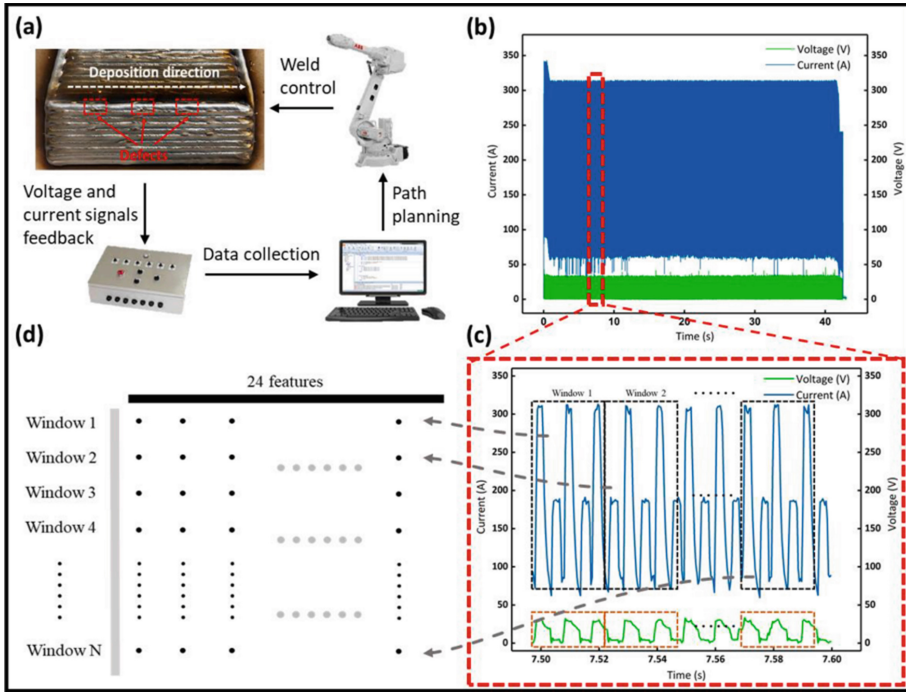


Fig. 9. Electrical signal pre-processing (a) data acquisition. (b) raw data of a single weld bead. (c) rolling windows split data into data pieces and then (d) each data piece will be extracted to 24 features as a representation of a data window [52].

Finally, to simplify the overall statistical features, a score evaluation algorithm is used to summarize and provide overall scores, which are used as the input of the incremental learning model.

For the model training process, an SVM is used to identify the defects. The goal is to obtain a linear score function of the SVM, and the function parameters are solved by the Stochastic Gradient Descent (SGD) optimizer through iterations during training. Li et al. achieved incremental learning by continuously feeding new data into the partially trained model, thus the model will be continually updated using the knowledge acquired in previous runs. Consequently, the user only needs to manually identify a relatively small dataset of defects during training (as shown in Fig. 10.) and the defects can be automatically detected during welding. The feasibility of the model is evaluated based on the three measures: recall, precision, and F1 score, while the higher value refers to better performance.

The result of practical experiments presents the high reliability and precision of this incremental learning-based in-situ defect detection approach. The F1 score reaches above 90% for all predicting tasks (that is, normal, arc on, arc off, and weld pool shift). Another advantage of this approach is flexibility: the training of the incremental learning model is based on a relatively small dataset, thus it is possible to detect more defects simultaneously, additionally, more cost-effective for rare materials.

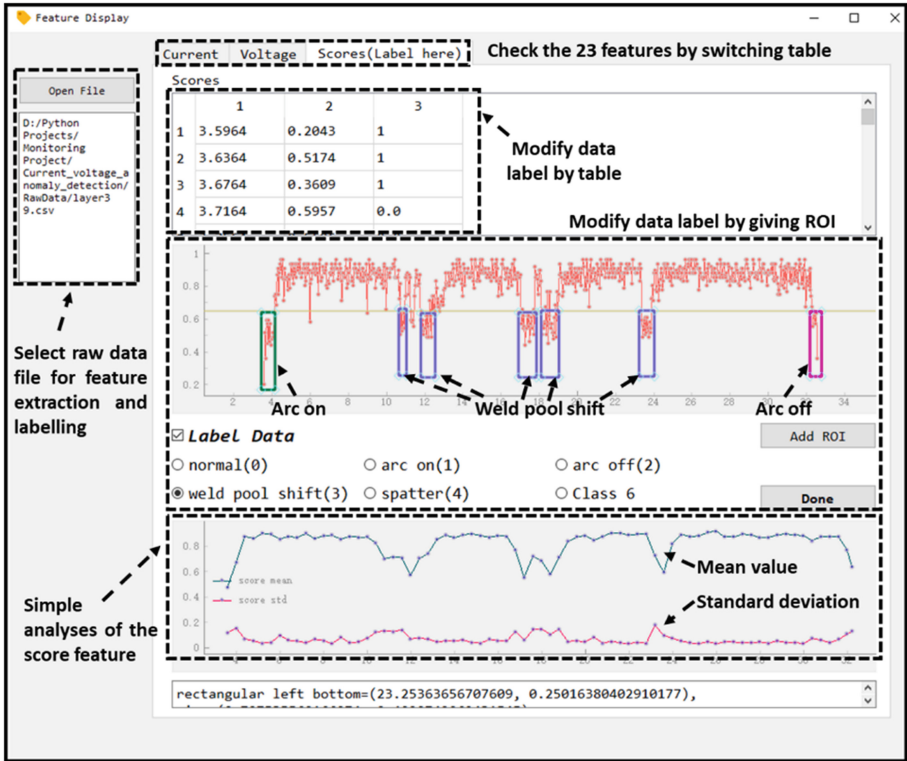


Fig. 10. The GUI that used for training the SVM model [52].

The unsupervised ML technology also presents a remarkable performance in the research from Reisch et al. [53]. The monitoring system detects defects by estimating the error likelihood, which is calculated based on the difference between predicted (reconstructed) inputs and in-situ monitored input signals. Generally, different ML models are selected based on different inputs. In this example, LSTM and one-dimensional convolutional (Conv1D) models are utilized for current and voltage predictions, respectively. The model parameters are optimized with Bayesian Hyperparameter Optimization (HPO), and the training process is completed using unlabelled data of a previous additive layer without forced anomalies. During the monitoring process, the predicted current and voltage data are compared with original data, and the prediction error is used to detect defects, as shown in Fig. 11. Results from practical experiments illustrate a remarkable detecting delay, which is less than 30ms, and a reliable loss, which is less than 0.011 on average.

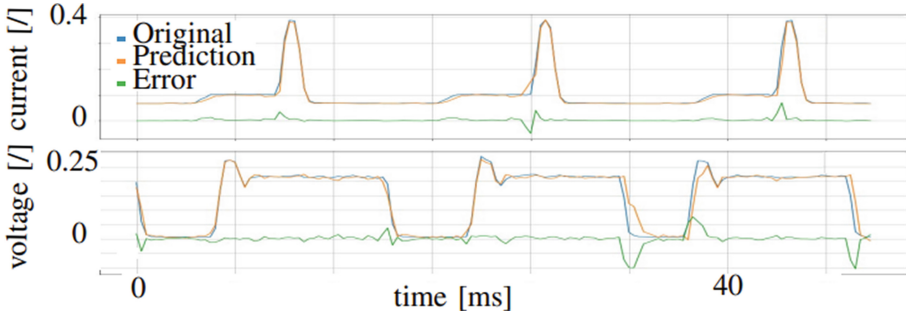


Fig. 11. Normalized not synchronized current and voltage time series (blue), their predictions (orange), and the resulting error distances (green) [53].

4.2 Defect Detection Using Computer Vision

In recent years, the images of the welding molten pool are monitored to detect defects. With the development of ML and image processing techniques, online image-based defect detection approaches are preferred due to their high reliability and flexibility. For example, using a CCD camera to capture the real-time formation of one layer’s deposition, then feed to neural networks (for example, YOLOv3 model, PredNet [54], and regression network [55]) to detect and classify the defects. For the training phase of the model, the images with defects are manually collected and labeled, and hyperparameter tuning is utilized to find the best performance model under different anchor settings. Results (as shown in Fig. 12.) present the practical performance of this approach. This online monitoring approach can detect surface defects instantly and provide theoretical references and inspiration for the research of online repair processes.

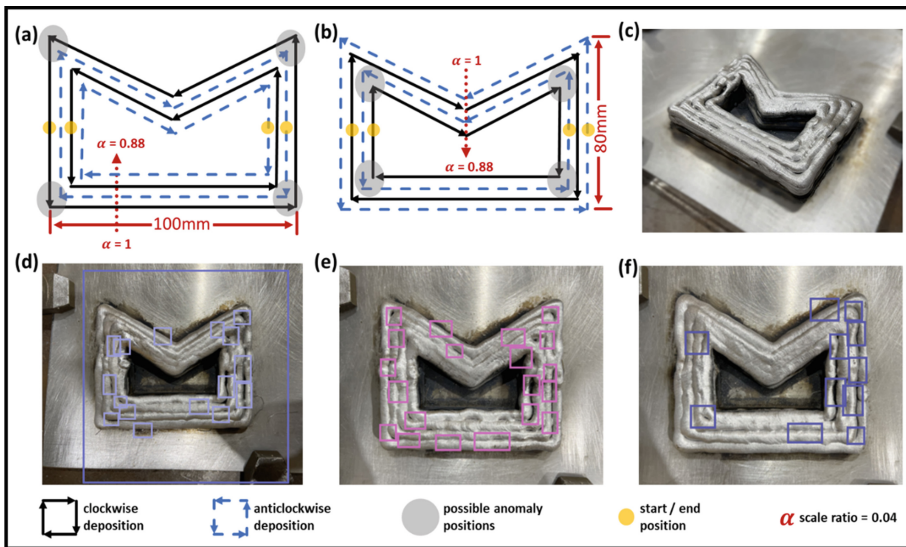


Fig. 12. (a)–(b): path planning, neighboring contours are welded in clockwise and anticlockwise directions; (c): real photo after 8 layers depositions; (d)–(f): Different detection results on different layers.

In another example, He et al. [20] developed a detection and classification system to monitor the surface defects using a Cost-Sensitive Convolutional Neural Network (CSCNN). The surface information is captured based on the Magneto-Optical Imaging (MOI) technique. Compared to the CCD camera, MOI can effectively detect defects on both surface and subsurface, while being more costly. The training of CSCNN is based on the original Magneto-Optical (MO) images, and the gradient descent training method is used to calculate the model parameters. The whole structure of the CSCNN classification model is shown in Fig. 13. For practical experiments, the prediction accuracy is above 85% when classifying different defects and notably reaches 97% when identifying no defect.

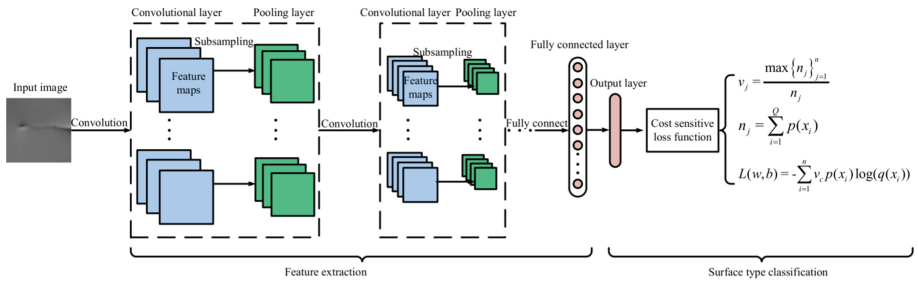


Fig. 13. Structure of the CSCNN classification model [20].

As for the unsupervised learning applications, an autoencoder is also utilized to detect anomalies in the work of Reisch et al. [53]. Similar to the unsupervised learning approach introduced in Sect. 4.2, this approach calculates the reconstruction error between the autoencoder reconstructed image, and the corresponding original image taken by the welding camera, as shown in Fig. 14. The training dataset only contains healthy data thus when an anomaly occurred, the autoencoder needs to reconstruct a new image, resulting in a worse fit. Results present a reliable detecting accuracy (average loss less than 0.002) with a relatively high predicting delay (more than 340 ms).

The sensor used for the defect detection algorithm is not limited to the cameras. Nalam-jam et al.[56] developed an offline porosity detection system based on microstructural images. The optical micrographs are taken by optical microscopy first, then processed by Gabor filters for feature extraction. Three classifiers are tested and compared in this approach: k-means, SVM, and RF. Results show that RF presents the highest classification accuracy of 99.49%, followed by SVM with an accuracy of 98.75%. One drawback of this approach is destructive testing, nevertheless, the high performance of ML algorithms proves to make ML a feasible technique for real-time porosity analysis.

4.3 Defect Detection Using the 3D Laser Scanner

As geometric inaccuracy is the most significant and commercial defect that appears in metallic AM processes, a straightforward detecting method is through geometric scanners. For example, Huang's research team [57] developed a 3D laser profilometer inspection (3D-LPI) system based on real-time feedback from the laser scanner. The

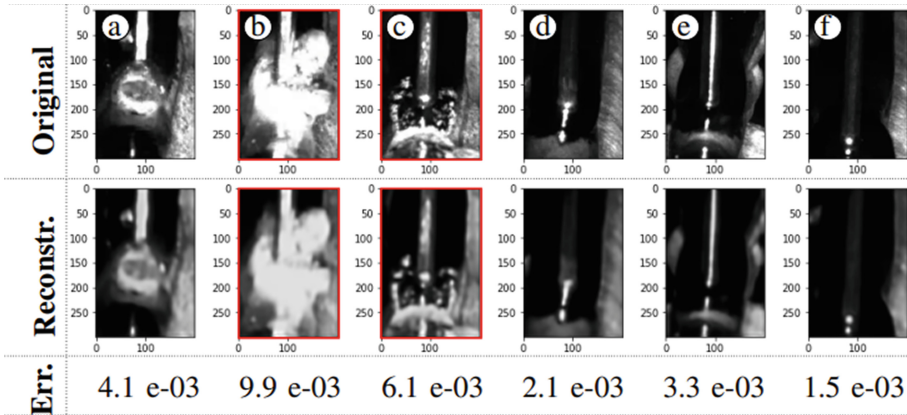


Fig. 14. Original/Reconstructed images of welding camera and corresponding reconstruction error; images of the abnormal process marked in red [53].

monitoring process can be divided into the following procedures: scanning, point cloud pre-processing, and detection.

During the manufacturing process, the deposited surface is scanned after finishing one layer of deposition. Then, the raw point cloud is generated and sent for the pre-processing step. The pre-processing algorithm aims to reduce noise, extract the deposited part, calculate the heightmap, and convert the geometric data into one topography image for each layer, as shown in Fig. 15. The detection process aims to detect and classify surface defects. In their work, 12 features (intensity, maximum, minimum, contrast, mean, standard deviation, entropy, flatness, homogeneity, skewness, distance to boundary, and Laplace filtered) and 4 labels (normal, bulgy, dented, and pores) are used for training the SVM model.

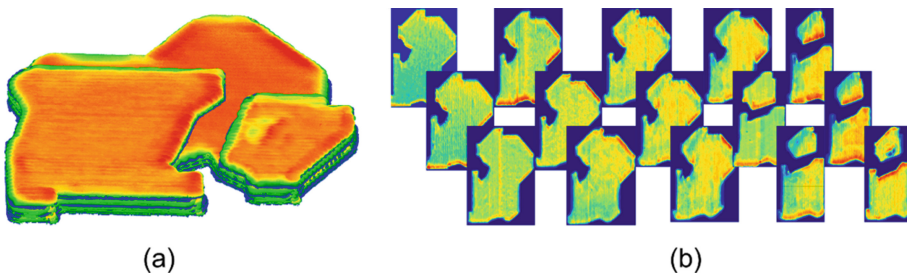


Fig. 15. The measurement results (a) The layerwise point cloud of the deposited object (b) layerwise topography image in pseudocolor [57].

For the experiment results, the proposed 3D-LPI system can effectively identify the labeled defects, as shown in Fig. 16. However, the resolution is the main hindrance to detecting small defects such as pores. To conclude, the proposed 3D-LPI system is capable of locating and identifying the surface defects during the deposition process of

medium to large components. Additionally, the balance between resolution and detecting accuracy is one of the main concerns when designing such a system.

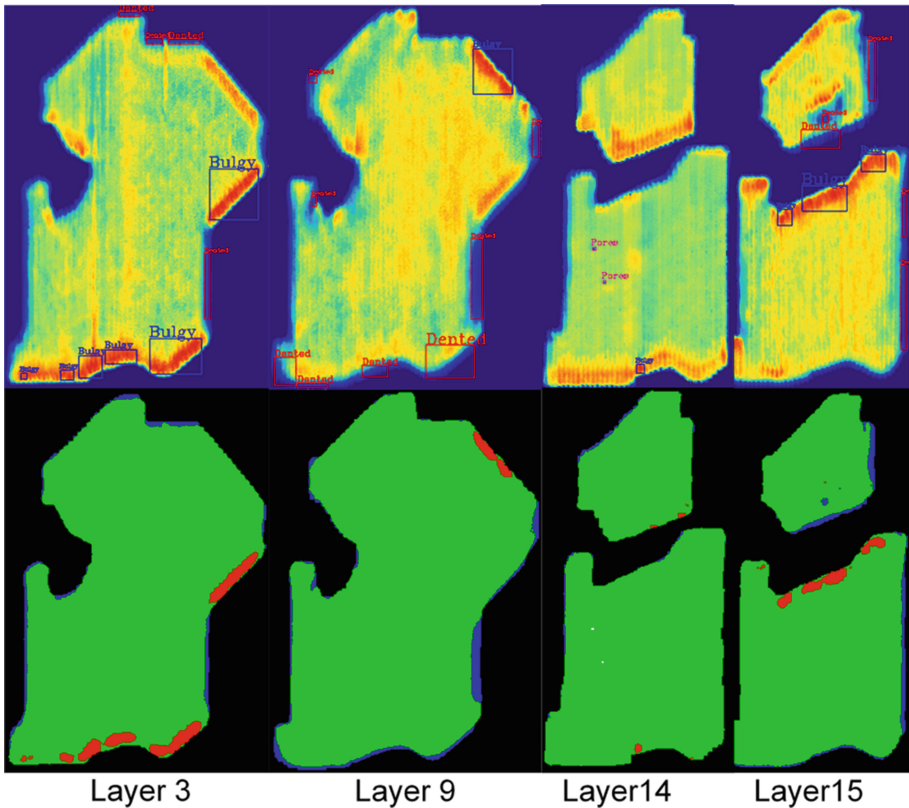


Fig. 16. Defects detection results, the first row showed the classification results of pixels, the second row showed identification results of defects on the pseudocolor topography [57].

4.4 Other Defect Detection Methods

Despite traditional sensors, some research efforts focus on investigating the combination of defect detection and new sensors. For example, in the online monitoring system proposed by Surovi et al. [58], acoustic sensors are used for detecting irregularities during the deposition process. The author provided three acoustic feature-based frameworks: Principal Component Analysis (PCA) + K-Nearest Neighbors (KNN), Mel Frequency Cepstral Coefficients (MFCC) + Neural Network (NN), and Mel Frequency Cepstral Coefficients (MFCC) + CNN. Results show that the combination of PCA and KNN can perform the best detecting accuracy. This attempt can provide theoretical basics and inspiration for the sensor used in monitoring systems.

5 Challenges and Future Work

In this section, the current challenges and future work for developing a monitoring system for WAAM will be summarized and categorized into two aspects: ML-based algorithm performance and sensor fusion.

5.1 Accuracy, Flexibility, and Efficiency of Detection

The main concern for developing a monitoring system is the ML-based algorithm performance, which can be categorized as detection accuracy, flexibility, and efficiency. Accuracy refers to whether different defects can be identified during the manufacturing process. Flexibility refers to whether defects can be detected in various welding environments. Efficiency refers to the time and cost of the detection process. During the real-time monitoring process, various defects need to be detected simultaneously while minimizing the detection delay. Consequently, selecting a proper training dataset and ML-based model, as well as designing the model iteration process, requires more future work.

5.2 Sensor Integration and Signal Data Fusion

Sensor fusion can present a better understanding of a physical system through combining multiple data sources, thus providing more consistent, accurate, and reliable feedback data. In WAAM, various sensors can be integrated (e.g., thermal, geometrical, voltage & current) to create a multidimensional dataset for describing the welding process. Sensors should be integrated into modules to solve specific detecting tasks. For example, the detection of oxidation is necessary for the welding with titanium wire, while less important for steel and nickel alloy wires. However, ML-based data fusion algorithms are compulsory to establish the connection between detection modules.

Another research problem for sensor fusion is that most in-situ sensors cannot monitor the microstructures of the deposited part, and the welding physics such as residual stress. Therefore, using ML to find the relationship between microstructure, welding physics and those detectable signals (e.g., arc, heat, and molten pool) is a necessary step to sensor fusion, which can be a future research interest.

6 Conclusion

In this study, a comprehensive review of research efforts in defects, ML applications, and ML-based defect detecting approaches in WAAM were provided. Common defects include cracks, delamination, porosity, deformation, residual stress, oxidation, and surface finish, then the formation, impact, and solution of these defects were reviewed. The background of ML applications in modeling, control, and simulation aspects was introduced, then the state-of-the-art ML-based defect detection approaches are discussed in detail and categorized by sensor sources. Challenges and future work are discussed from two aspects: ML-based algorithm performance and sensor fusion.

Acknowledgments. This work was supported in part by China Scholarship Council under Grant 202108200021, 202008200004.

References

1. Frazier, W.E.: Metal additive manufacturing: a review. *J. Mater. Eng. Perform.* **23**(6), 1917–1928 (2014). <https://doi.org/10.1007/s11665-014-0958-z>
2. Reischa, R., Hauser, T., Kamps, T., Knoll, A.: Robot based wire arc additive manufacturing system with context-sensitive multivariate monitoring framework. In: 30th International Conference on Flexible Automation and Intelligent Manufacturing (FAIM2021), Athens (2021)
3. Taşdemir, A., Nohut, S.: An overview of wire arc additive manufacturing (WAAM) in shipbuilding industry. *Ships Offshore Struct.* **16**(7), 797–814 (2021)
4. Xia, C., et al.: A review on wire arc additive manufacturing: monitoring, control and a framework of automated system. *J. Manuf. Syst.* **57**, 31–45 (2020)
5. Wang, F., Williams, S., Colegrove, P., Antonysamy, A.A.: Microstructure and mechanical properties of wire and arc additive manufactured Ti-6Al-4V. *Metall. Mater. Trans. A* **44**(2), 968–977 (2013)
6. Xiong, J., Zhang, G., Gao, H., Wu, L.: Modeling of bead section profile and overlapping beads with experimental validation for robotic GMAW-based rapid manufacturing. *Robot. Comput.-Integr. Manuf.* **29**(2), 417–423 (2013)
7. Ding, J., et al.: Thermo-mechanical analysis of wire and arc additive layer manufacturing process on large multi-layer parts. *Comput. Mater. Sci.* **50**(12), 3315–3322 (2011)
8. Xiong, J., Yin, Z., Zhang, W.: Closed-loop control of variable layer width for thin-walled parts in wire and arc additive manufacturing. *J. Mater. Process. Technol.* **233**, 100–106 (2016)
9. Ding, D., Pan, Z., Cuiuri, D., Li, H.: A multi-bead overlapping model for robotic wire and arc additive manufacturing (WAAM). *Robot. Comput. Integr. Manuf.* **31**, 101–110 (2015)
10. Lopez, A., Bacelar, R., Pires, I., Santos, T.G., Sousa, J.P., Quintino, L.: Non-destructive testing application of radiography and ultrasound for wire and arc additive manufacturing. *Addit. Manuf.* **21**, 298–306 (2018)
11. Bai, X., et al.: Numerical analysis of heat transfer and fluid flow in multilayer deposition of PAW-based wire and arc additive manufacturing. *Int. J. Heat Mass Transfer.* **124**, 504–516 (2018)
12. Uriondo, A., Esperon-Miguez, M., Perinpanayagam, S.: The present and future of additive manufacturing in the aerospace sector: a review of important aspects. *Proc. Inst. Mech. Eng. Part G: J. Aerosp. Eng.* **229**(11), 2122–2147 (2015)
13. Taşdemir, A., Nohut, S.: An overview of wire arc additive manufacturing (WAAM) in shipbuilding industry. *Ships Offshore Struct.* **16**, 1–18, 2020
14. Bourlet, C., Zimmer-Chevret, S., Pesci, R., Bigot, R., Robineau, A., Scandella, F.: Microstructure and mechanical properties of high strength steel deposits obtained by Wire-Arc additive manufacturing. *J. Mater. Process. Technol.* **285**, 116759 (2020)
15. Bento, J.B., Lopez, A., Pires, I., Quintino, L., Santos, T.G.: Non-destructive testing for wire + arc additive manufacturing of aluminium parts. *Addit. Manuf.* **29**, 100782 (2019)
16. Zeng, Y., Wang, X., Qin, X., Hua, L., Liu, G., Guan, S.: Laser ultrasonic inspection of defects in wire arc additive manufactured samples with different surface profiles. *Measurement* **188**, 110597 (2022)
17. Zimmermann, R., et al.: Multi-layer ultrasonic imaging of as-built wire + arc additive manufactured components. *Addit. Manuf.* **48**(Part A), 102398 (2021)
18. Fang, X., et al.: Additive manufacturing of high performance AZ31 magnesium alloy with full equiaxed grains: Microstructure, mechanical property, and electromechanical corrosion performance. *J. Mater. Process. Technol.* **300**, 117430 (2022)
19. Chabot, A., Laroche, N., Carcreff, E., Rauch, M., Hascoët, J.-Y.: Towards defect monitoring for metallic additive manufacturing components using phased array ultrasonic testing. *J. Intell. Manuf.* **31**(5), 1191–1201 (2019). <https://doi.org/10.1007/s10845-019-01505-9>

20. He, X., Wang, T., Wu, K., Liu, H.: Automatic defects detection and classification of low carbon steel WAAM products using improved remanence/magneto-optical imaging and cost-sensitive convolutional neural network. *Measurement* **173**, 108633 (2021)
21. Wu, B., et al.: A review of the wire arc additive manufacturing of metals: properties, defects and quality improvement. *J. Manuf. Process.* **35**, 127–139 (2018)
22. Chen, X., et al.: A review on wire-arc additive manufacturing: typical defects, detection approaches, and multisensor data fusion-based model. *Int. J. Adv. Manuf. Technol.* **117**(3–4), 707–727 (2021). <https://doi.org/10.1007/s00170-021-07807-8>
23. Horgar, A., Fostervoll, H., Nyhus, B., Ren, X., Eriksson, M., Akselsen, O.: Additive manufacturing using WAAM with AA5183 wire. *J. Mater. Process. Technol.* **68–74**, 259 (2018)
24. Derekar, K.S.: A review of wire arc additive manufacturing and advances in wire arc additive manufacturing of aluminium. *Mater. Sci. Technol. (U. K.)* **34**(8), 895–916 (2018)
25. Ryan, E., Harley, K., Sabin, T., Watts, J., Whiting, M.: Relationship Between Porosity and Surface Deposit Coverage for Wire and Arc Additive Manufactured Aluminium Alloy 2319 (2018)
26. Cui, J., Yuan, L., Commins, P., He, F., Wang, J., Pan, Z.: WAAM process for metal block structure parts based on mixed heat input. *Int. J. Adv. Manuf. Technol.* **113**(1–2), 503–521 (2021). <https://doi.org/10.1007/s00170-021-06654-x>
27. Xu, F., et al.: Realisation of a multi-sensor framework for process monitoring of the wire arc additive manufacturing in producing Ti-6Al-4V parts. *Int. J. Comput. Integr. Manuf.* **31**, 1–14, 2018
28. Hauser, T., et al.: Oxidation in wire arc additive manufacturing of aluminium alloys. *Addit. Manuf.* **41**, 101958 (2021)
29. Goh, G.D., Sing, S.L., Yeong, W.Y.: A review on machine learning in 3D printing: applications, potential, and challenges. *Artif. Intell. Rev.* **54**(1), 63–94 (2020). <https://doi.org/10.1007/s10462-020-09876-9>
30. Gobert, C., Reutzel, E.W., Petrich, J., Nassar, A.R., Phoha, S.: Application of supervised machine learning for defect detection during metallic powder bed fusion additive manufacturing using high resolution imaging. *Addit. Manuf.* **21**, 517–528 (2018)
31. Khanzadeh, P.R.M., Jafari-Marandi, R., Smith, B.K., Tschopp, M.A., Bian, L.: Quantifying geometric accuracy with unsupervised machine learning: using self-organizing map on fused filament fabrication additive manufacturing parts. *J. Manuf. Sci. Eng.* **140**(3), 031011 (2018)
32. Okaro, I.A., Jayasinghe, S., Sutcliffe, C., Black, K., Paoletti, P., Green, P.L.: Automatic fault detection for laser powder-bed fusion using semi-supervised machine learning. *Addit. Manuf.* **27**, 42–53 (2019)
33. Wasmer, K., Le-Quang, T., Meylan, B., Shevchik, S.A.: In situ quality monitoring in AM using acoustic emission: a reinforcement learning approach. *J. Mater. Eng. Perform.* **28**(2), 666–672 (2018). <https://doi.org/10.1007/s11665-018-3690-2>
34. Tang, S., Wang, G., Song, H., Li, R., Zhang, H.: A novel method of bead modeling and control for wire and arc additive manufacturing. *Rapid Prototyping J.* **27**(2), 311–320 (2021)
35. Barrionuevo, G.O., Ríos, S., Williams, S.W., Ramos-Grez, J.A.: Comparative evaluation of machine learning regressors for the layer geometry prediction in wire arc additive manufacturing. In: *ICMIMT 2021* (2021)
36. Yaseer, A., Chen, H.: Machine learning based layer roughness modeling in robotic additive manufacturing. *J. Manuf. Process.* **70**, 543–552 (2021)
37. Wu, Q., Mukherjee, T., De, A., DeRoy, T.: Residual stresses in wire-arc additive manufacturing – Hierarchy of influential variables. *Addit. Manuf.* **35**, 101355 (2020)
38. Maurya, A., Yeom, J.-T., Kang, S.W., Park, C.H., Hong, J.-K., Reddy, N.: Optimization of hybrid manufacturing process combining forging and wire-arc additive manufactured Ti-6Al-4V through hot deformation characterization. *J. Alloys Compd.* **894**, 162453 (2022)

39. Hu, Z., Qin, X., Li, Y., Ni, M.: Welding parameters prediction for arbitrary layer height in robotic wire arc additive manufacturing. *J. Mech. Sci. Technol.* **34**(4), 1683–1695 (2020). <https://doi.org/10.1007/s12206-020-0331-0>
40. Wang, J., Papadopoulos, P.: Coupled thermomechanical analysis of fused deposition using the finite element method. *Finite Elem. Anal. Des.* **197**, 103607 (2021)
41. Mu, H., Pan, Z., Li, Y., He, F., Polden, J., Xia, C.: MIMO model predictive control of bead geometry in wire arc additive manufacturing. In: 11th IEEE International Conference on Cyber Technology in Automation, Control, and Intelligent Systems (CYBER), Jiaxing (2021)
42. Dharmawan, A.G., Xiong, Y., Foong, S., Soh, G.S.: A model-based reinforcement learning and correction framework for process control of robotic wire arc additive manufacturing. In: ICRA, Paris (2020)
43. Xia, C., Pan, Z., Zhang, S., Li, H., Xu, Y., Chen, S.: Model-free adaptive iterative learning control of melt pool width in wire arc additive manufacturing. *Int. J. Adv. Manuf. Technol.* **110**(7–8), 2131–2142 (2020). <https://doi.org/10.1007/s00170-020-05998-0>
44. Kulkarni, A., Bhatt, P.M., Kanyuck, A., Gupta, S.K.: Using unsupervised learning for regulating deposition speed during robotic wire arc additive manufacturing. In: IDETC-CIE (2021)
45. Wang, Y., et al.: Active disturbance rejection control of layer width in wire arc additive manufacturing based on deep learning. *J. Manuf. Process.* **67**, 364–375 (2021)
46. Lam, T.F., Xiong, Y., Dharmawan, A.G., Foong, S., Soh, G.S.: Adaptive process control implementation of wire arc additive manufacturing for thin-walled components with overhang features. *Int. J. Adv. Manuf. Technol.* **108**(4), 1061–1071 (2019). <https://doi.org/10.1007/s00170-019-04737-4>
47. Xia, C., et al.: Model predictive control of layer width in wire arc additive manufacturing. *J. Manuf. Process.* **58**, 179–186 (2020)
48. Nalajam, P.K., Varadarajan, R.: A hybrid deep learning model for layer-wise melt pool temperature forecasting in wire-arc additive manufacturing process. *IEEE Access* **9**, 100652–100664 (2021)
49. Ding, D., He, F., Yuan, L., Pan, Z., Wang, L., Ros, M.: The first step towards intelligent wire arc additive manufacturing: an automatic bead modelling system using machine learning through industrial information integration. *J. Ind. Inf. Integr.* **23**, 100218 (2021). <https://doi.org/10.1016/j.jii.2021.100218>
50. Farias, F.W.C., Filho, J.D.C.P., Oliveira, V.H.P.M.E.: Prediction of the interpass temperature of a wire arc additive manufactured wall: FEM simulations and artificial neural network. *Addit. Manuf.* **48**(Part A), 102387 (2021)
51. Li, Y., et al.: A defect detection system for wire arc additive manufacturing using incremental learning. *J. Ind. Inf. Integr.* **27**, 100291 (2021)
52. Reisch, R., Hauser, T., Lutz, B., Pantano, M., Kamps, T., Knoll, A.: Distance-based multivariate anomaly detection in wire arc additive manufacturing. In: 2020 19th IEEE International Conference on Machine Learning and Applications (ICMLA), Miami (2020)
53. Wang, Y., Zhang, C., Lu, J., Bai, L., Zhao, Z., Han, J.: Weld reinforcement analysis based on long-term prediction of molten pool image in additive manufacturing. *IEEE Access* **8**, 69908–69918 (2020)
54. Wang, Y., et al.: Coordinated monitoring and control method of deposited layer width and reinforcement in WAAM process. *J. Manuf. Process.* **71**, 306–316 (2021)
55. Nalajam, P.K., Ramesh, V.: Microstructural porosity segmentation using machine learning techniques in wire-based direct energy deposition of AA6061. *Micron* **151**, 103161 (2021)
56. Huang, C., Wang, G., Song, H., Li, R., Zhang, H.: Rapid surface defects detection in wire and arc additive manufacturing based on laser profilometer. *Measurement* **189**, 110503, 2021

57. Surovi, N.A., Dharmawan, A.G., Soh, G.S.: A study on the acoustic signal based frameworks for the real-time identification of geometrically defective wire arc bead. In: 47th Design Automation Conference (2021)
58. Pringle, A., Oberloier, S., Petsiuk, A., Sanders, P., Pearce, J.: Open source arc analyzer: multi-sensor monitoring of wire arc additive manufacturing. *HardwareX* **8**, e00137 (2020)



Research Evolution on Intelligentized K-TIG Welding

Yanxin Cui and Yonghua Shi^(✉)

Guangdong Provincial Engineering Research Center for Special Welding Technology and Equipment, School of Mechanical and Automotive Engineering, South China University of Technology, Guangzhou, China
yhuashi@scut.edu.cn

Abstract. K-TIG welding is a novel and high efficiency deep penetration welding technology, attracting researchers since K-TIG welding was invented in 1997. This paper reviewed the literatures with respect to the K-TIG welding from 1997 to 2021. The importance of the literatures collected from the Web of Science Core Collection were sorted by local citation score(LCS). The intellectualization and improvement progress of the K-TIG welding were introduced, including seam tracking, penetration recognition, investigation on dynamic K-TIG welding process, arc pressure measurement, and enlarging the operating window. Many sensing technologies including arc spectrum analysis and multi-information fusion have great potential in recognizing the penetration status and analyzing the dynamic K-TIG welding process. The exertion of external magnetic field can change the arc shape and improve the mechanical properties of the weld joint. There is still a long way to go to intelligentize and improve the K-TIG welding.

Keywords: K-TIG welding · LCS · Seam tracking · Penetration recognition · Dynamic welding process · Arc pressure · External magnetic field

1 Introduction

Welding is a key technology in modern manufacturing processes, which has an urgent demand of becoming robotic, automotive, and intelligent to substitute for the traditional, time consuming, and low efficiency handworked craft [1]. The mid-thick plates (4.5–25 mm) welding is a difficult and sometimes complex process, which has wide applications in marine ships, pipeline manufacturing, and large-scale pressure vessel. To handle this welding condition, penetrative welding technologies, including plasma arc welding(PAW), laser beam welding(LBW), electric beam welding(EBW), and keyhole tungsten inert gas welding(K-TIG), have been developed. Comparing to other penetrative technologies, K-TIG welding, which is capable of low cost, edge preparation and filler wire avoidable, is an ideal method to join the mid-thick plates.

According to the vivid exposition made by Zhang et al., welding process can be regarded as an optimization problem shown in Eq. (1) [2]. P is the semidefinite positive function, representing the total cost of the given welding problem. κ is the invariant

welding conditions or parameters. ϖ is the variable vector, representing the controllable welding parameters. o is the required welding quality, such as the geometry of weld seam, the microstructure of the weld metal, and the residual stress, etc. $o(\varpi/\kappa)$ describes the relationship between the output or the required welding quality o and the controllable welding parameters ϖ under given conditions κ . The result of the optimization problem is denoted as Eq. (2), where κ^* is the nominal conditions, and ϖ^* is the derived controllable parameters under the nominal conditions κ^* . To solve the mid-thick plates welding problem described by Eq. (1), there are two ways to go. One is to optimize the welding parameters under the given welding technology, i.e., just optimize the κ and ϖ instead of changing the function $o(\varpi/\kappa)$. For example, the mid-thick plates can be joint together by multi-pass welding through traditional welding technology. The other way is to find a suitable and novel welding technology $o(\varpi/\kappa)$ to meet the requirement o . The K-TIG welding is such an appropriate and novel technology for joining mid-thick plates.

$$\begin{cases} \min_{\varpi^{(L)} \leq \varpi \leq \varpi^{(U)}} P(o(\varpi/\kappa)) \\ o^{(L)} \leq o(\varpi/\kappa) \leq o^{(U)} \end{cases} \quad (1)$$

$$\begin{cases} P(o(\varpi^*/\kappa^*)) = \min_{\varpi^{(L)} \leq \varpi \leq \varpi^{(U)}} P(o(\varpi/\kappa^*)) \\ o^{(L)} \leq o(\varpi/\kappa^*) \leq o^{(U)} \end{cases} \quad (2)$$

However, K-TIG welding is a complex physical and chemical process with high coupling of acoustic, optical, thermal, mechanical, magnetic and electrical fields. The operating window is narrow and the penetration ability is sensitive to the height and angle of the tungsten needle, welding current, and welding speed [3]. This fact results in a common phenomenon that in the practical K-TIG welding process, there is a bias $\Delta\kappa$ between the practical welding conditions κ and the nominal conditions κ^* , which lead to the difference between the actually obtained output $o(\varpi^*/\Delta\kappa + \kappa^*)$ and the optimized and required ideal output $o^*(\varpi^*/\kappa^*)$. If the weld torch had a deviation from the weld seam, this deviation $\Delta\kappa$ can be directly measured through vision sensing and can be compensated, which is the weld seam tracking problem. However, there are many parameters cannot be measured or even if they can be measured, they cannot be measured online in real time. For example, the tungsten needle could be burn out and dull under some extreme working conditions, causing the erosion of the penetration ability. Under this condition, the angle of tungsten needle is hard to measure in real-time, and thus the bias $\Delta\kappa$ cannot be compensated. Therefore, as a high efficiency deep penetration welding technology, the main weld defect of K-TIG welding is the penetration defect, which means the penetration o is interfered from the dull tungsten, deformed plates, and changed plates gap, $\Delta\kappa$, resulting in the lack of penetration or burn through. When the $\Delta\kappa$ is hard to measure or even cannot be measured, the controllable welding parameters ϖ should be compensated $\Delta\varpi$, making the output o in Eq. (3) as close as possible to the required ideal output o^* . In actual K-TIG welding practice, the welding parameters in time k can be adjusted as shown in Eq. (4), according to the previous adjusted welding parameters $\Delta\varpi^{(k-1)}$ in time $k-1$. This process can be iterated until the bias $o-o^*$ as small as possible. Some control algorithms like model predictive control(MPC) can handle this process to ensure the whole K-TIG welding

process in the completely penetrated status. The most difficult point during the iteration process is the output o cannot be directly measured. Therefore, we need to find out the relationship between the directly measurable physical information like arc sound, arc electrical signals, and vision information, etc., and the output o . Thus the output o can be indirectly measured. This needs the deeper knowledge and insight into the K-TIG welding process.

$$\min_{\Delta\varpi} P(o(\varpi = \varpi^* + \Delta\varpi/\varpi^*, \kappa^*, \Delta\kappa)) \quad (3)$$

$$\Delta\varpi^{(k)} = \Delta\varpi^{(k-1)} + \gamma(o^{(k)} - o^*) \quad (4)$$

Therefore, this paper aims to introduce the research evolution on intelligentized K-TIG welding, especially on measuring the output o through kinds of sensing technology combining with machine learning technology and the attempts for improving the K-TIG welding. Section 2 introduced the development progress of the K-TIG welding and reviewed the literatures collected from the Web of Science Core Collection. Section 3 reviewed the intellectualization of K-TIG welding, including the seam tracking and penetration recognition. Methods tried to improve the K-TIG welding were presented in Section 4. Finally, conclusions and some research issues were drawn in Section 5.

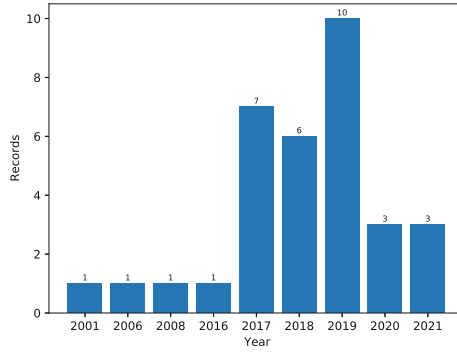
2 The Development Progress of K-TIG Welding

In 1997, based on the traditional TIG welding, a novel high efficiency deep penetration welding technology characterized by the noticeable keyhole, K-TIG welding, was invented by Commonwealth Scientific and Industrial Research Organisation (CSIRO) in Australia. Dr. Jarvis, whose PhD thesis is majoring in the K-TIG welding, lays a solid foundation of the theory and application of the K-TIG welding [4]. Comparing to the traditional TIG welding, the K-TIG welding has three distinct differences:

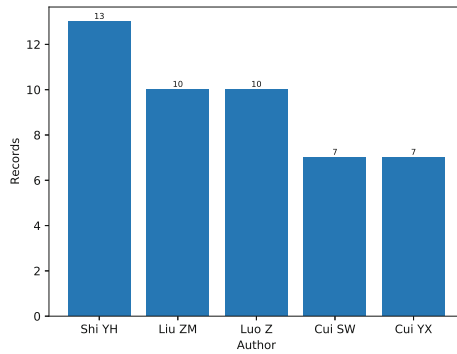
1. When the penetrative process is stable, there is a distinct keyhole on the backside of the weld specimen.
2. The welding current is high. Commonly, the welding current is set at 400–600 A.
3. The tungsten electrode is strongly water-cooled.

The high welding current and strongly water-cooled tungsten needle are responsible for the penetrative process. The higher welding current is, the bigger energy input obtains, thus the more intense self-induced magnetic field in the arc area induces. The free burning arc is radially contracted under the Lorentz force, resulting in the increase of the energy density and arc pressure. The strong water-cooling can reduce the burning loss of the tungsten electrode and extend its service life. Meanwhile, the cathode electron emitting area is compressed, further increasing the current density and enhancing the pinch effect. Therefore, the K-TIG welding is capable of deep penetration welding.

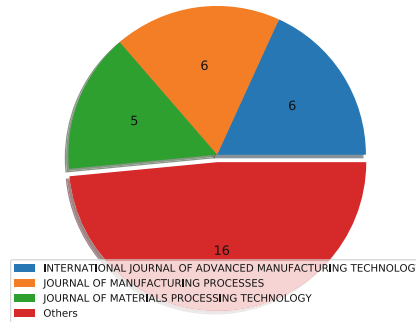
From 1997, there are many works focusing on the K-TIG welding [3–48]. We analyzed 33 literatures in the Web of Science Core Collection [6–24, 26, 27, 29–35, 37, 38, 46–48]. As shown in Fig. 1, K-TIG welding aroused many researchers' interests



(a) The literatures of K-TIG welding sorted by years



(b) The literatures of K-TIG welding sorted by authors



(c) The literatures of K-TIG welding sorted by journals

Fig. 1. The literatures analysis of K-TIG welding

from 2017. The first three authors who contributed the most literatures are Shi YH, Liu ZM, and Luo Z. More than 50% of the literatures were published in INTERNATIONAL JOURNAL OF ADVANCED MANUFACTURING TECHNOLOGY, JOURNAL OF MANUFACTURING PROCESSES, and JOURNAL OF MATERIALS PROCESSING TECHNOLOGY.

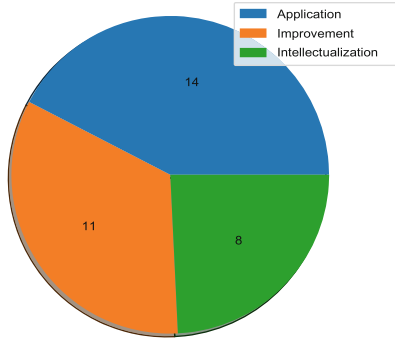


Fig. 2. The literatures of K-TIG welding classified by research directions

Figure 2 shows the research directions of the counted literatures. Fourteen literatures investigated the application of the K-TIG welding on different metal materials, and analyzed the microstructure and mechanical properties of the weld specimen. Eleven literatures analyzed the welding process especially the keyhole dynamic behaviors, and tried kinds of methods to widen the operating window and improve the K-TIG welding. Only eight literatures reported the intellectualization of the K-TIG welding, including the penetration recognition and tracking the weld seam. The historiographs of all the literatures are drawn in Fig. 3. These literatures are sorted by Local Citation Score(LCS), which is the number of citations to the paper from within the collection. The more LCS a paper gets, the more important the paper is, and the bigger circle in Fig. 3 is. Though the most influential paper should be the thesis written by Dr. Jarvis [4], it is not collected in the Web of Science Core Collection. Therefore, the most important literature in Fig. 3 is the one published in 2001, which was also authored by Dr. Jarvis [11]. Recently, literatures [30, 33], and [19] have the most citations, and all of them are reporting the application of the K-TIG welding.

The improvement and intellectualization are more important. One is to improve the $\sigma(\varpi/\kappa)$, providing a novel way to optimize Eq. (1). The other is to obtain the output o and support for optimizing the welding parameters $\Delta\varpi$. Therefore, the following parts are reviewing the related works about improvement and intellectualization of K-TIG welding.

3 The Intellectualization of K-TIG Welding

The intellectualization of K-TIG welding is to make the output o as close as possible to the required output o^* . As a deep penetration welding technology, K-TIG welding

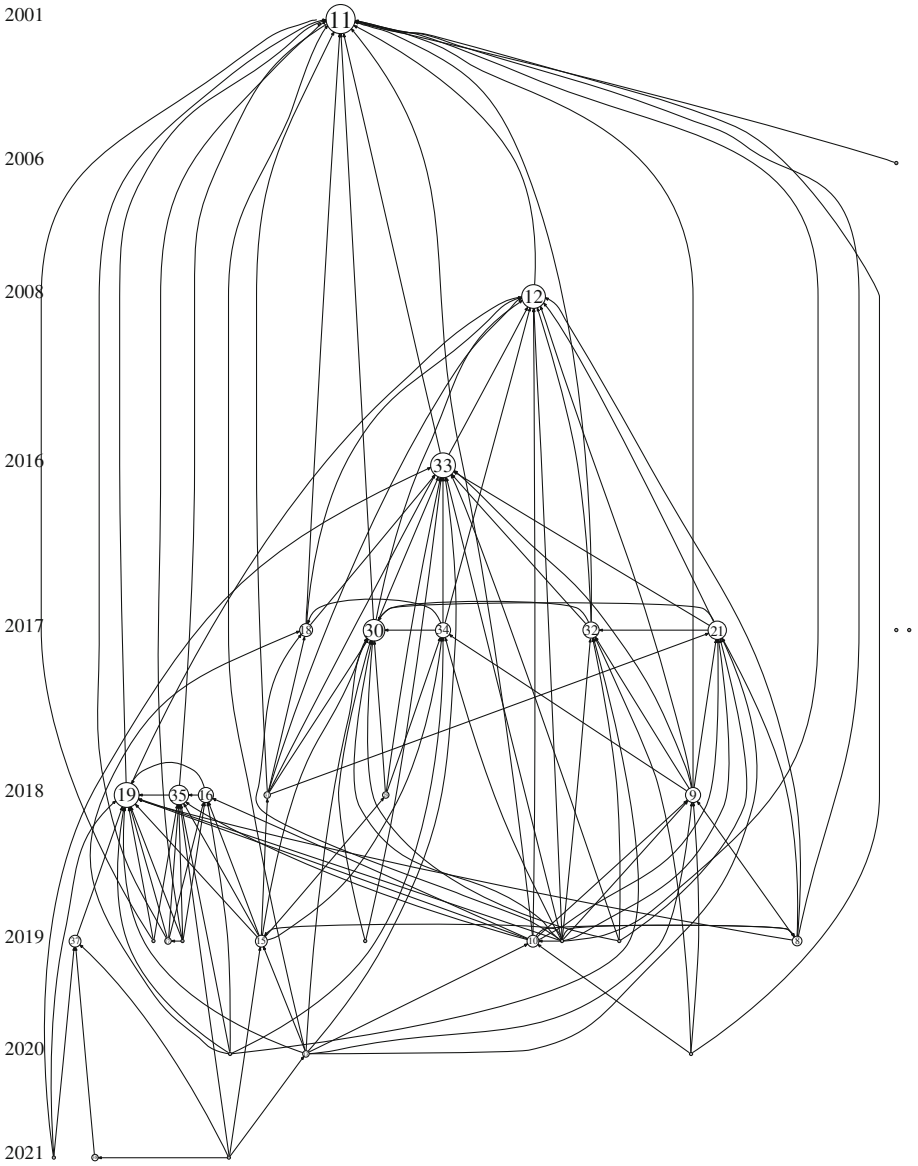


Fig. 3. The historiographs of the K-TIG welding literatures

hardly occurs the slag inclusion, porosity and crack. The main research objects of K-TIG welding are seam tracking and penetration recognition.

3.1 The Research of Seam Tracking in K-TIG Welding

All the works to realize seam tracking utilized the vision sensing technology. However, due to the high welding current, the dynamic range in a captured image containing both

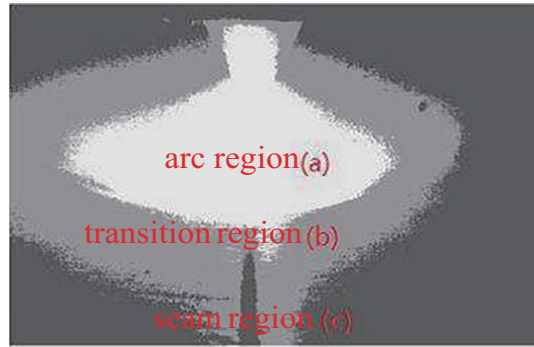


Fig. 4. K-means clustering area division results [39]

the arc area and the seam area is so wide, bringing difficulties to the image processing. To overcome this problem, Gu et al. [26, 37] utilized a high dynamic range (HDR) CMOS camera to capture the vision information. To find the weld seam and weld pool ROIs, Gu et al. proposed a HOG-SVM based algorithm and the error of the proposed weld seam tracking algorithm is only 0.04 mm. Similarly, Liu [41] also utilized the HDR camera. Liu proposed an algorithm in combination with the K-Means, wavelet transform, and random forests to solve the core problem in weld seam tracking, which is the edge detection problem. Considering the real-time performance of the proposed algorithm, Liu performed a parallel optimization of the proposed edge detection algorithm on GPU using CUDA programming. The optimized algorithm ran 123 times faster than that on CPU. The final seam tracking system is able to track the straight-line seam, the polyline seam, and the curve seam, while the error can be controlled within 0.12 mm, 1.65 mm, and 1.76 mm, respectively. The ROI extraction is useful for solving the seam tracking problem. To extract the arc area and seam area ROIs, Zhang et al. [39] proposed the segmentation algorithm based on K-Means clustering. The captured image can be segmented into arc region, transition region, and seam region, as shown in Fig. 4, which reduced difficulties in image processing. Chen et al. [14] proposed the segmentation algorithm based on Mask-RCNN, the flow chart of which is shown in Fig. 5. The proposed algorithm is robust and the input images are directly processed to output the mask of the weld pool region. However, a fixed ROI region is selected to extract the weld seam region. In conclusion, the ROI selection algorithm and the edge detection algorithm are important in the seam tracking in K-TIG welding. The machine learning algorithm, such as Mask-RCNN and SVM, has shown superior performance in the ROI extraction process.

3.2 The Research of Penetration Recognition in K-TIG Welding

As a deep penetration welding technology, maintaining a proper penetration status is significant in the K-TIG welding process. However, due to the inconsistent gap, the deformation of weld specimen, and the sudden interference, etc., the penetration is

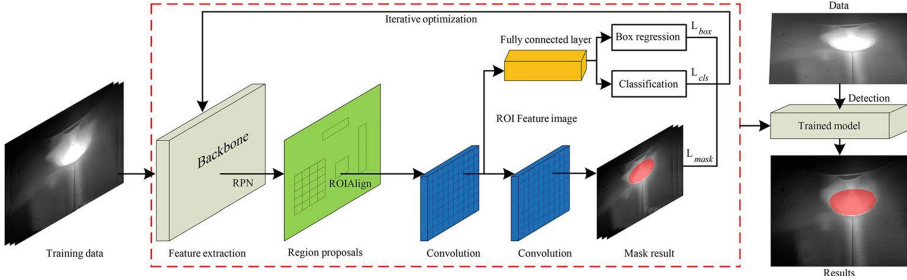


Fig. 5. The weld pool segmentation algorithm based on Mask-RCNN [14]

interfered and transitioned into lack of penetration or burn through. Therefore, the recognition of penetration σ is necessary, which is the basic feedback to control the welding parameters $\Delta\omega$.

Xia et al. [13] utilized the HDR camera to capture the weld pool and arc images during the K-TIG welding process. The undercut, lack of penetration, and burn through are recognized by the proposed ResNet model. However, the thickness of the experimental specimen is only 6 mm, which is too thin in the actual welding practice. Zhu et al. [40] collected the arc sound and analyzed it in the time domain, frequency domain, and the time-frequency domain. The weighted scoring criterion based on the Fisher distance and the maximum information coefficient (Fisher-MIC) were utilized to reduce the dimension of the arc sound features set from 34 to 12. Finally, based on the reduced feature set, a SVM model was trained, which is able to identify the partial penetration, the full penetration, and the excessive penetration within the rate of 92.21%. Considering the high cost of the HDR camera, Zhang et al. [38] proposed the HDR image processing algorithm, empowering the traditional CCD camera to deal with the intense arc light. Image characteristics were extracted from the weld pool region and the keyhole entrance region, based on which the Softmax and SVM model were established. Comparing to the SVM model, Zhang et al. found that the Softmax model has a higher recognition rate and a faster response time.

4 The Research of Improving the K-TIG Welding

The K-TIG welding is characterized by the high welding current, free-burning arc, and backside keyhole. However, due to the high welding current and the free-burning arc, the weld pool region is large and the grains in weld microstructure is coarse, resulting in the narrow operating window and bringing difficulties to the further generalization of the K-TIG welding. Therefore, it is essential to widen the application and generalization of the K-TIG welding, requiring a deeper knowledge of the dynamic K-TIG welding process. Meanwhile, the arc physics needs to be analyzed, especially the arc pressure. Finally, kinds of methods are tried to improve the K-TIG welding.

4.1 The Dynamic K-TIG Welding Process

During the deep penetration welding process, the arc penetrated the whole welding specimen as shown in Fig. 6. Near the side of the welding torch to the back of the

welding specimen, the keyhole can be divided into the keyhole entrance, the keyhole channel and the backside keyhole exit.

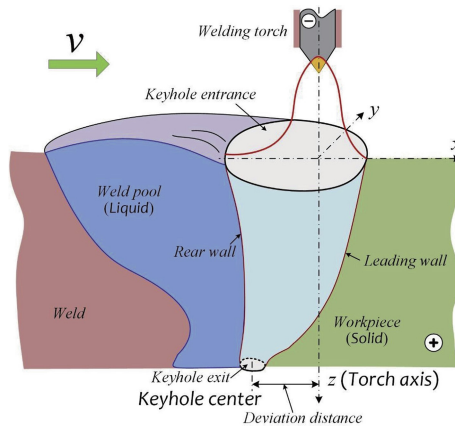


Fig. 6. Sectional view of weld specimen during K-TIG welding process [32]

The backside keyhole exit is often called the keyhole. Comparing to the keyhole entrance covered by the intense arc and the keyhole channel blocked by the weld specimen, it is simple to observe the dynamic behaviors of the backside keyhole exit. Liu et al. [42] established a vision sensing system to observe the dynamic behaviors of the backside keyhole exit in PAW. Based on the vision sensing system, a mature keyhole image processing algorithm was developed, and the dynamic behavior of the backside keyhole was analyzed. Then, Liu et al. [18, 29, 30, 33] upgraded the system to observe the keyhole in the K-TIG welding process.

At present, most of the works aiming to investigate the dynamic K-TIG welding process are observing the backside keyhole. Only a few works observe the keyhole entrance. However, the goal of observing the keyhole entrance is utilizing the keyhole entrance image to track the weld seam [14] or recognize the penetration status [38]. Few literatures reported the research on the keyhole entrance, where most of the arc plasma penetrated through, and where the arc plasma interacted with molten pool dynamically. It is essential to analyze the dynamic behaviors of the keyhole entrance. However, the keyhole entrance is blocked by the weld specimen, bringing difficulties to the observation of the keyhole entrance. Cui et al. [43, 44] referenced to the observation of keyhole entrance in LBW, and established a steel/glass sandwich based sensing system to observe the dynamic behaviors of the keyhole entrance and the sectional weld pool, as shown in Fig. 7. The dynamic behaviors of the arc, keyhole, and weld pool are observed during the whole K-TIG welding process, including the arc ignition stage, the stable arc stage, and the arc extinction stage, as shown in Fig. 8. Cui et al. [43] investigated the influence of axial magnetic field on K-TIG welding by means of the established sandwich based sensing system. Cui et al. found that the arc emitting area decreased with the exertion of axial magnetic field, resulting in the increase of arc force and arc pressure, which finally lead to the improvement of the penetration ability.

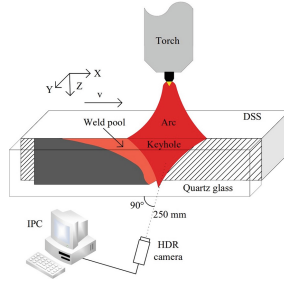


Fig. 7. Schematic of the sandwich based vision sensing system [44]

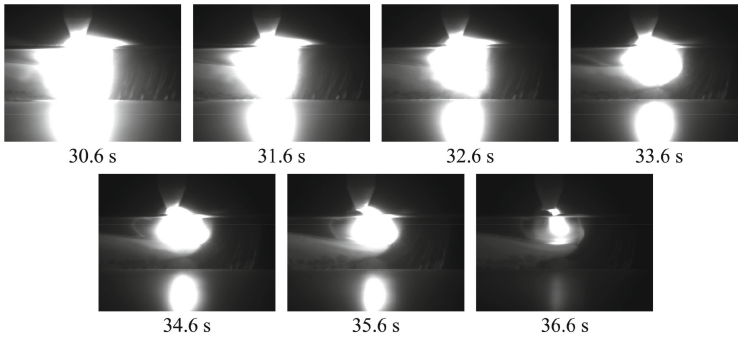


Fig. 8. Arc extinction process in K-TIG welding [44]

4.2 The Arc Pressure in K-TIG Welding Process

In 2001, Jarvis [4] has investigated the physical properties of the K-TIG arc, and found the important role of surface tension in maintaining keyhole channel. The role of arc pressure in penetrating the weld specimen was also analyzed. However, the arc pressure was measured in relative weight limited to the experiment methods. Further accurate measurement in Pa is still required.

Recently, Cui et al. [3] established an arc pressure measurement device, as shown in Fig. 9. Experiments were carried out under the 3 mm arc length and 20 L/min pure Argon protective gas. The maximum arc pressure was 757 Pa under the 250 A welding current. However, the operating window of welding current is 515–622 A when carrying out the bead on plate welding experiments on 8 mm thickness 304 stainless steel. The experimental welding current 250 A is too small to represent the actual welding practice. What's more, the pinhole of the measurement device is $\phi 2$, which is large compared to the diameter of the tungsten needle. Therefore, Liu et al. [28] improved the measurement device, and the pinhole was reduced to $\phi 1.5$. The arc pressure under the influence of cusp magnetic field was measured, and the maximum arc pressure was 818 Pa. Though the maximum arc pressure increased when the cusp magnetic field was exerted, it is hard to assert that the arc pressure was enhanced by the cusp magnetic field considering the precision class of the pressure sensor.

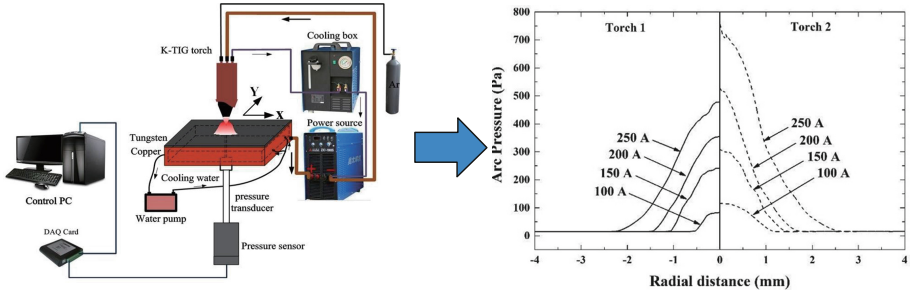


Fig. 9. The arc pressure measurement device and the measured arc pressure [3]

Considering the limitations of the current arc pressure measurement methods in K-TIG welding, the authors designed a water-cooling enhancing arc pressure measurement device, as shown in Fig. 10. The pinhole is controlled within 0.5–1 mm as the top surface should be turning into plain after several welding experiments. Experiments were carried out to measure the spatial distribution of the arc pressure, and the welding parameters were shown in Table 1. The spatial distribution of the arc pressure is shown in Fig. 11. The maximum arc pressure is 5362 Pa. Projecting the arc pressure onto X-Y plane, the distribution of the arc pressure on the top surface of the weld specimen can be obtained, as shown in Fig. 12. The arc pressure is in an axial symmetrical distribution along X axis, which is the direction of the weld speed. However, the arc pressure measurement device should be further optimized to measure the arc pressure under a higher welding current.

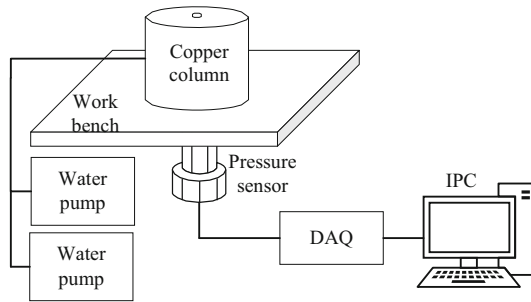


Fig. 10. Schematic of the arc pressure measurement system in K-TIG welding

Table 1. The welding parameters of the arc pressure measurement experiments

Welding current(A)	Welding speed(mm s ⁻¹)	Arc length(mm)	Ar flow rate(L/min)
350	4	3	20

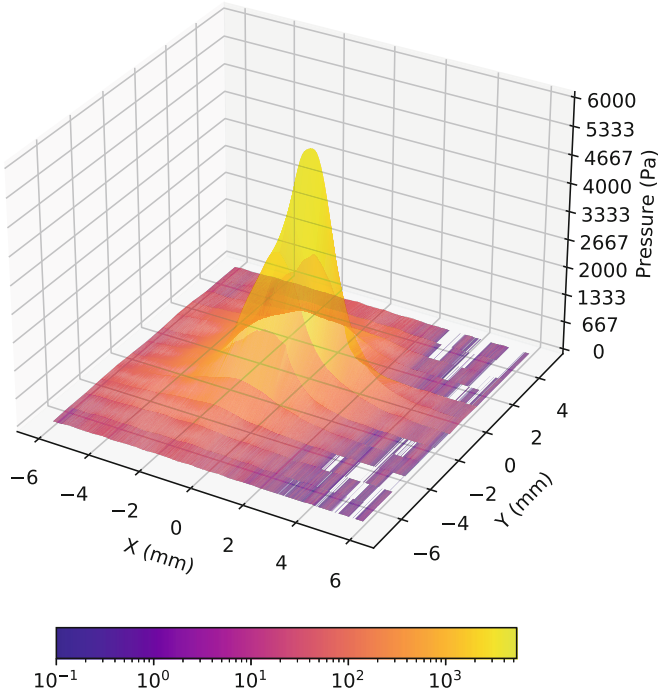


Fig. 11. The spatial distribution of the arc pressure

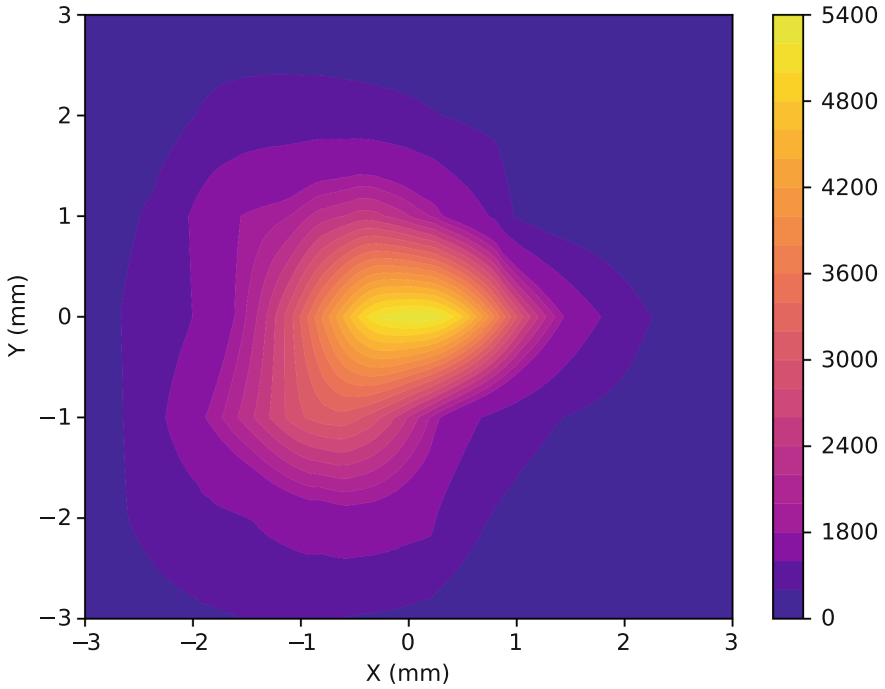


Fig. 12. The distribution of the arc pressure on the top surface of the weld specimen

4.3 Methods Tried to Improve the K-TIG Welding

After analyzing the dynamic keyhole process and the arc pressure, there are many directions to improve the K-TIG welding, including improving the penetration ability, reducing the threshold penetration welding current, and optimizing the microstructure and properties of the weld. Many works have been done to achieve these goals, including optimizing the structure of the weld torch, constricting the arc by external magnetic field, and adding filling wires.

Cui et al. [3, 27] designed a weld torch with strong cooling capacity. The high temperature region in the tip of tungsten torch is successfully compressed. In combination with the optimization of the angle and materials of the tungsten needle, the arc pressure is finally increased. Finally, the threshold welding current is decreased and the operating window is enlarged. Liu et al. [32] exerted the jet flow argon gas backing on 16Mn steel, widening the operating window from 410–450 A in normal protective gas conditions to 420–540 A. The specially designed device is shown in Fig. 13.

To obtain a better performance of the microstructure of the armour steel joint, Fei et al. [5] used a trapezoidal interlayer to weld the 6.2 mm armour steel, as shown in Fig. 14. Good mechanical properties were obtained by utilizing this interlayer welding method. To simplify the welding procedure of preparing the trapezoidal interlayer, Fei et al. [8] utilized the ER308 as the filler wires, substituting the interlayer to weld the armour steel. For dissimilar joint between ferritic steel and austenitic stainless steel, Fei et al. [7] utilized the post-weld heat treatment to improve the microstructure and mechanical properties of the dissimilar joint. Fei et al. found that the 760 °C of the post-weld heat treatment can obtain a better performance with respect to the overall mechanical properties.

The exertion of the external magnetic field can affect the arc and the weld pool. Liu et al. [28, 31] investigated the influence of the cusp magnetic field on K-TIG welding. As shown in Fig. 15, the arc shape varies with the variation of the cusp magnetic field angle α . When the cusp magnetic field was exerted, the arc voltage increased and the threshold welding current decreased. The smaller the angle α is, the smaller the melting region is, and the larger the arc voltage and penetration depth are. Ning et al. [45] investigate the influence of rotation magnetic field, axial magnetic field, and rotation-axial composite magnetic field on K-TIG welding. Ning et al. reported that the arc radius increased with the increase of the rotation frequency when the rotation magnetic field was exerted. With regard to the weld pool, the weld pool bears the axial force when the rotation magnetic field is exerted while it bears radial force when the axial magnetic field is exerted. Therefore, the axial magnetic field can stir the molten pool and the low temperature impact energy of the 10 mm Q345R weld joint can reach 53.6 J.

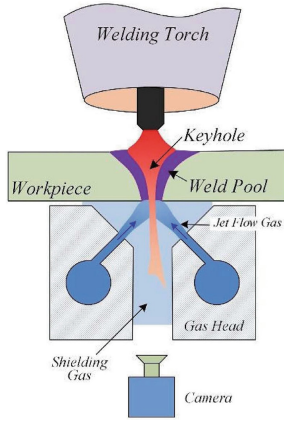


Fig. 13. The installation of jet flow argon gas backing [32]

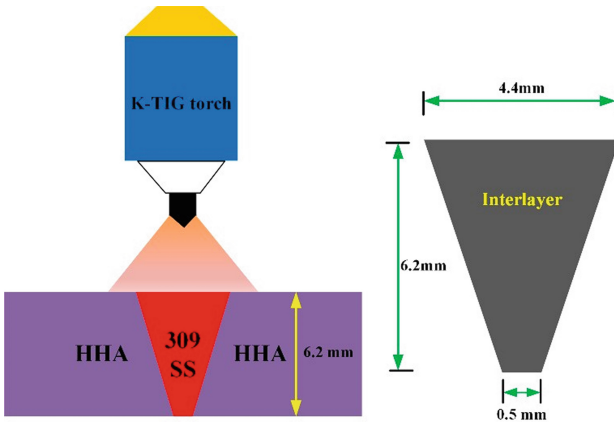


Fig. 14. Schematic of the K-TIG welding process in combination with the interlayer [5]

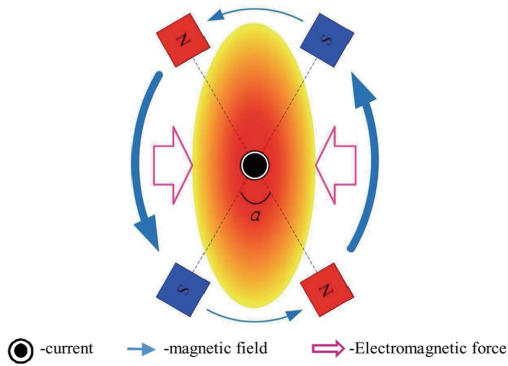


Fig. 15. The influence of cusp magnetic field on arc [28]

5 Conclusions

This paper reviewed the literatures of the K-TIG welding, conclusions and research issues are drawn as follows.

- 1) Literatures with higher LCS are reporting the application of the K-TIG welding, indicating that these kinds of works could arouse the readers' interests. However, more works should be done to intelligentize and improve the K-TIG welding.
- 2) Considering the intense arc light in the K-TIG welding, all the seam tracking works utilized the HDR technology, no matter from the hardware or software. Machine learning technology shows great potential in welding image processing.
- 3) The penetration status in K-TIG welding can be recognized by processing the arc sound signals and welding images. The recognition rate should be improved. The potential of arc spectrum, arc electrical information, and multi-information fusion could be investigated in recognizing the penetration status.
- 4) The importance of arc emitting region in the tungsten needle is revealed by analyzing the dynamic K-TIG welding process. Enhancing the water-cooling in the weld torch can compress the arc emitting region, thus the arc pressure is increased and the operating window is enlarged.
- 5) The arc pressure of K-TIG welding is higher than 5 kPa in the normal conditions. The arc pressure measurement device could be optimized and more accurate values should be obtained especially under the welding current of 400–600 A.
- 6) Many kinds of methods are tried to improve the K-TIG welding. The exertion of the external magnetic field shows great potential. To date, only the influence of rotation magnetic field, axial magnetic field, and cusp magnetic field have been investigated. The influence of transverse magnetic field and longitudinal magnetic field on K-TIG welding should be studied.

Acknowledgments. The authors gratefully acknowledge the financial support for this work from the Key Research and Development Program of Guangdong Province (Grant No. 2020B090928003), National Natural Science Foundation of Guangdong Province (Grant No. 2020A1515011050), and Guangdong Province Marine Economic Development Project (Grant No. GDOE[2019]A13).

References

1. Chen, S.B., Lv, N.: Research evolution on intelligentized technologies for arc welding process. *J. Manuf. Process.* **16**(1), 109–122 (2014)
2. Zhang, Y.M., Yang, Y.-P., Zhang, W., Na, S.-J.: Advanced welding manufacturing: a brief analysis and review of challenges and solutions. *J. Manuf. Sci. Eng.* **142**(11), 110816 (2020)
3. Cui, S.: Study on cathode focusing behavior in water-cooled TIG tungsten electrode, Master, Tianjin University, Tianjin (2018)
4. Jarvis, B.L.: Keyhole gas tungsten arc welding: A new process variant, PhD Thesis, University of Wollongong (2001)

5. Fei, Z., Pan, Z., Cuiuri, D., Li, H., Gazder, A.A.: A combination of keyhole GTAW with a trapezoidal interlayer: a new insight into armour steel welding. *Materials* **12**(21), 3571 (2019)
6. Fei, Z., et al.: Effect of heat input on weld formation and tensile properties in keyhole mode TIG welding process. *Metals* **9**(12), 1327 (2019)
7. Fei, Z., Pan, Z., Cuiuri, D., Li, H., Huang, W., Peng, Z.: Effect of post-weld heat treatment on microstructure and mechanical properties of deep penetration autogenous TIG-welded dissimilar joint between creep strength enhanced ferritic steel and austenitic stainless steel. *Int. J. Adv. Manuf. Technol.* **108**(9–10), 3207–3229 (2020)
8. Fei, Z., Pan, Z., Cuiuri, D., Li, H., Wu, B., Su, L.: Improving the weld microstructure and material properties of K-TIG welded armour steel joint using filler material. *Int. J. Adv. Manuf. Technol.* **100**(5–8), 1931–1944 (2018). <https://doi.org/10.1007/s00170-018-2787-y>
9. Fei, Z., et al.: Investigation into the viability of K-TIG for joining armour grade quenched and tempered steel. *J. Manuf. Process.* **32**, 482–493 (2018)
10. Fei, Z., Pan, Z., Cuiuri, D., Li, H., Van Duin, S., Yu, Z.: Microstructural characterization and mechanical properties of K-TIG welded SAF2205/AISI316L dissimilar joint. *J. Manuf. Process.* **45**, 340–355 (2019)
11. Lathabai, S., Jarvis, B., Barton, K.: Comparison of keyhole and conventional gas tungsten arc welds in commercially pure titanium. *Mater. Sci. Eng., A* **299**(1–2), 81–93 (2001)
12. Lathabai, S., Jarvis, B.L., Barton, K.J.: Keyhole gas tungsten arc welding of commercially pure zirconium. *Sci. Technol. Weld. Joining* **13**(6), 573–581 (2008)
13. Xia, C., Pan, Z., Fei, Z., Zhang, S., Li, H.: Vision based defects detection for Keyhole TIG welding using deep learning with visual explanation. *J. Manuf. Process.* **56**, 845–855 (2020)
14. Chen, Y., Shi, Y., Cui, Y., Chen, X.: Narrow gap deviation detection in keyhole TIG welding using image processing method based on Mask-RCNN model. *Int. J. Adv. Manuf. Technol.* **112**(7–8), 2015–2025 (2021). <https://doi.org/10.1007/s00170-020-06466-5>
15. Cui, Y., Shi, Y., Hong, X.: Analysis of the frequency features of arc voltage and its application to the recognition of welding penetration in K-TIG welding. *J. Manuf. Process.* **46**, 225–233 (2019)
16. Cui, S., Shi, Y., Cui, Y., Zhu, T.: The impact toughness of novel keyhole TIG welded duplex stainless steel joints. *Eng. Fail. Anal.* **94**, 226–231 (2018)
17. Cui, S., Shi, Y., Cui, Y., Zhu, T.: The influence of microstructure and chromium nitride precipitations on the mechanical and intergranular corrosion properties of K-TIG weld metals. *Constr. Build. Mater.* **210**, 71–77 (2019)
18. Cui, S., Liu, Z., Fang, Y., Luo, Z., Manladan, S.M., Yi, S.: Keyhole process in K-TIG welding on 4 mm thick 304 stainless. *J. Mater. Process. Technol.* **243**, 217–228 (2017)
19. Cui, S., Shi, Y., Sun, K., Gu, S.: Microstructure evolution and mechanical properties of keyhole deep penetration TIG welds of S32101 duplex stainless steel. *Mater. Sci. Eng., A* **709**, 214–222 (2018)
20. Cui, S., Xian, Z., Shi, Y., Liao, B., Zhu, T.: Microstructure and Impact toughness of local-dry keyhole tungsten inert gas welded joints. *Materials* **12**(10), 1638 (2019)
21. Fang, Y., Liu, Z., Cui, S., Zhang, Y., Qiu, J., Luo, Z.: Improving Q345 weld microstructure and mechanical properties with high frequency current arc in keyhole mode TIG welding. *J. Mater. Process. Technol.* **250**, 280–288 (2017)
22. Liu, Z., Chen, S., Cui, S., Lv, Z., Zhang, T., Luo, Z.: Experimental investigation of focusing cathode region by cooling tungsten. *Int. J. Therm. Sci.* **138**, 24–34 (2019)
23. Cui, S., Shi, Y., Zhu, T., Liu, W.: Microstructure, texture, and mechanical properties of Ti-6Al-4V joints by K-TIG welding. *J. Manuf. Process.* **37**, 418–424 (2019)
24. Cui, Y., Shi, Y., Zhu, T., Cui, S.: Welding penetration recognition based on arc sound and electrical signals in K-TIG welding. *Measurement* **163**, 107966 (2020)
25. Feng, Y., Luo, Z., Liu, Z., Li, Y., Luo, Y., Huang, Y.: Keyhole gas tungsten arc welding of AISI 316L stainless steel. *Mater. Des.* **85**, 24–31 (2015)

26. Gu, S., Shi, Y.: Image processing and weld deviation recognition of robotic deep penetration TIG welding. In: The 7th Annual IEEE International Conference on Cyber Technology in Automation, Control and Intelligent Systems, IEEE, Hawaii (2017)
27. Liu, Z., Fang, Y., Chen, S., Zhang, T., Lv, Z., Luo, Z.: Focusing cathode tip characteristics in cooling tungsten. *Energy* **167**, 982–993 (2019)
28. Liu, S., Liu, Z.M., Zhao, X.C., Fan, X.G.: Influence of cusp magnetic field configuration on K-TIG welding arc penetration behavior. *J. Manuf. Process.* **53**, 229–237 (2020)
29. Liu, Z., Chen, S., Liu, S., Luo, Z., Yuan, J.: Keyhole dynamic thermal behaviour in K-TIG welding process. *Int. J. Heat Mass Transf.* **123**, 54–66 (2018)
30. Liu, Z., et al.: Keyhole thermal behavior in GTAW welding process. *Int. J. Therm. Sci.* **114**, 352–362 (2017)
31. Liu, Z., Chen, S., Yuan, X., Zuo, A., Zhang, T., Luo, Z.: Magnetic-enhanced keyhole TIG welding process. *Int. J. Adv. Manuf. Technol.* **99**(1–4), 275–285 (2018). <https://doi.org/10.1007/s00170-018-2501-0>
32. Liu, Z., Fang, Y., Qiu, J., Feng, M., Luo, Z., Yuan, J.: Stabilization of weld pool through jet flow argon gas backing in C-Mn steel keyhole TIG welding. *J. Mater. Process. Technol.* **250**, 132–143 (2017)
33. Liu, Z., et al.: Stable keyhole welding process with K-TIG. *J. Mater. Process. Technol.* **238**, 65–72 (2016)
34. Liu, Z., et al.: Sustaining the open keyhole in slow-falling current edge during K-TIG process: principle and parameters. *Int. J. Heat Mass Transf.* **112**, 255–266 (2017)
35. Shi, Y., Cui, S., Zhu, T., Gu, S., Shen, X.: Microstructure and intergranular corrosion behavior of HAZ in DP-TIG welded DSS joints. *J. Mater. Process. Technol.* **256**, 254–261 (2018)
36. Shi, Y., Cui, Y., Cui, S., Zhang, B.: A Novel high-efficiency keyhole tungsten inert gas (k-tig) welding: principles and practices. In: Paulo Davim, J. (ed.) *Welding Technology*, pp. 313–367. Springer, Cham (2021). https://doi.org/10.1007/978-3-030-63986-0_10
37. Zhang, B., Shi, Y., Gu, S.: Narrow-seam identification and deviation detection in keyhole deep-penetration TIG welding. *Int. J. Adv. Manuf. Technol.* **101**(5–8), 2051–2064 (2019)
38. Zhang, B., Shi, Y., Cui, Y., Wang, Z., Hong, X.: Prediction of keyhole TIG weld penetration based on high-dynamic range imaging. *J. Manuf. Process.* **63**, 179–190 (2021). <https://doi.org/10.1016/j.jmapro.2020.03.053>
39. Zhang, B., Shi, Y.: Welding deviation extraction during K-TIG welding based on k-means clustering. In: Chen, S., Zhang, Y., Feng, Z. (eds.), *Transactions on Intelligent Welding Manufacturing*, Springer, Singapore, pp. 93–107 (2020). https://doi.org/10.1007/978-981-15-7215-9_6
40. Zhu, T., Shi, Y., Cui, S., Cui, Y.: Recognition of weld penetration during K-TIG welding based on acoustic and visual sensing. *Sens. Imaging* **20**(1), 1–21 (2019). <https://doi.org/10.1007/s11220-018-0224-9>
41. Liu, W.: Research on Narrow Gap Seam Tracking System of K-TIG Welding, Master, South China University of Technology, Guangzhou(2019)
42. Liu, Z.M., Wu, C.S., Chen, M.A.: Visualizing the influence of the process parameters on the keyhole dimensions in plasma arc welding. *Meas. Sci. Technol.* **23**(10), 105603 (2012)
43. Cui, Y., Kang, Y., Shi, Y., Chen, J., Wang, Z., Wang, J.: Investigation into the arc profiles and penetration ability of axial magnetic field-enhanced K-TIG welding by means of a specially designed sandwich. *J. Manuf. Process.* **68**, 32–41 (2021)
44. Cui, Y.-X., Shi, Y.-H., Ning, Q., Chen, Y.-K., Zhang, B.-R.: Investigation into keyhole-weld pool dynamic behaviors based on HDR vision sensing of real-time K-TIG welding process through a steel/glass sandwich. *Adv. Manuf.* **9**(1), 136–144 (2021)
45. Ning, Q.: Research on K-TIG Welding Magnetic Control Technology and Welding Process of q345r Steel, Master, South China University of Technology, Guangzhou (2020)

46. Lathabai, S., Barton, K.J., Green, L.K., Tyagi, V.K.: Microstructure and mechanical properties of keyhole gas tungsten arc welds in titanium and titanium alloys, trends in welding research. In: Proceedings, pp. 711–716 (2006)
47. Sales, A.M., Westin, E.M., Jarvis, B.L.: Effect of nitrogen in shielding gas of keyhole GTAW on properties of duplex and superduplex welds. *Welding in World* **61**(6), 1133–1140 (2017)
48. Zhang, B., Shi, Y., Cui, Y., Wang, Z., Chen, X.: A high-dynamic-range visual sensing method for feature extraction of welding pool based on adaptive image fusion. *Int. J. Adv. Manuf. Technol.* **117**(5–6), 1675–1687 (2021)

Research Papers



Segmentation-Based Automatic Recognition for Weld Defect in Radiographic Testing Image

Ming Zhu^(✉), Xiaohua Chen, Hulong Zhang, Yu Shi, and Ding Fan

State Key Laboratory of Advanced Processing and Recycling of Non-Ferrous Metals,
Lanzhou University of Technology, Lanzhou 730050, China
zhumings@yeah.net

Abstract. In order to improve the efficiency of radiographic evaluation, the method of image processing was used to extract weld defects. According to the characteristics of weld radiographic image, a defect recognition algorithm based on image segmentation was proposed. The algorithm was divided into three stages: image preprocessing, weld segmentation and defect segmentation. Firstly, the influence of different image enhancement algorithms and filtering methods on the preprocessing effect of weld X-ray image was analyzed. Then an automatic segmentation method based on connected region size was proposed. Finally, the local threshold binarization and flooding filling algorithm were used to extract the potential defects, and the aspect ratio, circularity and effective area were calculated. The results show that the extracted parameters can reflect the shape features of actual defects.

Keywords: Extraction of defect · Radiographic testing · X-ray image

1 Introduction

Welded structures are widely used in many areas, such as construction, aerospace, railway, petrochemical and machinery electrical. The weld defects are inevitable because of the different environmental conditions and welding technology in the welding process. It is critical to check the quality of welded joints to assure the reliability and safety of the structure, especially for those critical applications where weld failure can be catastrophic. Being a part of NDT, the radiographic testing (RT) has played a significant role in the inspection of welds. This technique uses penetrating and ionizing radiations such as X-rays or gamma rays to detect, in a welded joint, internal discontinuities. The obtained radiograms are then manually examined by radiography expert proceeds to their quantification and their identification to decide about their acceptance or rejection according to the requirements of the weld RT standards and codes [1]. Finally, due to the high developed film density, a subsequent illumination through a negatoscope is applied to permit the film examination and interpretation. However, the human visualization quality of the films remains low due to many factors, such as bad contrast, image noise, low dimension of some defects, interpreter skills and experience, interpreter physical and mental states at the moment of interpretation, etc., making the evaluation subjectivity

not negligible during weld defect detection and identification process [2]. Therefore, RT-based computer vision weld interpretation system using image processing and pattern recognition are, more than never, recommended.

Since the radiographic image has the characteristics of low contrast, narrow intensity range, and multi-source noise, the preprocessing steps mainly include contrast enhancement and noise filtering [3, 4]. Many scholars rush into the improvement of filter to avoid the loss of detail information in the preprocessing process. A local pixel nonuniformity factor (LPIF) method was proposed to enhance the contrast of radiographic images [5], which can not only improve the contrast but eliminate noise. The track continuity of defects in image sequences was detected by Kalman filter to identify real defects [6]. Some researchers are also committed to the development of filters, such as anisotropic diffusion filtering [7] and Gabor filter [8]. The radiographic film contains the weld area and other areas, while the defects are often located in the weld. Therefore, it is necessary to extract weld area before defect extraction to avoid the interference of other areas on defect detection. Threshold segmentation [9], morphological operation [10], background difference method [11], region growth [12] and edge detection [13] have been widely used in defect extraction. However, there is no algorithm can be enough to the defect extraction of all radiographic films because the weld radiographic films obtained under different conditions have different sizes, shapes, contrasts and textures. Therefore, different algorithms according to different welding conditions have been designed. In ref [14], double wall double image (DWDI) exposure technology was studied for automatic radiographic inspection of pipeline interior. Chi [15] studied the radiographic image processing algorithm of steel plate lap weld. The support vector machine of [16] was used to extract the image. Although these algorithms have achieved good detection results, their generality is still limited.

In this paper, weld defects can be automatically recognized from radiographs through image preprocessing, weld segmentation and defect segmentation. During the image preprocessing, adaptive histogram equalization (AHE) can balance the brightness of the weld area and improve the contrast between the defect area and the background without noise being enhanced obviously after compared with ordinary histogram equalization. Then the mean filtering with 9×3 size of template can effectively remove the noise points of radiograph without destroying useful information. In the step of weld segmentation, an algorithm based on the size of locally connected regions was proposed, and it is capable of extracting weld bead from different radiographs. In the step of defect segmentation, combining local thresholding and flood filling can adaptively extract defects.

2 Experiments and Analysis

In this paper, radiographic images of circumferential weld of a pressure vessel in a factory were studied. Aiming at the characteristics of low contrast, narrow intensity range and multi-source noise of weld radiographic images, the following automatic defect recognition algorithm was designed in this paper (Fig. 1). The algorithm is based on OpenCV, Python 3.7 and PyCharm compiler.

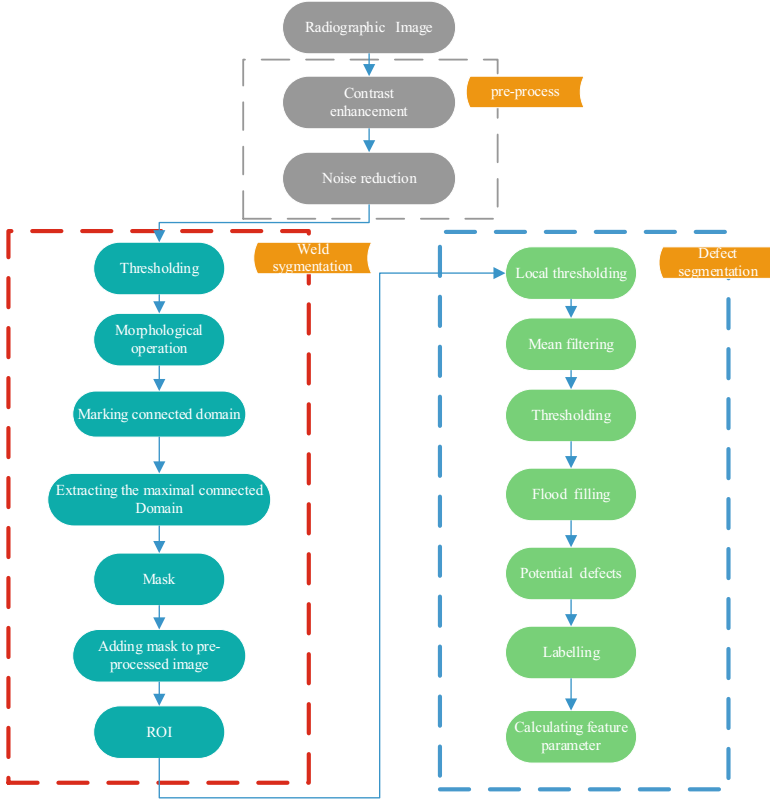


Fig. 1. Procedure of the proposed algorithm for automatic defect recognition

2.1 Image Preprocessing

Contrast Enhancement. The weld seam and defect do not form a strong contrast with the background because of the low contrast of X-ray image, which makes the image segmentation very difficult. Therefore, it is necessary to highlight the useful information of the image through histogram equalization. The conventional histogram equalization can be expressed as follows:

$$g(x, y) = T[f(x, y)] \quad (1)$$

where $f(x, y)$ is the original gray value of point (x, y) , $g(x, y)$ is the enhanced gray value of point (x, y) , and T is the gray transformation function of f . After histogram equalization, the dynamic range of gray image is enlarged. However, histogram equalization belongs to point processing enhancement and is a global processing algorithm, which will lead to the loss of useful information of the image. The adaptive histogram equalization algorithm changes the contrast of the image by calculating the local histogram of the image and redistributing the brightness. This algorithm is more suitable for enhancing the local contrast of the weld radiographic image and obtaining more image details. The

calculation formula is shown in (2):

$$x'_{i,j} = \begin{cases} T(x_{i,j}) + k(x_{i,j} - m_{i,j}) & 0 \leq x_{i,j} \leq 255 \\ T(x_{i,j}) & otherwise \end{cases} \quad (2)$$

where $x_{i,j}$. and $x'_{i,j}$ represent the gray value of the image before and after the transformation, $m_{i,j}$ denoted by $x_{i,j}$ is the neighborhood mean of the center, T is for $x_{i,j}$ can adjust the dynamic range of histogram, $k(x_{i,j} - m_{i,j})$ is equivalent to a high pass filter, which can enhance the local contrast.

The gray scale image of the pressure pipeline weld X-ray film image shows in Fig. 1a, and the effect of the weld line image through the ordinary histogram equalization shows in Fig. 1b. It can be seen that the contrast between the weld area and the defect area is improved, and the surrounding noise is amplified, and the defect is covered by noise. Figure 1c shows the effect of the adaptive histogram equalization algorithm, which well balances the brightness of the weld area, improves the contrast between the defect area and the background, and the noise is not obviously enhanced. Therefore, in order to avoid the influence of noise equalization on the histogram, the image enhancement was realized by using the histogram. The results of adaptive histogram equalization of the remaining two radiographs are shown in Fig. 3.

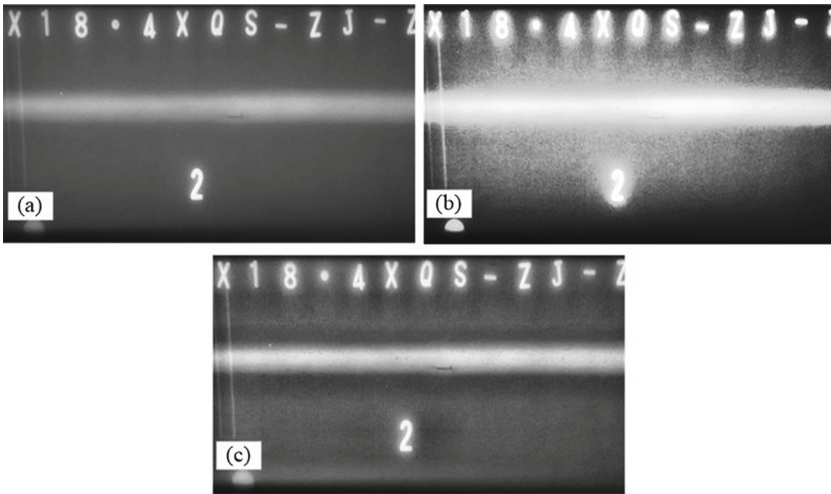


Fig. 2. (a). original gray image; (b). histogram equalized image; (c). adaptive histogram equalized image

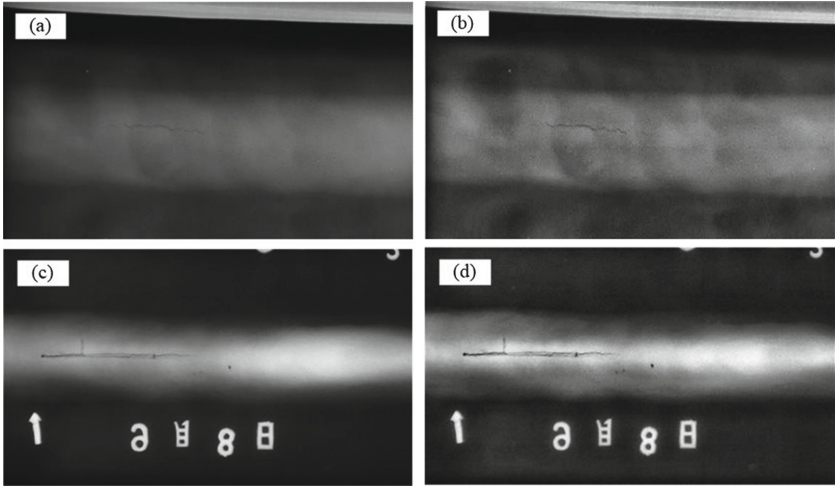


Fig. 3. (a). original gray image; (b). histogram equalized image; (c). adaptive histogram equalized image

Mean Filtering. It is necessary to filter and suppress the radiographic noise which have been enhanced by previous step. The purpose can be achieved with convolution operation of filtering template. The formula mean filtering can be described as follows:

$$f(x, y) = \frac{1}{M} \sum_{(i,j) \in R} g(i, j) \quad (3)$$

where R represents an area in the image, M represents the total number of pixels in the R area, and points (x, y) are the center pixels of the R area.

Figure 4 shows the results of mean filtering on Fig. 2c with 3×3 , 5×5 and 9×3 templates. It can be seen that the 3×3 template (Fig. 4a) has a bad noise suppression effect, but the edge of the weld area becomes heavily fuzzy under the 5×5 template (Fig. 4b), and loses a lot of defect details. However, the 9×3 template (Fig. 4c) has a superior mean filtering effect, that is, it can filter useless information and retain the defect details and weld edges completely. Therefore, 9×3 template mean filter was used to denoise the image in this paper, and the average filtering result is shown in Fig. 5.

2.2 Weld Area Extraction Based on Connected Region Size

Weld area extraction equates essentially a problem of image segmentation. But image segmentation methods are often highly specific and only suitable for some types of problems and images. There is no a special method can solve all the image segmentation problems. Because the X-ray image contains not only the weld seam, but also the film model, date and other areas, mask method, commonly used in OpenCV image processing, was used to extract the weld area. The basic idea is: firstly, the mask of the region of interest is obtained, and then the obtained mask and the original image are matrix added. The key step to realize mask extraction is to obtain mask. The conventional method of obtaining mask by drawing is obviously limited by the size of the image.

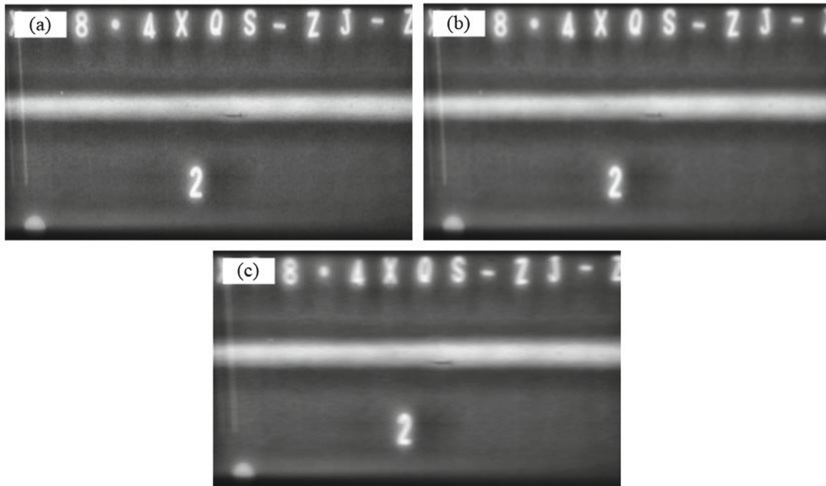


Fig. 4. The results of mean filtering with different template size: (a). 3×3 size; (a). 5×5 size; (a). 9×3 size

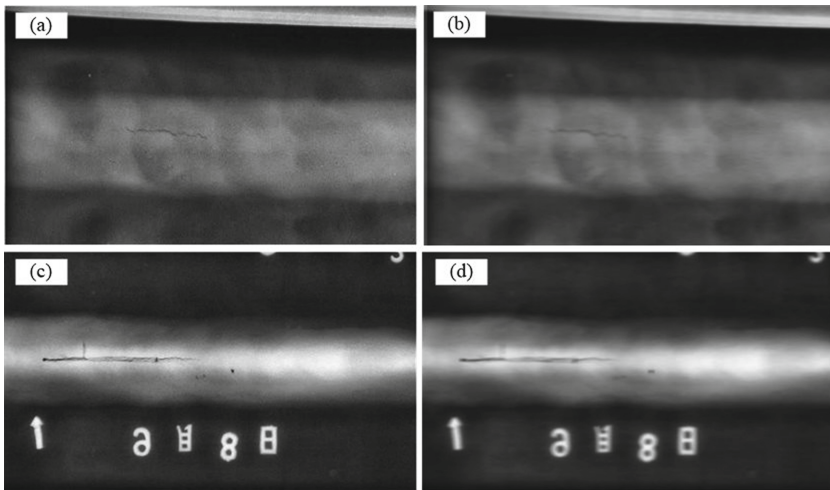


Fig. 5. Results of mean filtering: (a) (c). contrast enhanced images; (b) (d). mean filtered images

Therefore, combined with the characteristics of the X-ray image, that is, there are various connected regions, and the weld area is the largest, so this paper proposed to use the maximum through domain method to obtain the mask of weld area. The design algorithm is as follows: (1) After preprocessing the image, binarization, expansion and corrosion operations are carried out to obtain a binary map with distinct connected domains; (2) The contour of each region is extracted, the index value is assigned to each contour, and the area of contour is calculated; (3) Find the contour index value maxindex with the largest enclosed area. (4) Traverse the contour. If the contour index value is not equal to maxindex, change the color of the enclosed area into black.

According to the above algorithm, the connected region with the largest area was left and the weld mask was obtained. Finally, the weld area could be obtained by matrix addition of the mask and the contrast enhanced gray image. The implementation process is shown in Fig. 6. Figure 6b describes the result of Fig. 6a after thresholding and morphological operation. It can be found that the weld area is the largest. It is necessary to extract the contour of each area and calculate the area enclosed by the contour to obtain the weld mask. The obtained weld mask is shown in Fig. 6c, and then Fig. 6c and Fig. 6a are added, and the final weld result is shown in Fig. 6d. Similarly, the same

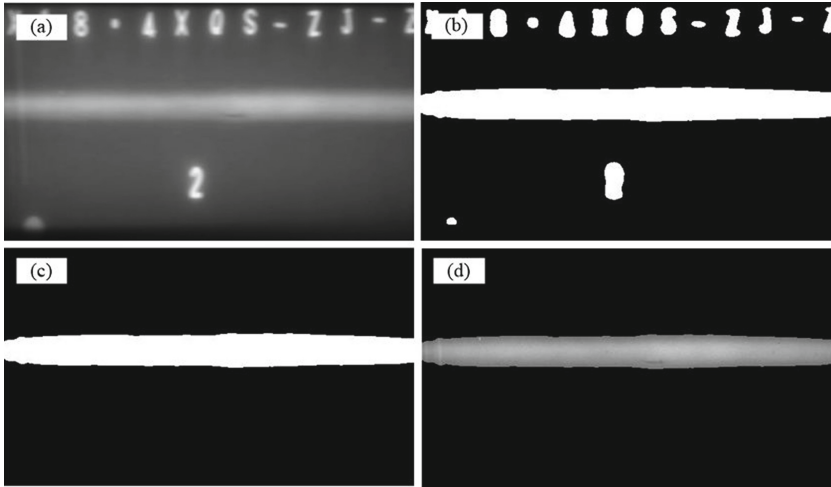


Fig. 6. The process of weld bead extraction: (a). image after preprocessing; (b). image after thresholding and morphological operation; (c). mask; (d). final result of weld extraction

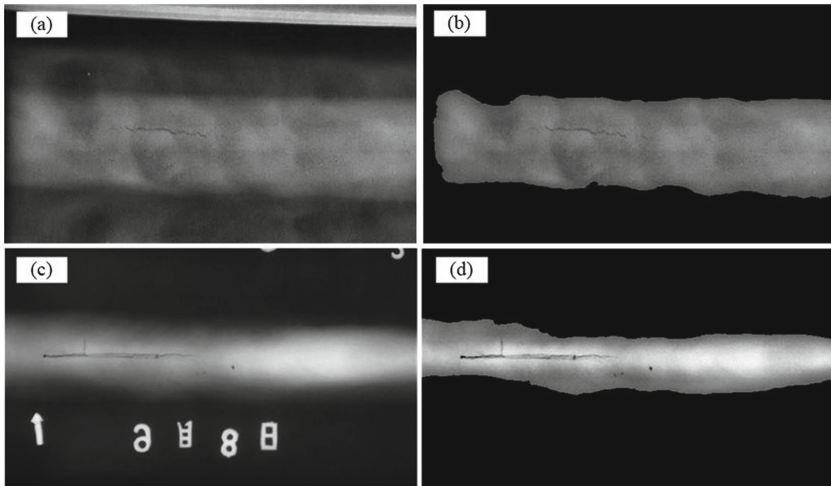


Fig. 7. Results of weld extraction: (a) (c). original images; (b) (d). results

algorithm is used to extract the other two X-ray welds after pretreatment, and the effect is shown in Fig. 7.

2.3 Defect Extraction Based on Local Threshold and Flood Filling

Local Thresholding. After the welding seam was segmented, the pixel level was divided into several categories by setting the threshold value according to the difference between the target and the background in the image, so as to realize the separation of the target and the background. The mathematical expression is as follows:

$$g(x, y) = \begin{cases} 1 & f(x, y) \geq T \\ 0 & f(x, y) < T \end{cases} \quad (4)$$

where $f(x, y)$ is the original gray value at the point (x, y) , and t is the gray threshold to distinguish the target from the background. It can be seen from the expression that the gray value of the pixel that is greater than or equal to the threshold value is set to 1, corresponding to the target in the image, while the gray value of the pixel smaller than the threshold value is set to 0, corresponding to the background in the image. Therefore, the effect of threshold segmentation depends on the selection of threshold.

In this paper, the local threshold was used for binary segmentation of the image. A pixel and its surrounding 5×5 pixels neighborhood were regarded as “local”. According to the two-dimensional Gaussian distribution function, the weighted sum is used as the threshold of the point, and all the pixels in the image are traversed. Finally, the image can be binarized and segmented. The expression of two-dimensional Gaussian distribution function is as follows:

$$G(x, y) = \frac{1}{2\pi\sigma^2} e^{-\frac{x^2+y^2}{2\sigma^2}} \quad (5)$$

Figure 8a shows the result of local binarization. It can be seen that the weld edges and defects are almost extracted, and the contour is very clear, which can basically represent the information transmitted to the brain by the human eye when observing the image. However, there are some white noises inside the weld, and the weld boundary is not smooth enough, so it is necessary to filter the binary image. Figure 8b shows the result of 5×5 template mean filtering. It can be observed that some smaller noise points are well suppressed, and the larger noise points are also weakened. The Otsu global threshold processing can make the noise pixel value be replaced by 0, and the foreground is further highlighted. The final local threshold processing results are shown in Fig. 8c.

Flood Filling. After the binary image of weld was obtained by local threshold method, defects needed to be segmented. As shown in Fig. 8c, the adaptive thresholding eliminates the weld background, leaving weld boundaries and defects. According to the conventional idea, only two weld boundaries needed to be removed, filtering and morphological operations were then carried out to get the target. However, this idea is desirable for the processing of a single radiograph, and the parameters of the algorithm also need to be changed for different radiographic images. It is obvious that traditional idea for eliminating weld boundary remains low adaptability. Flooding filling is commonly used in

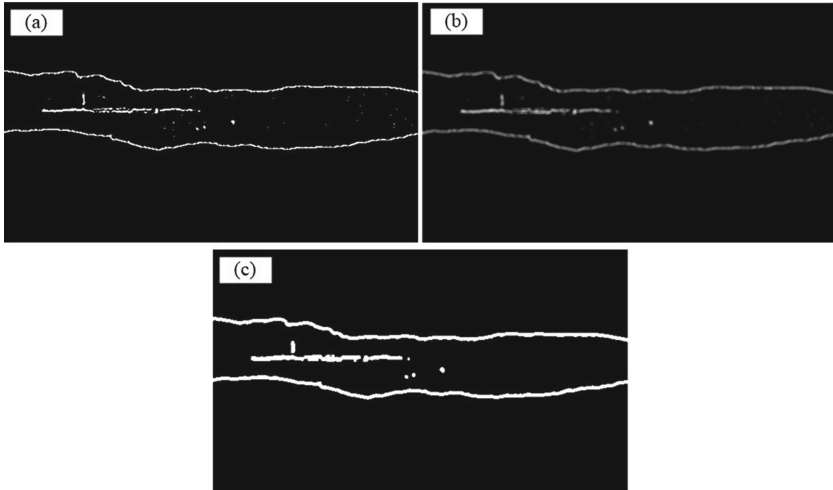


Fig. 8. The process of local thresholding: (a). the result of local thresholding; (b). the result of mean filtering; (c). the result of Otsu thresholding

graphics rendering software. Only by setting the starting point of filling pixel, the closed area where the point is located can be filled into a new color. The weld seam just forms the closed area in the image, and the starting point of the filling pixel can be determined according to the size of the image. Opencv provides a flood fill function (`floodfill()`), which is implemented as follows: (1) Mark the pixel of seed (x, y); (2) The color of the point is detected. If it is different from the boundary color and the fill color, the point is filled with the fill color, otherwise it is not filled; (3) Detect the adjacent place and turn back to step (2). There are two kinds of adjacent pixels: four-way connectivity and eight term connectivity (Fig. 9).

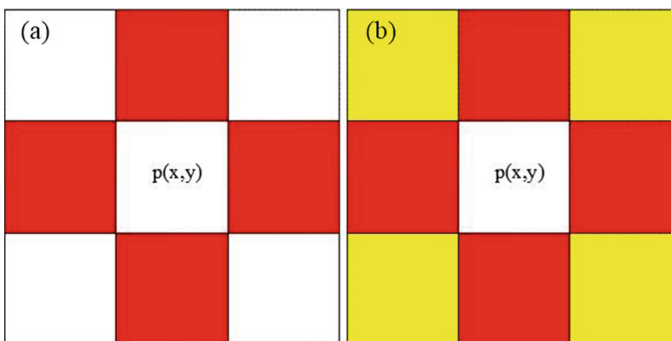


Fig. 9. (a). four connected region; (b). eight connected region

Figure 10 shows the process of defect extraction by flood filling. Flood filling was carried out according to the two starting points F1 and F2 shown in Fig. 10a. The filling color was white, and the result is shown in Fig. 10b. It can be found that the outside of the weld area turns to white, and then it is only necessary to fill the outside of the weld area once more. The filling color was set to black, and still F1 and F2 were set to the starting points, the defect could then be segmented. The results of secondary flooding filling are shown in Fig. 10c. It can be seen that flooding filling can effectively eliminate the weld boundary.

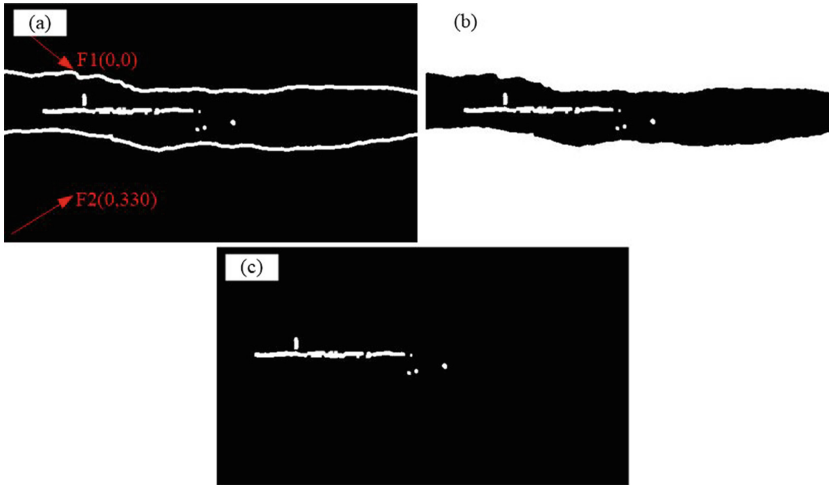


Fig. 10. The process of flood filling: (a). labelling of seeds; (b). first flooding filling; (c). second flood filling

Defect Labeling and Recognition. In order to verify the accuracy of the proposed algorithm, the extracted defects were drawn in the original image, and each contour was marked. The results are shown in Fig. 11 (b) (d) (f). The aspect ratio, circularity and effective area of each profile were calculated respectively. The calculation results are shown in Table 1. It can be found that the aspect ratio of crack defects is greater than 1.5, while the roundness of non-crack defects is close to 1. The calculated effective area can highlight the actual size of defects.

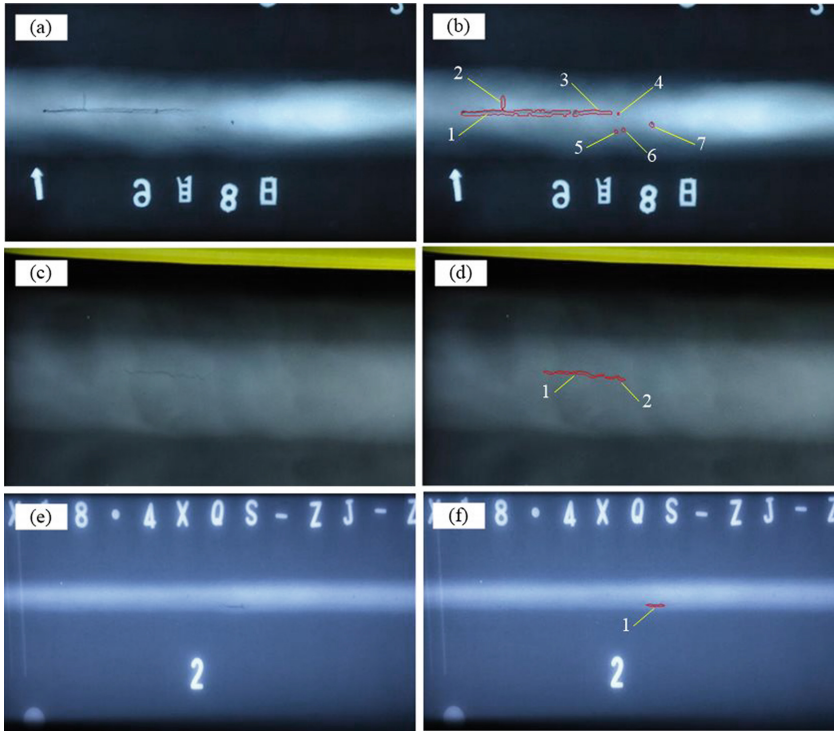


Fig. 11. The results of defect extraction: (a) (c) (e). original images; (b) (d) (f). detection results

Table 1. Table captions should be placed above the tables.

Image name	Contour index	Aspect ratio	Roundness	Effective area
Figure 11. (b)	1	16.67	0.091	2.51
	2	2.67	0.575	1.85
	3	6.55	0.213	2.08
	4	1.0	0.857	1.01
	5	1.5	0.754	0.6
	6	1.5	0.923	1.15
	7	1.25	0.913	1.55
Figure 11.(d)	1	10.69	0.075	1.104
	2	5.06	0.170	0.896
Figure 11. (e)	1	8.67	0.218	0.958

3 Conclusions

The length width ratio, roundness and effective area of the defects extracted were calculated. The length width ratio of the crack defect is greater than 1.5, and the roundness of the non-crack defect is close to 1. The defect recognition algorithm proposed in this paper can be used not only for the auxiliary evaluation of weld radiographic film, but also as a preprocessing step for classification and recognition of weld defects.

Acknowledgement. This work was supported by the National Natural Science Foundation of China (52065041, 51805234), China Scholarship Council (CXXM2012210002), the “double first-class” research project of the education department of Gansu province (GSSYLXM-03), and Lanzhou university of technology Supporting Program for Excellent Young Talents.

References

1. Nacereddine, N., Goumeidane, A.B., Ziou, D.: Unsupervised weld defect classification in radiographic images using multivariate generalized Gaussian mixture model with exact computation of mean and shape parameters. *Comput. Ind.* **108**(2019), 132–149 (2019)
2. Palenichka, R., Alekseichuk, A., Zscherpel, U.: Flaw detection in radiographic images by structure-adaptive binary segmentation. In: *Proceedings International Symposium On Computed Tomography for Industrial Applications and Image Processing in Radiology*, pp. 221–232 (1999)
3. Yan, Z.H., Xu, H., Huang, P.F.: Multi-scale multi-intensity defect detection in ray image of weld bead. *NDT E Int.* **116**(2020), 102342 (2020)
4. Hou, W., Zhang, D., Wei, Y., Guo, J., Zhang, X.: Review on computer aided weld defect detection from radiography images. *Appl. Sci.* **10**(5), 1878 (2020)
5. Lin, Z., Zhang, Y., Dai, B., Li, Y.: Welding defect detection based on local Image Enhancement **13**(13), 2647–2658 (2019)
6. Zou, Y., Du, D., Chang, B., Pan, J.: Automatic weld defect detection method based on Kalman filtering for real-time radiographic inspection of spiral pipe. *NDT E Int.* **72**(2015), 1–9(2015),
7. Malarvel, M., Sethumadhavan, G., Bhagi, P.C.R., Kar, S., Krishnan, A.: Anisotropic diffusion based denoising on X-radiography images to detect weld defects **68**(2017), 112–126 (2017)
8. Ma, J., Wang, Y., Shi, C., Lu, C.: Fast surface defect detection using improved gabor filters. In: *2018 25th IEEE International Conference on Image Processing (ICIP)*, pp.1508–1512. Springer, Athens (2018)
9. Guo, H., Shao, W., Zhou, A., Yang, Y., Liu, K.: Novel defect recognition method based on adaptive global threshold for highlight metal surface. *Chin. J. Sci. Instrum.* **38**(11), 2797–2804 (2017)
10. Alaknanda, Anand, R.S., Kumar, P.: Flaw detection in radiographic weld images using morphological approach. *NDT E Int.* **39**(1), 29–33 (2005)
11. Zhou, P., Wang, F., Xiao, H., Ao, B.: Automatic detection and recognition of gas pores in DR images. *Nondestruct. Test.* **39** (10), 37–40 (2017)
12. Alaknanda, Anand, R.S., Kumar, P.: Flaw detection in radiographic weldment images using morphological watershed segmentation technique. *NDT E Int.* **42**(2009), 2–8 (2009)
13. Yana, B., Lia, Y., Rena, S., Mukriz, I., Abidin, Z.: Recognition and evaluation of corrosion profile via pulse-modulation eddy current inspection in conjunction with improved Canny algorithm. *NDT E Int.* **106**(2019), 18–28 (2019)

14. Centeno, T.M.: Automated detection of welding defects in pipelines from radiographic images DWDI. *NDT E Int. Independent Nondestr. Test. Eval.* **86**(2017), 7–13 (2017)
15. Dazhao, C., Ziqi, M., Yi, C., Ziming, W., Ziheng, T.: Single lap weld defect recognition based on X-ray image processing. *Welding* **65**(08), 1–4 (2019)
16. Qi, J., LI, J.: Feature extraction of welding defect based on machine vision. *China Weld.* **28**(1), 56–62 (2019)



MLD Classification Model of Visual Features of Multi-layer and Multi-pass Molten Pool During Robotic MAG Welding of Medium-Thick Steel Plates

Hao Zhou¹, Yinshui He², Huabin Chen^{1,3(✉)}, and Shanben Chen^{1,3(✉)}

¹ Intelligentized Robotic Welding Technology Laboratory, School of Materials Science and Engineering, Shanghai Jiao Tong University, Shanghai 200240, People's Republic of China
{hbchen, sbchen}@sjtu.edu.cn

² School of Resources Environmental and Chemical Engineering, Nanchang University, Nanchang 330031, China

³ Shanghai Key Laboratory of Materials Laser Processing and Modification, School of Materials Science and Engineering, Shanghai Jiao Tong University, Shanghai 200240, People's Republic of China

Abstract. Molten pool image segmentation and feature extraction based on vision sensor is one of the core tasks of robotic automated welding. The Geodesic active contour model (GAC) method is used for the molten pool image in the multi-layer and multi-pass welding process (non-swing welding), and the molten pool contour can be effectively separated from the two-dimensional image obtained by the welding vision sensor. Through further analysis of the extracted contour, calculation of melting width, comprehensive evaluation of the radius of curvature of the front, upper and lower ends of the molten pool, the molten pool in multi-layer multi-pass welding can be divided into seven types. Corresponding to the seven forming conditions in multi-layer and multi-pass welding, the MLD classification model is established. The experimental results show that the image segmentation method based on GAC can effectively obtain the edge of MAG weld pool. The characteristics of weld pool can be exactly corresponding to the seven types of multi-layer and multi-pass, which lays a foundation for the MLD dynamic control of welding.

Keyword: Robotic MAG · Molten pool · Multi passes · GAC · Image segmentation · Feature extraction · MLD classification

1 Introduction

As a relatively mature process, arc welding is widely used in heavy industry, especially in the fields of energy, transportation, chemical engineering and marine engineering [1]. The plate members in these fields are mostly composed of steel structures, and the plate exceeding 10 mm often need to be formed by multi-layer multi-pass welding [2, 3]. As a new process of MAG welding, CMT welding method has the advantage of

reducing welding heat input and welding spatter, reducing welding residual stress and welding distortion compared with traditional MIG welding [4]. Usually this welding method is only suitable for Thin plate welding [5, 6]. In order to eliminate the process of heat treatment after the workpiece is welded, it is introduced and applied to the multi-layer and multi-pass welding process. At present, multi-layer and multi-pass welding are mainly traditional manual arc welding and semi-automatic welding, and the efficiency is relatively low; at the same time, the fumes and strong arc light generated during the welding process damage the health of the welder [7]. For to improve the production efficiency of multi-layer and multi-pass welding and free the welder from the harmful welding environment, higher requirements are put forward for modern welding intelligent manufacturing.

In order to realize the automation and intelligence of welding manufacturing process, it is necessary to simulate professional welders with specific equipment and models. Chen et al. [1, 8] proposed the concept of Intelligent Welding Manufacturing Technology/System (IWMT/S), the core of which is to use welding robots for precise motion control of the welding process, and to realize automatic welding without any participation. From the perspective of multi-robots, a macro-task allocation model for multi-robot welding is established. Through the established welding expert system, complex welding tasks are decomposed and completed one by one [9–11]. Starting from the specific welding process, first obtain the sensor information during the welding process, including the voltage and current information of the arc, the molten pool information [12–14], the sound information [15, 16], and the spectral information [17–19]. Furthermore, a real-time control model is established through this information and feedback control of welding process parameters is performed [20].

In modern industrial processes, the control of hybrid systems with interactive continuous-time dynamic characteristics and discrete-time dynamic characteristics has become universal, and it is a hot research issue in the field of control research [21]. The automated robot welding process is a typical hybrid system dynamic control process, which includes the robot posture, the robot's motion process and the continuous and discrete dynamics of the welding equipment operation process [22–24]. By analyzing the continuous and discrete dynamics of the dynamic process of the molten pool, combining the visual information of the welding process of the wrong edge and gap, and abstracting it into discrete variables, Ma established the misalignment molten pool mixed logic dynamic model [25] and the gap molten pool mixed logic dynamics model [26], which provides an effective estimate for penetration control.

To realize the intelligent welding process, it is necessary to process the images collected during the welding process to obtain important information in the welding process. The characteristics of the molten pool play an important role in weld formation and welding quality inspection. Because the welding environment changes greatly, there is no stable illumination, and the complex reflection characteristics of the molten pool surface and the intense light intensity of the arc are disturbed, the edge of the molten pool image is difficult to obtain effectively. In order to obtain a stable and accurate edge of the molten pool, many scholars have done a lot of research work [27]. Zou et al. [28] first used the Haar wavelet to filter the molten pool image, and then binarized the pool image by directly setting the threshold. Shen et al. [29] used the Robert operator method

to perform edge detection on the molten pool image and then perform refinement to obtain the center of the molten pool. In the traditional image segmentation method [30], the canny operator is not susceptible to noise interference. Two different thresholds are used to detect the strong edge and the weak edge respectively, and when the weak edge and the strong edge are connected, the weak edge is included in the output image. Kong et al. [12] used the canny operator to perform edge detection on the TIG's weld pool to obtain the edge of the weld pool. The edges of these weld pools also include some interference information, which needs further filtering.

Xu et al. [31] proposed an improved Canny operator for edge detection of molten pool images. In this algorithm, a nonlinear anisotropic diffusion filter is first used instead of a Gaussian filter, then the Otsu algorithm is used to automatically adjust the high and low thresholds, and then the adjusted threshold is used to detect and connect the edges of the image. In laser welding, zheng et al. [32] based on the shape of the molten pool is a prior knowledge of the closed convex profile. The active contour model based on the closed convex shape is established, and the stable laser welding pool segmentation result is obtained.

The demand for multi-layer and multi-pass welding used in heavy industry is very large, and many researchers are studying multi-layer and multi-pass welding planning [2, 3]. However, starting from the welding pool, there are relatively few researches on the image characteristics of multi-layer and multi-channel welding pools, and the establishment of feedback control models for welding parameters based on the image characteristics. In this article, we mainly analyze the molten pool of multi-layer and multi-pass non-swing welding and related forming, find the rules and classify the molten pool, and provide a basis for establishing the relevant MLD model.

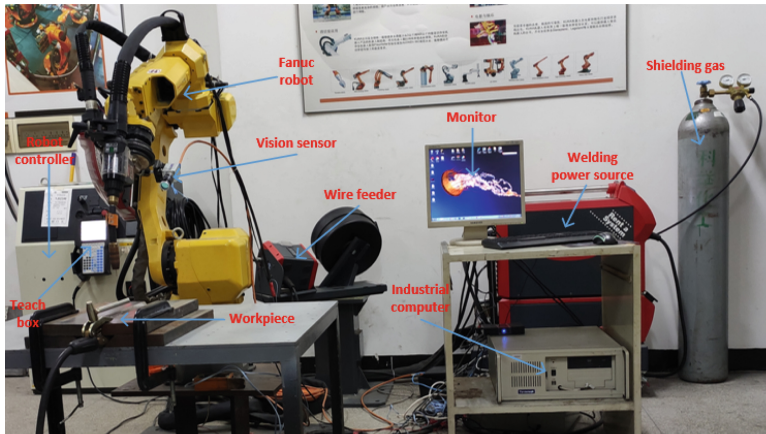
2 Experimental System and Image Acquisition

2.1 Experimental System

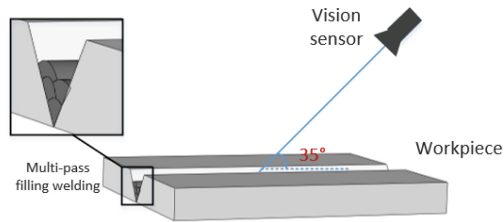
The complete experimental system is shown in Fig. 1a, which consists of three parts: MAG system, Fanuc robot motion system, molten pool image acquisition system. The MAG system mainly refers to the Fronius TPS 400i welding source, which includes MAG power, wire feeder, liquid-cooled tank, welding torch, and gas cylinder (80% argon and 20% carbon dioxide as shielding gas). The robot Fanuc motion system is composed of the six-axis robot body, the robot motion controller, and the teaching box.

The vision sensor includes a high dynamic range camera (Xiris XVC-1000), (what filter and dimming film are added, the transmittance is 80%), which is installed under the robot flange through a universal bracket. The horizontal direction of the sensor to the welding workpiece is 35° (as shown in Fig. 1.c), and the distance from the camera to the tip of the welding wire is 190 mm.

The composition of the multi-layer and multi-pass welding base metal involved in this paper has dimensions shown in Table 1, the schematic diagram is shown in Fig. 2, and the welding parameter table is shown in Table 2.



(a)



(b)

Fig. 1. (a) The whole experimental system. (b) The position relationship between the vision sensor and the welding workpiece.

Table 1. Information of the base metal.

Welding materials	Thickness	Groove angle	Type of weld seam
Q235	30 mm	30°	Butt joint

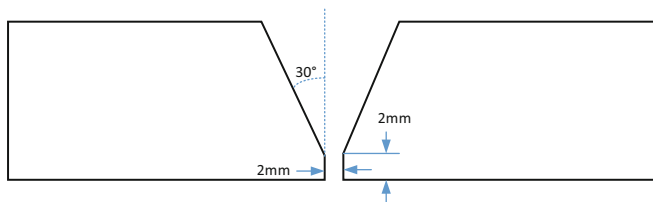


Fig. 2. Schematic diagram of welding base metal size.

Table 2. MAG welding parameters.

Welding parameters	Value
Welding type	CMT
Welding speed (mm/min)	240
Backing welding current (A)	170–185
filling welding current (A)	210–280
Angle of torch (°)	–15–15
Air flow (L/min)	1.5
Dimensions of workpiece (mm)	400 × 150 × 30

2.2 Image Acquisition

The Xiris molten pool vision sensor can collect 25 grayscale images of the molten pool every second, and the size of the grayscale image is 300 * 300 pixels. Taking the bottom welding and the first pass of the 3rd layer as an example, the corresponding weld pool image is shown in Fig. 3.

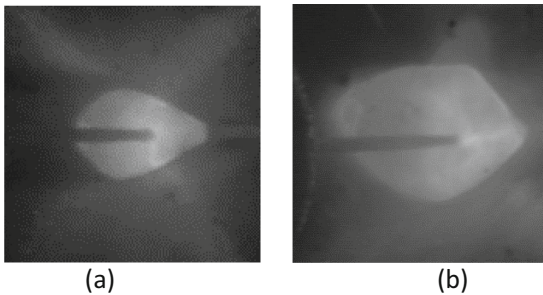


Fig. 3. Typical multi-pass weld pool image. (a)The pool image of backing. (b) The pool image of backing first pass of the 3rd layer.

3 Multi-layer and Multi-pass Forming Analysis

The theoretical modes of multi-layer and multi-pass welding are generally divided into three situations, as shown in Fig. 4; they are triangular forming, trapezoidal forming and parallelogram forming.

Through many welding experiments, the welding sequence of multiple layers and multiple passes is shown in Fig. 5. The principle of welding planning is the welding sequence of the two sides first and then the middle.

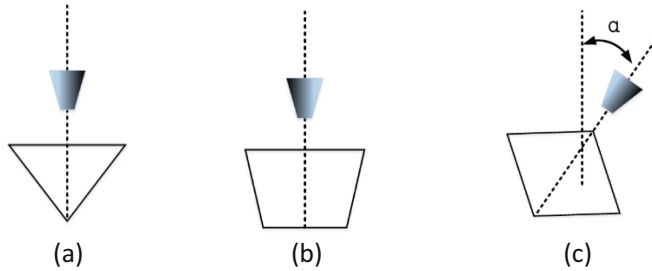


Fig. 4. (a) triangular forming. (b) trapezoidal forming (c) parallelogram forming.

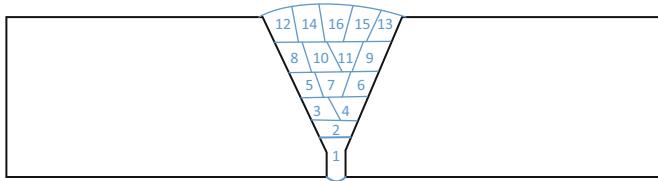


Fig. 5. Multi-layer and multi-pass welding sequence for 30 mm thick plates

In the process of multi-layer and multi-pass welding, since there are many welding layers, it is necessary to classify the welding pool through the corresponding theoretical model:

From the analysis of the multi-layer and multi-pass welding plan, the triangular shape is the backing welding.

(1) Triangle forming (Type 1)

The molten pool of the Type 1 is shown in Fig. 6.

The welding current of the back welding is about 175A, and the current is relatively small. Due to the restriction of the side wall of the groove, the included angle at the front end of the molten pool is a small acute angle.

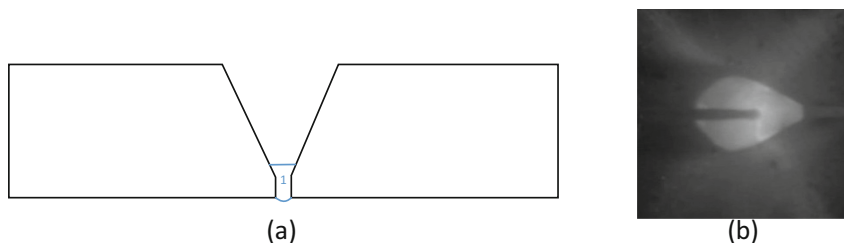


Fig. 6. (a) Schematic diagram of weld bead filling. (b) (a) corresponding molten pool image.

(2) Trapezoidal forming

There are generally three types of trapezoid formation: the first is shown in Fig. 7, where the weld bead is formed on the basis of the bottom welding, and the two sides of the molten pool are not restricted by the side walls; the second is shown in Fig. 8, The case where one side of the molten pool is a side wall and the other side is a weld bead; the third is shown in Fig. 8, where both sides of the molten pool are weld beads.

1) When welding grooves on both sides (Type 2):

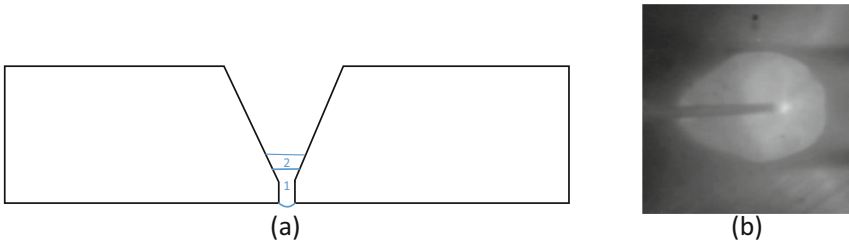


Fig. 7. (a) Schematic diagram of weld bead filling. (b) (a) corresponding molten pool image.

2) When one side is groove and the other is weld bead (Type 3):

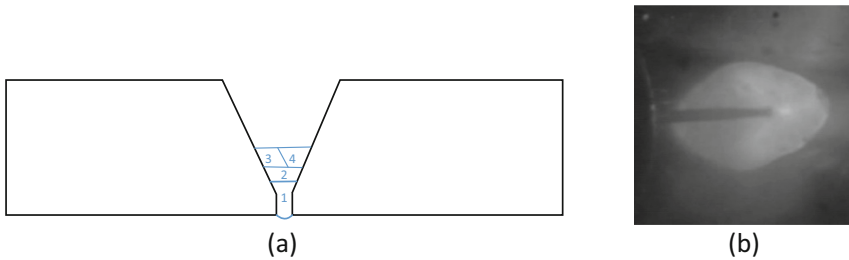


Fig. 8. (a) Schematic diagram of weld bead filling. (b) (a) corresponding molten pool image.

3) When both sides are weld beads (Type 4) (Fig. 9):

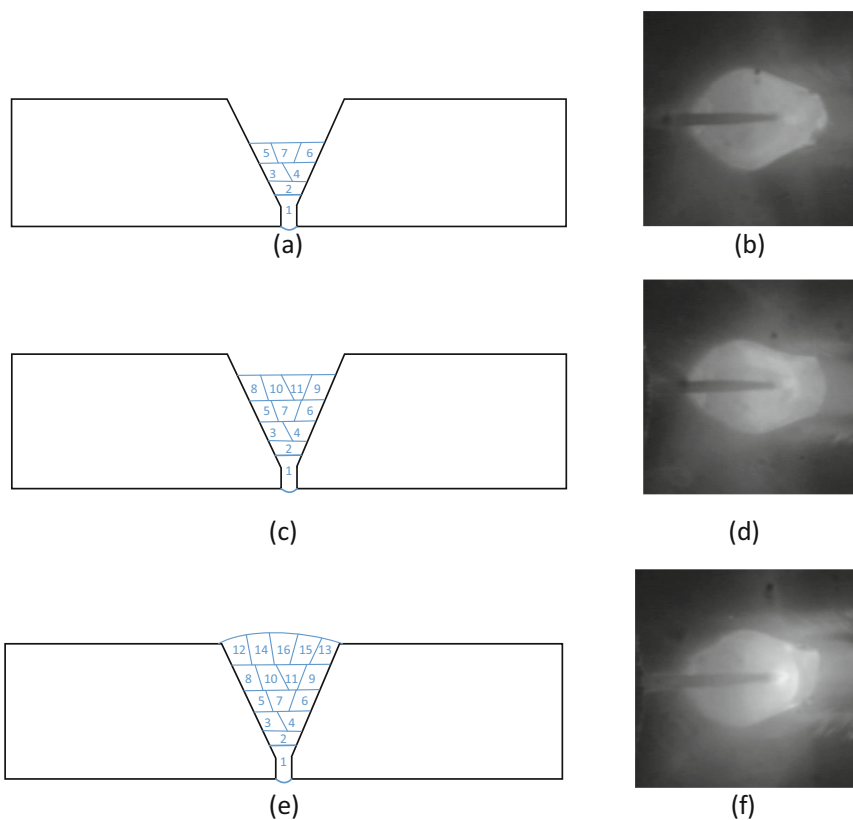


Fig. 9. (a) (c) (e) Schematic diagram of weld bead filling. (b) (d) (f) (a) (c) (e) corresponding molten pool image.

(2) Parallelogram forming

There are three types of parallelogram formation of weld beads: the first is the case where one side is the side wall, as shown in Fig. 10; the second is the case where one side is the weld, as shown in Fig. 11; This is the case of cover welding, as shown in Fig. 12.

- 1) When one side is groove (Type 5):
- 2) When one side is the weld bead (Type 6):
- 3) In the case of cover welding (Type 7):

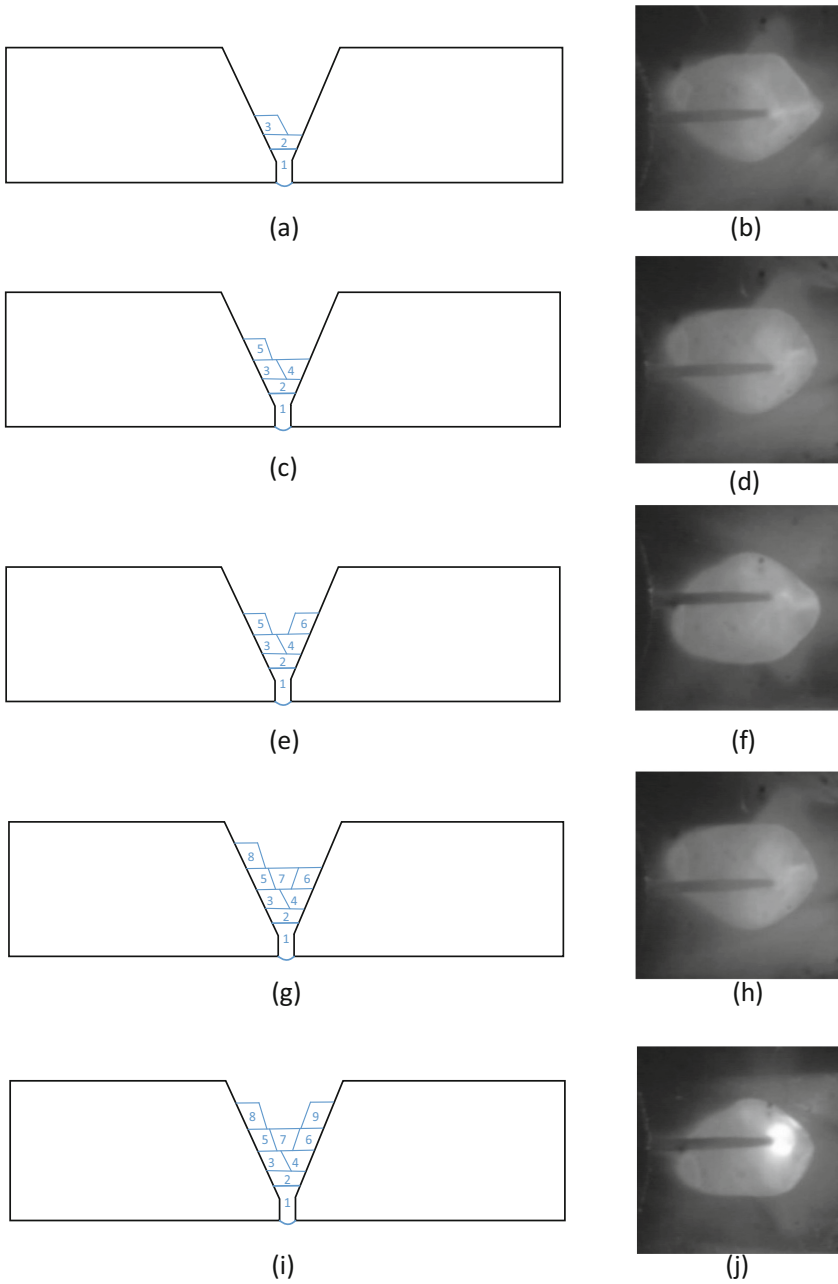


Fig. 10. (a) (c) (e) (g) (i) Schematic diagram of weld bead filling. (b) (d) (f) (h) (j) (a) (c) (e) (g) (i) corresponding molten pool image.

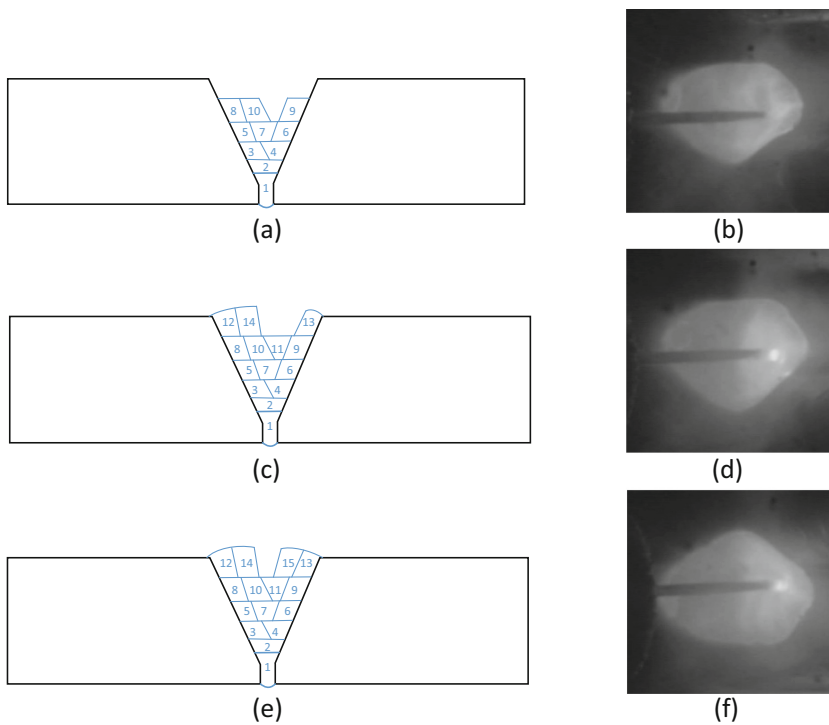


Fig. 11. (a) (c) (e) Schematic diagram of weld bead filling. (b) (d) (f) (a) (c) (e) corresponding molten pool image.

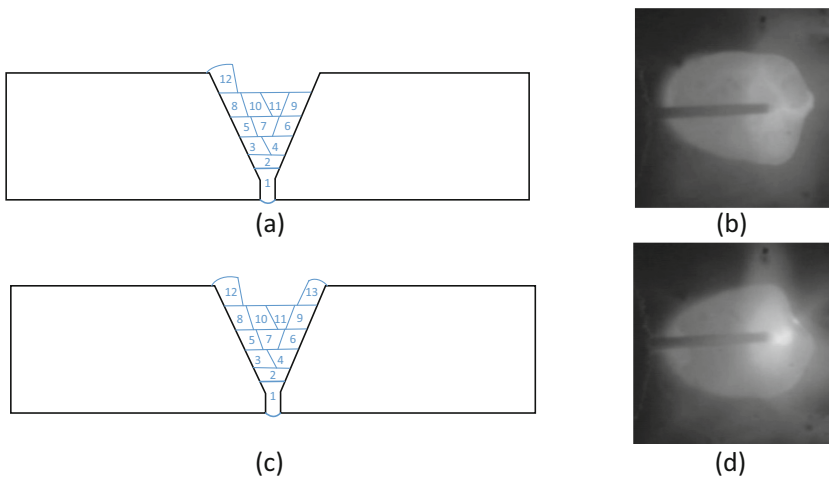


Fig. 12. (a) (c) Schematic diagram of weld bead filling. (b) (d) (a) (c) corresponding molten pool image.

In a word, starting from the three theoretical models of multi-layer and multi-pass forming, after specific forming analysis, all types of weld bead can be divided into 7 types, which represent the types of typical multi-layer and multi-pass forming.

4 Multi-layer and Multi-pass Welding Pool Features Extraction

The flow of multi-layer and multi-pass molten pool feature acquisition is shown in Fig. 12 below. First of all, checkerboard calibration is performed on the area of the weld pool. The purpose of calibration is to obtain the actual melting width and length. The second is to use the Geodesic active contour model (GAC) method to segment the molten pool image. After obtaining the edge curve of the image, divide the edge curve into three parts, the upper half of the molten pool, the lower half, and the right part. Fit the three curve parts of the molten pool and calculate their radius of curvature respectively. According to the different types of multi-layer and multi-pass forming, it is judged by the obtained radius of curvature and combined to obtain the characteristic information of the molten pool.

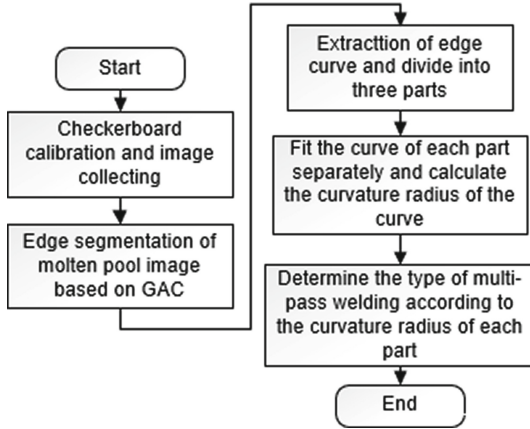


Fig. 13. Multi-layer and multi-pass welding pool image feature extraction flowchart.

4.1 Image Calibration

In this study, the actual width and length of the molten pool need to be obtained, so the image of the molten pool needs to be calibrated. As shown in Fig. 13, the blue arrow is the x direction and the red arrow is the y direction. The size of the checkerboard is 9 * 9 mm (Fig. 14).

The calibration values obtained in the x direction and y direction are:

$$k_x = 9 / \sqrt{(x_2 - x'_2)^2 + (y_2 - y'_2)^2} = 0.147461 \text{ mm/pixel}$$

$$k_y = 9 / \sqrt{(x_1 - x_2)^2 + (y_1 - y_2)^2} = 0.075606 \text{ mm/pixel}$$

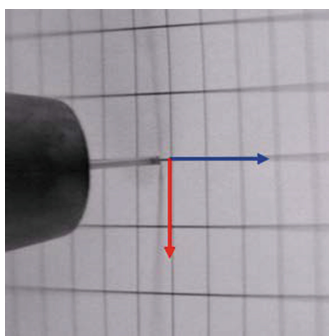


Fig. 14. Multi-layer and multi-pass welding pool image feature extraction flowchart.

4.2 Image Segmentation

The segmentation of weld pool image is the basis of welding vision to obtain information. It is the first step in the subsequent processing of weld pool geometric features, classification and feedback control, and it is also a difficult problem in weld pool image processing. Geodesic active contour(GAC) [33] model based on curve evolution theory and level set method is widely used in edge detection, image segmentation and other fields. In plane image segmentation, it expresses the 2-dimensional evolution curve as the zero level set of a high one-dimensional 3-dimensional continuous function, and the level set function is defined as the symbol distance function of the evolution curve, which can better deal with the change of the curve topology. Therefore, the GAC model is used to segment the molten pool image, and the specific segmentation process is shown in Fig. 15.

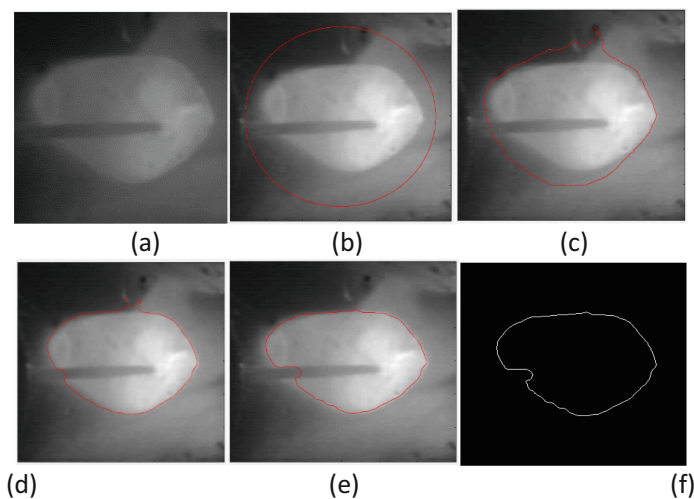


Fig. 15. Use GAC model to segment the pool image.

4.3 Weld Pool Feature Extraction

After obtaining the edge of the molten pool, the next step is to obtain the edge curve of the molten pool. Taking the first molten pool of the fourth layer as an example, Fig. 15(a) shows the original image of the molten pool, and Fig. 16(a) shows the three parts of the molten pool that need further analysis. Figure 16(b) shows the segmentation of the molten pool through the GAC; Fig. 16(c) shows the edge curve of the molten pool, that is, the upper part, the lower part, and the right part of the molten pool. Figure 16 (d), (f), (h) are the three curve divisions of the molten pool, and Fig. 16 (e), (g), (i) are the corresponding curve fittings.

Now define each characteristic parameter of the molten pool:

W is the weld width, and L is the weld length. R_t is the maximum curvature radius of the upper curve of the molten pool, R_{tr} is the maximum curvature radius of the upper curve of the molten pool. R_r is the maximum curvature radius of the right curve of the molten pool, R_b represents the maximum curvature radius of the lower curve of the molten pool, and R_{br} represents the maximum curvature radius of the lower right portion of the curve of the molten pool.

(1) Triangle, type 1:

It can be analyzed from the welding current that the current of the bottom welding is generally 175A, which is quite different from the welding current of the fill welding, so the type of bottom welding can be distinguished intuitively from the melting width (Fig. 17 and Table 3).

Through statistics, the criteria are as follows:

$$\begin{aligned} u_w &\leftrightarrow W \leq 115 \\ pc_1 &\leftrightarrow u_w \end{aligned} \quad (4-1)$$

(2) Trapezoid, type 2 (Fig. 18 and Table 4):

The criteria are as follows:

$$\begin{aligned} u_{rt2} &\leftrightarrow |R_t| < 115 \\ u_{rr2} &\leftrightarrow |R_r| < 50 \\ u_{rb2} &\leftrightarrow |R_b| < 115 \\ u_{bbt2} &\leftrightarrow ||R_b| - |R_t|| < 35 \\ pc_2 &\leftrightarrow \neg u_w \wedge u_{rt2} \wedge u_{rr2} \wedge u_{rb2} \wedge u_{bbt2} \end{aligned} \quad (4-2)$$

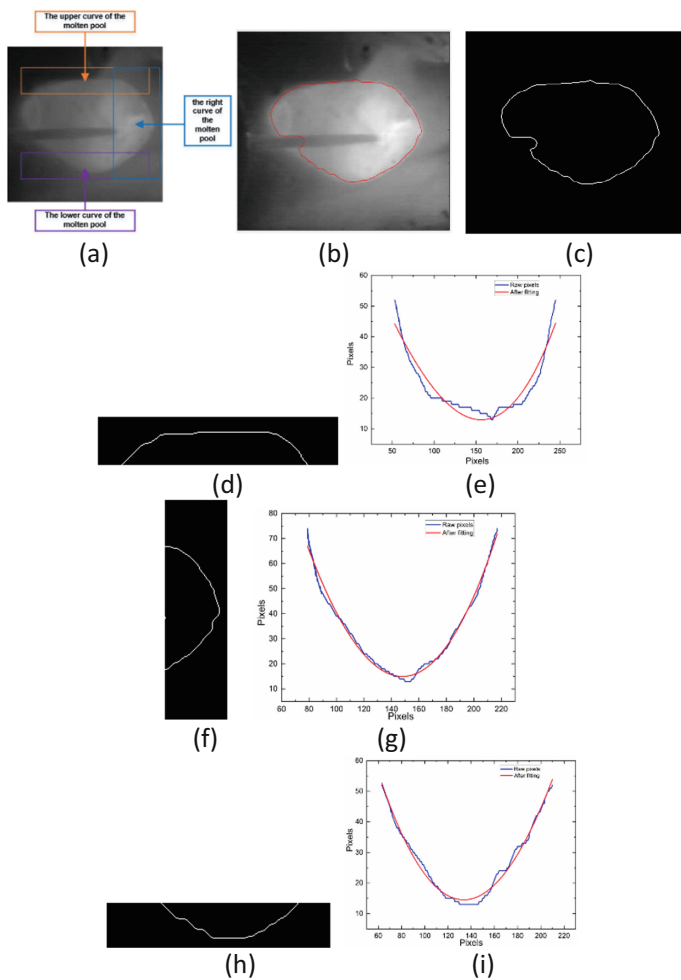


Fig. 16. Three-part curve acquisition of multi-layer and multi-pass MAG welding pool. (a) The three parts of the molten pool that need further analysis. (b) The pool image after binarization. (c) Edge curve of molten pool. (d), (f), (h) The three curve divisions of the molten pool. (e), (g), (i) The curve fitting corresponding to figure (d), (f), (h).

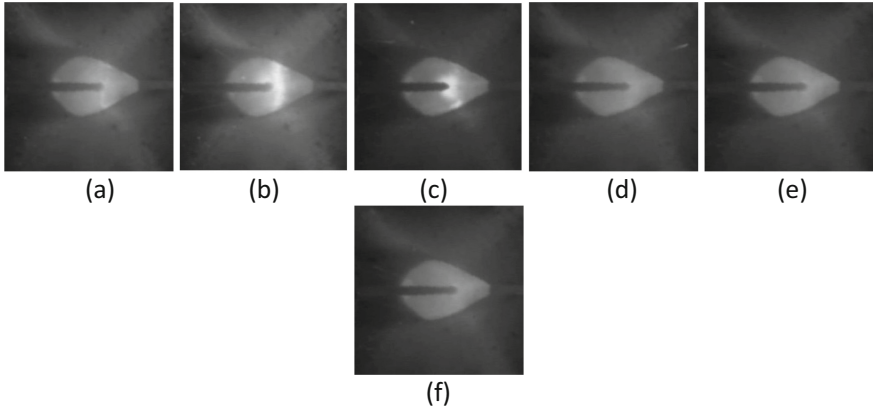


Fig. 17. The molten pool of the type 1 (backing weld) bead. (a)–(e) are five randomly selected molten pool images. (f) To randomly select a molten pool image for verification

Table 3. Type 1 of molten pool parameters.

W	L
105	153
105	156
105	156
107	157
107	161
107	163

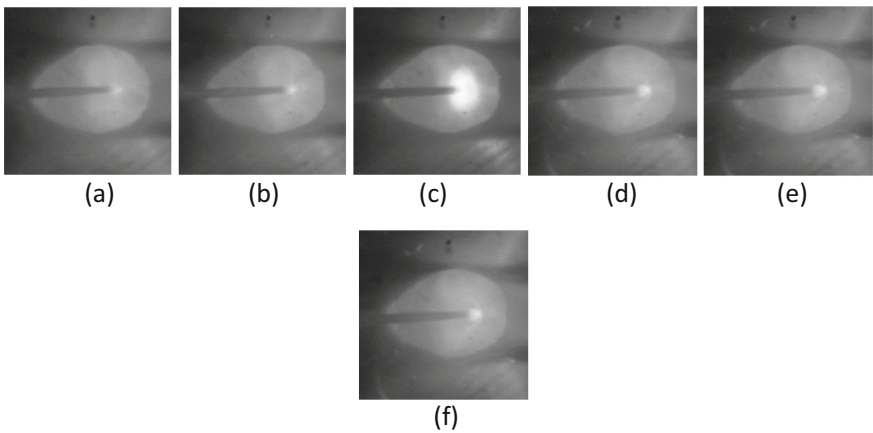


Fig. 18. The molten pool of type 2. (a)–(e) are five randomly selected molten pool images. (f) is to randomly select a molten pool image for verification.

Table 4. Type 2 of molten pool parameters.

W	L	R _t	R _r	R _b	R _{br}
159	215	79.276	33.7535	46.7916	103.9456
159	215	82.9049	38.0113	44.8293	113.2096
159	217	88.6734	61.8229	45.4542	107.0541
157	217	89.4454	57.922	45.9784	103.6563
157	218	95.0685	69.692	44.6619	102.0378
158	218	92.3826	65.2369	45.7832	104.5244

(3) Trapezoid, type 3 (Fig. 19 and Table 5):

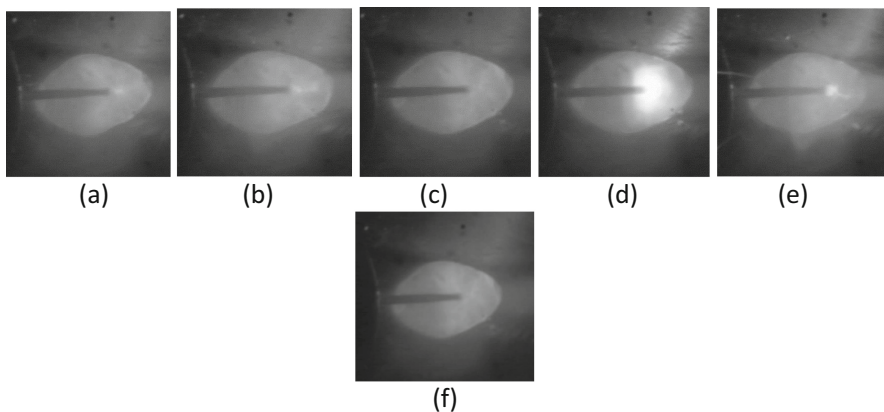


Fig. 19. The molten pool of type 3. (a)–(e) are five randomly selected molten pool images. (f) To randomly select a molten pool image for verification.

The criteria are as follows:

$$u_{rt3} \leftrightarrow |R_t| < 105$$

$$u_{rr3} \leftrightarrow 22 < |R_r| < 28$$

$$u_{rb3} \leftrightarrow |R_b| < 110$$

$$u_{bbt3} \leftrightarrow ||R_b| - |R_t|| < 10$$

$$pc_3 \leftrightarrow \neg u_w \wedge u_{rt3} \wedge u_{rr3} \wedge u_{rb3} \wedge u_{bbt3} \quad (4-3)$$

Table 5. Type 3 of molten pool parameters.

W	L	Rt	Rtr	Rr	Rb	Rbr
149	213	85.5911	197.8414	26.8985	85.9074	194.3363
147	221	83.8003	133.3447	27.3709	92.932	665.4702
147	219	90.3914	188.0991	26.2565	99.2006	325.4636
145	220	101.0607	211.8539	26.6252	106.4114	252.9662
145	221	97.3207	191.9639	24.7745	100.5413	694.1431
147	223	102.6654	217.9962	23.4133	109.5718	375.0627

(4) Trapezoid, type 4 (Fig. 20 and Table 6):

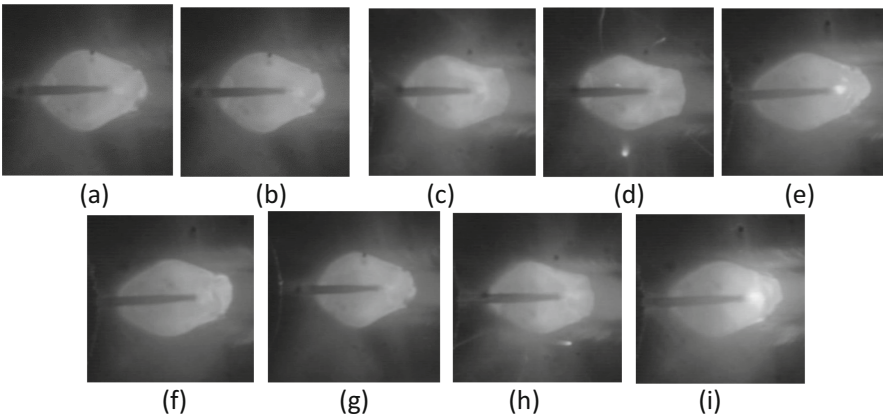


Fig. 20. The molten pool of type 4. (a)–(f) are two randomly selected molten pool images. (g)–(i) To randomly select a molten pool image for verification.

The criteria are as follows:

$$u_{rt4} \leftrightarrow 50 < |R_t| < 85$$

$$u_{rr4} \leftrightarrow 17 < |R_r| < 27$$

$$u_{rb4} \leftrightarrow |R_b| < 90$$

$$u_{bbt4} \leftrightarrow ||R_b| - |R_t|| < 21$$

$$u_{rtc4} \leftrightarrow R_{br} < 0$$

Table 6. Type 4 of molten pool parameters.

pass	W	L	Rt	Rtr	Rr	Rb	Rbr
7	143	193	56.3753	-5555.8552	23.3418	54.0618	-311.8901
	141	197	60.5102	-4978.9889	22.0322	57.7988	-174.0986
	143	193	64.3408	-4945.2167	23.1494	54.4977	-188.7877
	143	190	62.5592	-5226.144	23.5489	61.4746	-341.2367
	139	190	53.2057	-5206.568	20.4364	63.0447	-387.4696
11	131	195	60.106	-169.7276	24.3817	80.8584	-317.6024
	133	189	60.9807	-191.3551	24.2848	63.7415	-120.9918
	135	189	57.0138	-237.8718	26.5708	72.1065	-5094.479
	131	188	64.7271	-64.7271	25.7175	70.6339	-2407.798
	129	191	63.0117	-251.9374	24.5282	85.7223	-1855.276
16	137	209	79.3633	-221.4421	19.4788	84.8692	-2216.673
	131	193	75.0741	-700.8264	21.9214	65.5621	-963.2916
	139	204	84.1078	-305.1603	22.5752	76.277	-466.4149
	135	213	75.9227	-539.8999	18.3402	83.3682	-290.6306
	133	203	83.743	-209.298	21.4706	77.683	-7740.307
7	137	196	60.5792	-5306.8196	19.7811	65.9601	-349.3552
11	127	191	60.94	-375.2437	24.4326	87.0569	-668.3157
16	135	203	83.7501	-984.0019	19.8724	61.3134	-417.2899

$$u_{bt4} \leftrightarrow R_{br} < 0$$

$$pc_4 \leftrightarrow \neg u_w \wedge u_{rt4} \wedge u_{rr4} \wedge u_{rb4} \wedge u_{bbt4} \wedge u_{rtc4} \wedge u_{bt4} \quad (4-4)$$

(5) Parallelogram, type 5 (Fig. 21 and Table 7):

The criteria are as follows:

$$u_{rt5} \leftrightarrow 85 < |R_t| < 155$$

$$u_{rr5} \leftrightarrow 33 < |R_r| < 45$$

$$u_{rb5} \leftrightarrow 60 < |R_b| < 82$$

$$u_{bbt5} \leftrightarrow ||R_b| - |R_t|| < 85$$

$$pc_5 \leftrightarrow \neg u_w \wedge u_{rt5} \wedge u_{rr5} \wedge u_{rb5} \wedge u_{bbt5} \quad (4-5)$$

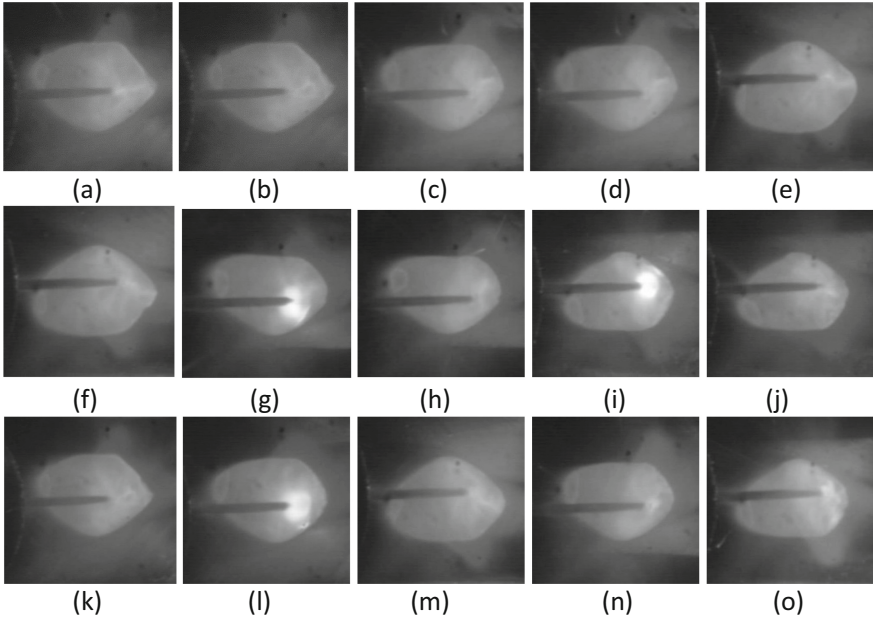


Fig. 21. The molten pool of type 5. (a)–(j) are two randomly selected molten pool images. (k)–(o) To randomly select a molten pool image for verification.

(6) Parallelogram, type 6 (Fig. 22 and Table 8):

The criteria are as follows:

$$u_{rt6} \leftrightarrow 80 < |R_t| < 138$$

$$u_{rr6} \leftrightarrow 30 < |R_r| < 47$$

$$u_{rb6} \leftrightarrow 53 < |R_b| < 73$$

$$u_{bbt6} \leftrightarrow ||R_b| - |R_t|| < 65$$

$$u_{btc6} \leftrightarrow R_{br} < 0$$

$$pc_6 \leftrightarrow \neg u_w \wedge u_{rt6} \wedge u_{rr6} \wedge u_{rb6} \wedge u_{bbt6} \wedge u_{btc6} \tag{4-6}$$

(7) Parallelogram, type 7 (Fig. 23 and Table 9):

Table 7. Type 5 of molten pool parameters.

pass	W	L	Rt	Rtr	Rr	Rb	Rbr
3	159	222	99.419	145.319	37.9801	78.8085	91.3605
	159	232	102.6757	127.9223	37.4002	76.8588	98.8327
	161	226	85.7161	126.4251	40.5345	78.5779	131.5777
	161	225	88.4945	60.5219	40.348	81.4894	133.62
	163	234	92.4032	43.0999	39.5433	76.6258	122.4742
5	153	221	147.6841	36.6504	44.9708	73.9984	200.0176
	153	217	131.4755	60.3901	41.0304	76.8382	102.4092
	151	218	114.9791	18.2926	44.1616	76.8368	73.3608
	151	217	114.8398	43.0148	44.3951	77.5024	282.1384
	155	209	102.1529	42.423	45.6374	71.6163	153.1936
6	160	220	73.5091	106.0315	41.0398	118.9931	41.8942
	161	219	66.8628	55.3658	41.3335	127.5468	34.0626
	161	217	70.6655	135.1551	40.2617	132.8812	43.8204
	157	218	68.9225	78.8941	39.4617	135.0497	51.7431
	157	219	69.4237	94.7675	39.3826	131.3384	38.4752
8	145	207	143.1609	75.34	34.1876	66.5981	464.626
	141	204	151.0228	21.5064	37.8685	71.6805	82.7574
	141	203	141.7465	27.4193	38.8503	68.6791	173.305
	141	203	146.5179	56.5966	37.8298	74.0481	103.058
	141	201	146.2478	32.5917	36.5269	73.6076	105.552
9	143	197	63.3954	115.4262	40.192	145.427	18.88
	141	199	62.1299	71.3367	39.8112	143.5173	54.2081
	141	202	68.239	96.6824	39.8355	139.6161	132.358
	141	204	66.0865	72.5481	39.6356	148.3546	45.0454
	139	201	66.7349	105.2763	39.9214	146.67	210.97
3	162	231	97.7938	47.113	38.4162	74.6338	115.294
5	151	211	101.5942	24.7872	43.6021	71.0419	407.268
6	158	216	68.5453	80.6139	38.3785	134.0264	38.1636
8	141	201	135.3096	179.9543	39.7619	71.6912	105.273
9	141	201	65.9604	350.1976	39.7983	129.2673	54.5188

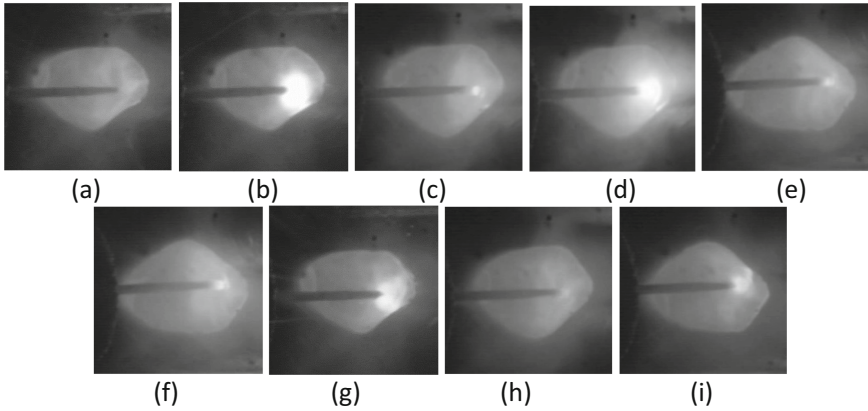


Fig. 22. The molten pool of type 6. (a)–(f) are two randomly selected molten pool images. (g)–(i) To randomly select a molten pool image for verification.

Table 8. Type 6 of molten pool parameters.

pass	W	L	Rt	Rtr	Rr	Rb	Rbr
10	151	207	104.0077	43.6882	32.374	59.004	-705.6589
	149	207	116.206	62.045	32.3293	63.8371	-100.0862
	149	209	132.0414	36.9397	32.0472	60.3521	-924.8026
	149	209	136.995	18.292	30.8752	58.8568	-288.5754
	151	210	123.5267	156.0458	34.1237	54.7122	-218.9153
14	167	215	112.6073	11.4513	42.7922	55.8002	-296.2293
	167	214	98.1487	16.4391	44.4472	61.4282	-453.7857
	167	216	82.7299	21.2447	42.3235	56.1501	-96.4655
	165	217	79.5456	27.664	45.4802	61.9466	-781.9262
	167	216	82.0002	75.5636	44.5167	57.8463	-92.2382
15	171	233	71.5709	-2340.716	45.2712	107.1723	24.3783
	171	231	71.2194	-130.4077	44.2595	115.2049	21.2203
	171	233	70.7274	-103.0834	44.4478	121.7682	37.2183
	169	225	70.9579	-3622.179	44.165	131.0743	14.3236
	165	219	64.8885	-392.794	43.7776	86.7009	32.3969
10	149	209	122.9329	26.4931	33.2848	55.6208	-331.5272
14	165	215	82.2734	43.9459	45.9019	60.2076	-1325.601
15	165	217	61.3678	-162.9544	40.0473	88.4657	65.2723

The criteria are as follows:

$$u_{rt7} \leftrightarrow |R_t| > 105$$

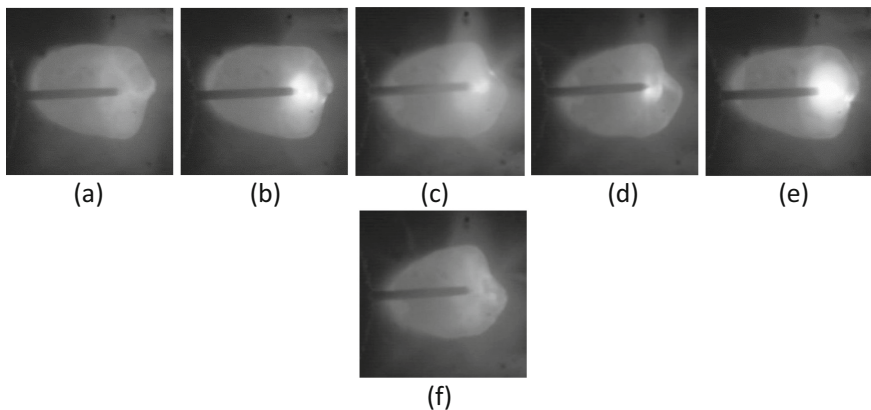


Fig. 23. The molten pool of type 7. (a)–(d) are two randomly selected molten pool images. (e) (f) To randomly select a molten pool image for verification.

Table 9. Type 7 of molten pool parameters.

pass	W	L	Rt	Rtr	Rr	Rb	Rbr
12	171	225	139.855	50.0167	57.9496	67.6126	12.1555
	171	237	155.3976	88.0362	57.2292	70.1374	9.4358
	167	233	129.5874	53.8201	56.5308	65.189	5.2882
	167	235	132.2024	22.8411	60.4113	66.9672	7.3035
	167	228	116.464	89.6201	62.349	68.6604	8.0859
13	171	223	51.5259	9.1902	48.7589	107.4615	66.483
	167	221	50.0318	8.2466	37.7043	142.8044	65.2548
	171	223	47.8157	5.5634	44.3116	115.0319	23.3683
	169	225	45.768	7.6619	42.3871	119.2906	29.0021
	167	224	43.5136	3.7836	43.0867	127.8094	31.7932
12	149	209	122.9329	26.4931	33.2848	55.6208	331.5272
13	165	215	82.2734	43.9459	45.9019	60.2076	1325.601

$$u_{rr7} \leftrightarrow 36 < |R_r| < 65$$

$$u_{rb7} \leftrightarrow 42 < |R_b| < 72$$

$$u_{bt7} \leftrightarrow |R_{br}| < 15$$

$$pc_7 \leftrightarrow \neg u_w \wedge u_{rr7} \wedge u_{rr7} \wedge u_{rb7} \wedge u_{bt7} \quad (4-7)$$

5 MLD Classification Model

The MLD system is a system described by interdependent physical laws, logical laws, and operational constraints. It transforms the heuristic knowledge, logical judgments, and constraints that must be observed by the operating objects into the form of propositional logic, and then the propositional logic is transformed into linear inequalities containing integers and continuous variables, thus realizing the integration of qualitative knowledge, expert experience, logical rules and operating constraints with physical laws.

The MLD model is a powerful tool for expressing hybrid systems. This chapter introduces the basic principles of MLD and the MLD classification model of multi-layer and multi-pass welding.

In MLD modeling means, a binary variable is assigned to each statement. If and only if the statement is true, the value of the binary variable is true.

$$x_a \equiv True \leftrightarrow \delta_a = 1 \quad (5-1)$$

The general form of the hybrid system based on MLD [34] is shown in (5-2):

$$\begin{cases} x(k+1) = Ax(k) + B_1u(k) + B_2\delta(k) + B_3z(k) \\ y(k) = Cx(k) + D_1u(k) + D_2\delta(k) + D_3z(k) \\ E_2\delta(k) + E_3z(k) \leq E_1u(k) + E_4x(k) + E_5 \end{cases} \quad (5-2)$$

Where x is the state vector of the system, y is the output variable including continuous output and logic output, u is the continuous input and logic input. δ and z are logical and continuous auxiliary variables, respectively. Equation (5-2) includes mixed integer inequality and operating constraints. E_1, E_2, E_3, E_4, E_5 are the matrices of appropriate dimensions respectively.

After analyzing the characteristics of the multi-layer and multi-pass weld pool image, the result obtained is seven types of weld bead ((4-1)–(4-7)), then seven logical variables are introduced to define the MLD weld pool classification model as follows ((5-3)–(5-9)):

$$[\delta_1 = 1] \leftrightarrow [pc_1 = u_w] \quad (5-3)$$

$$[\delta_2 = 1] \leftrightarrow [pc_2 = \neg u_w \wedge u_{rt2} \wedge u_{rr2} \wedge u_{rb2} \wedge u_{bbt2}] \quad (5-4)$$

$$[\delta_3 = 1] \leftrightarrow [pc_3 = \neg u_w \wedge u_{rt3} \wedge u_{rr3} \wedge u_{rb3} \wedge u_{bbt3}] \quad (5-5)$$

$$[\delta_4 = 1] \leftrightarrow [pc_4 = \neg u_w \wedge u_{rt4} \wedge u_{rr4} \wedge u_{rb4} \wedge u_{bbt4} \wedge u_{rtc4} \wedge u_{btc4}] \quad (5-6)$$

$$[\delta_5 = 1] \leftrightarrow [pc_5 = \neg u_w \wedge u_{rt5} \wedge u_{rr5} \wedge u_{rb5} \wedge u_{bbt5}] \quad (5-7)$$

$$[\delta_6 = 1] \leftrightarrow [pc_6 = \neg u_w \wedge u_{rt6} \wedge u_{rr6} \wedge u_{rb6} \wedge u_{bbt6} \wedge u_{btc6}] \quad (5-8)$$

$$[\delta_7 = 1] \leftrightarrow [pc_7 = \neg u_w \wedge u_{rt7} \wedge u_{rr7} \wedge u_{rb7} \wedge u_{bt7}] \quad (5-9)$$

6 Conclusions

In this paper, the image segmentation of multi-layer and multi-pass molten pool, corresponding forming classification and MLD classification model are studied. Related works including:

1. Established a multi-layer multi-pass welding pool image acquisition system.
2. The uneven brightness and blurred edges of the molten pool image show the complexity of its edge segmentation. GAC can effectively segment the edges of the molten pool image, with short detection time and high accuracy. It can also be effectively segmented under uneven lighting conditions.
3. By analyzing the multi-pass molten pools, the different layers can be divided into 7 categories, and the characteristics of the corresponding molten pools in each category have their own characteristics. Through the analysis and summary of the experimental data, the category assignment is determined, which provides the basis for the subsequent logical switch of the MLD(mixed logic dynamic) control model.

The significance of multi-layer and multi-pass welding MLD modeling is to simplify the welding process of the complex robot welding intelligent system into a control process in which logical variables and linear equations interact and automatically switch. The next step is to establish the differential equations under the conditions of different types of molten pools (layer types), which quantitatively express the thermal inertia in the multi-layer and multi-pass welding process and use it to control the welding formation.

Acknowledgements. This work is partly supported by the National Natural Science Foundation of China under the Grant No. 61873164.

References

1. Chen, S.-B.: On intelligentized welding manufacturing. In: Tarn, Tzyh-Jong., Chen, Shan-Ben., Chen, Xiao-Qi. (eds.) *Robotic Welding, Intelligence and Automation*. AISC, vol. 363, pp. 3–34. Springer, Cham (2015). https://doi.org/10.1007/978-3-319-18997-0_1
2. Yang, C., et al.: Multi-pass path planning for thick plate by DSAW based on vision sensor. *Sens. Rev.* (2014)
3. Chen, Y., Yang, C., Chen, H., Zhang, H., Chen, S.: Microstructure and mechanical properties of HSLA thick plates welded by novel double-sided gas metal arc welding. *Int. J. Adv. Manuf. Technol.* **78**(1–4), 457–464 (2014). <https://doi.org/10.1007/s00170-014-6477-0>
4. Selvi, S., Vishvaksean, A., Rajasekar, E.: Cold metal transfer (CMT) technology-an overview. *Defence Technol.* **14**(1), 28–44 (2018)
5. Pickin, C., Young, K.: Evaluation of cold metal transfer (CMT) process for welding aluminium alloy. *Sci. Technol. Weld. Joining* **11**(5), 583–585 (2006)
6. Zhang, H., Feng, J., He, P.: Interfacial phenomena of cold metal transfer (CMT) welding of zinc coated steel and wrought aluminium. *Mater. Sci. Technol.* **24**(11), 1346–1349 (2008)
7. Chen, S.-B., Wu, J.: *Intelligentized Methodology for Arc Welding Dynamical Processes*. Springer, Heidelberg (2009). <https://doi.org/10.1007/978-3-540-85642-9>

8. Chen, S., Lv, N.: Research evolution on intelligentized technologies for arc welding process. *J. Manuf. Process.* **16**(1), 109–122 (2014)
9. Yong Jie, P., et al.: Application of multi-agent systems in welding flexible manufacturing system. *Trans. China Weld. Inst.* **5**, 23 (2002)
10. Piao, Y.J., Zhu, Z.Y., Chen, S.B.: Multi-agent collaboration control for multi-manipulator WFMS. *Acta Simulata Systematica Sinica* **16**(11), 2571–2574 (2004)
11. Zhang, L.X., et al.: Agent-based modeling and control of remote robotic welding system. In: Tarn, T.J., Chen, S.B., Zhou, C. (eds.) *Robotic Welding, Intelligence and Automation. Lecture Notes in Control and Information Sciences*, vol. 362, pp. 187–194. Springer, Heidelberg (2007)
12. Kong, M., Chen, S.: Al alloy weld pool control of welding robot with passive vision. *Sens. Rev.* **29**(1), 28–37 (2009)
13. Wang, J.J., Lin, T., Chen, S.B.: Obtaining weld pool vision information during aluminium alloy TIG welding. *Int. J. Adv. Manuf. Technol.* **26**(3), 219–227 (2005)
14. Xu, Y., et al.: Computer vision technology for seam tracking in robotic GTAW and GMAW. *Rob. Comput.-Integr. Manuf.* **32**, 25–36 (2015)
15. Lv, N., et al.: Automated control of welding penetration based on audio sensing technology. *J. Mater. Process. Technol.* **250**, 81–98 (2017)
16. Na, L.V., Gu, F., Yan-ling, X., Hui, Z., Shan-ben, C., Ju-jia, Z.: Real-time monitoring of welding path in pulse metal-inert gas robotic welding using a dual-microphone array. *Int. J. Adv. Manuf. Technol.* **90**(9–12), 2955–2968 (2016). <https://doi.org/10.1007/s00170-016-9571-7>
17. Huang, Y., et al.: EMD-based pulsed TIG welding process porosity defect detection and defect diagnosis using GA-SVM. *J. Mater. Process. Technol.* **239**, 92–102 (2017)
18. Huang, Y., et al.: Investigation of porosity in pulsed GTAW of aluminum alloys based on spectral and X-ray image analyses. *J. Mater. Process. Technol.* **243**, 365–373 (2017)
19. Zhang, Z., Kannatey-Asibu, E., Chen, S., Huang, Y., Xu, Y.: Online defect detection of Al alloy in arc welding based on feature extraction of arc spectroscopy signal. *Int. J. Adv. Manuf. Technol.* **79**(9–12), 2067–2077 (2015). <https://doi.org/10.1007/s00170-015-6966-9>
20. Zhang, Z., et al.: Multisensor-based real-time quality monitoring by means of feature extraction, selection and modeling for Al alloy in arc welding. *Mech. Syst. Signal Process.* **60**, 151–165 (2015)
21. Chen, S.: Research evolution on intelligentized technologies for robotic welding at SJTU. In: *Robotic Welding, Intelligence and Automation*, pp. 3–14. Springer, Heidelberg (2011). https://doi.org/10.1007/978-3-642-19959-2_1
22. He, Y., et al.: Fault correction of algorithm implementation for intelligentized robotic multi-pass welding process based on finite state machines. *Rob. Comput. Integr. Manuf.* **59**, 28–35 (2019)
23. Zhou, H., et al.: Mixed logic dynamic model for the hybrid characteristics of the dual robotic welding process and system. In: 2016 IEEE Workshop on Advanced Robotics and its Social Impacts (ARSO) (2016)
24. Ma, H., Chen, S.: Mixed logical dynamical model for robotic welding system. In: Tarn, T.J., Chen, S.B., Fang, G. (eds.) *Robotic Welding, Intelligence and Automation*, pp. 123–128. Springer, Heidelberg (2011). https://doi.org/10.1007/978-3-642-19959-2_15
25. Ma, H., et al.: Mixed logical dynamical model for back bead width prediction of pulsed GTAW process with misalignment. *J. Mater. Process. Technol.* **210**(14), 2036–2044 (2010)
26. Ma, H., et al.: Mixed logical dynamical model of the pulsed gas tungsten arc welding process with varied gap. *Proc. Inst. Mech. Eng. Part I J. Syst. Control Eng.* **225**(3), 270–280 (2011)
27. Chen, S.B., et al.: Robotic welding systems with vision-sensing and self-learning neuron control of arc welding dynamic process. *J. Intell. Rob. Syst.* **36**(2), 191–208 (2003)

28. Yong, Z., et al.: Weld pool image processing algorithm for seam tracking of welding robot. In: *Industrial Electronics & Applications* (2011)
29. Shen, H.Y., et al.: Research on weld pool control of welding robot with computer vision. *Ind. Robot.* **34**(6), 467–475 (2007)
30. Gonzalez, R.C., Woods, R.E.: *Digital Image Processing*, 3rd edn. (2007)
31. Xu, Y., Fang, G., Chen, S., Zou, J.J., Ye, Z.: Real-time image processing for vision-based weld seam tracking in robotic GMAW. *Int. J. Adv. Manuf. Technol.* **73**(9–12), 1413–1425 (2014). <https://doi.org/10.1007/s00170-014-5925-1>
32. Zheng, R., et al.: Measurement of laser welding pool geometry using a closed convex active contour model. *Meas. Sci. Technol.* **25**(3), 116–121 (2014)
33. Caselles, V., Kimmel, R., Sapiro, G.: Geodesic active contours. *Int. J. Comput. Vision* **22**(1), 61–79 (1997)
34. Bemporad, A., Morari, M.: Control of systems integrating logic, dynamics, and constraints. *Automatica* **35**(3), 407–427 (1999)



Deep Learning Based Robot Detection and Grinding System for Veneer Defects

Xuewu Wang¹(✉), Zhongwang Zhang¹, and Huafeng Liu²

¹ Key Laboratory of Advanced Control and Optimization for Chemical Processes of Ministry of Education, East China University of Science and Technology, Shanghai 200237, China
wangxuew@ecust.edu.cn

² Shanghai Value Automation Technology Co., Ltd., Shanghai 200233, China

Abstract. To obtain desired wood appearance, it is necessary to grind the defects in the wood veneer. Traditional manual grinding method is time consuming and laborious. Therefore, the method using industrial robot combined with vision detection system is proposed to improve the processing efficiency. Based on the object detection network RetinaNet, the detection model is trained to detect the defects of different categories in the whole veneer. The pixel coordinates of detected defects will be transformed into robot coordinates, and PLC uses these coordinate values to control the robot for grinding. Based on the data set of veneers, experiments are conducted on the anchor boxes parameters and the weight factor of Focal Loss. The results show that the model has high recognition accuracy in the tested veneer data.

Keywords: Veneer defects · Deep learning · Industrial robot · Object detection

1 Introduction

The furniture industry has higher and higher requirements for the quality of wooden products, the defects in the veneer need to be grinded in the early stage of the process. In the traditional processing process, it mainly relies on the worker to look for defects with his eyes and to use a grinding tool for grinding. Long time in such a working environment will cause visual fatigue and affect worker's judgment, and the powder produced by grinding will seriously affect the respiratory health of workers. Therefore, the vision based grinding system of industrial robots has a good application value, deep learning algorithms promote the wide application of image processing in this field.

As early as the 1950s, Frank Rosenblatt [1] established the earliest perceptron model, one of the simplest neural networks, which laid a theoretical foundation for the subsequent development. With the continuous development of scientific computing technology, the multi-layer perceptron model, BP algorithm [2] and other theories also continuously promote the research process of neural network. Around 2010, with the proposal of SGD [3], the model training method of neural network has been continuously improved, deep learning research enters a boom. Companies and educational institutions around

the world are engaged in deep learning research, and the research direction is becoming more diversified. Nowadays, deep learning has been widely applied in the fields of image recognition, text recognition, Voice recognition and so on. Different from traditional image processing algorithms that extract features such as edges, corners and colors from images, deep learning networks generate feature maps of different scales and depths based on original images through multi-layer convolutional neural networks. These feature maps represent various abstract features of the original image. With the deepening of the network level, it can express more image information. Different algorithms use different mechanisms to process features, which can achieve tasks such as classification of complex images, object detection, and image segmentation [4].

The thickness of the veneer produced after ring cut of the log is only about 0.1 mm, and there are many types of defects on the surface. Figure 1 shows common defects such as knot, black line, black line group, and hardwood. Since these defects are formed naturally, the characteristics of those defects can change vary widely. The traditional image processing algorithm may not have good robustness. A study of the defect images based on deep learning algorithm, make full use of the ability of deep neural networks to learn the abstract features of the target, and improve the generalization ability of the recognition algorithm. The neural network model is based on RetinaNet, the network structure is relatively simple, and its unique Focal loss [5] function can reduce the impact of category imbalance. Using the trained network model to detect the bounding box of the defect in the picture. According to the grinding method, the bounding box is converted into grinding points and the it's pixel coordinates are converted into engineering coordinates. The coordinates are output to the PLC to control the robot arm to polish the veneer.

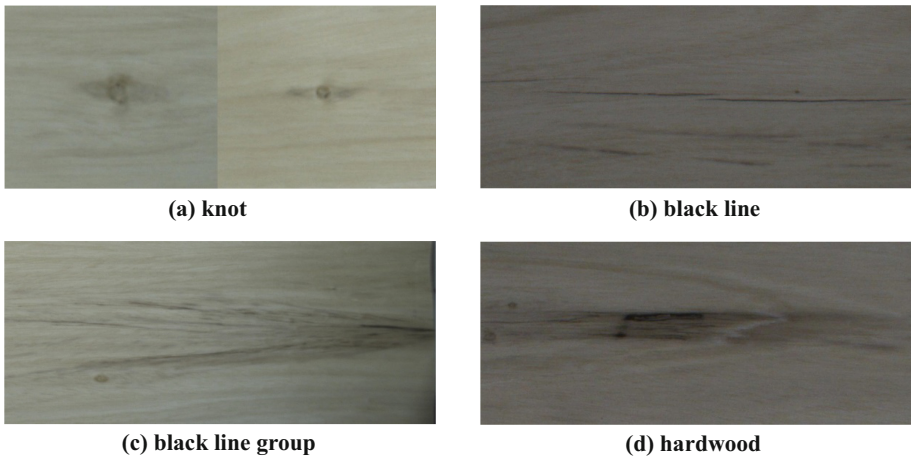


Fig. 1. Different types of veneer defects.

The content of the paper is arranged as follows: First introduce the architecture of robot detection and grinding system for veneer defects, including the main hardware units in the system and the image processing software system. Then the working process of the system is explained, and the part of image preprocessing and hand-eye calibration are

introduced in detail. Introduced the principle of RetinaNet used in this study, based on the RetinaNet algorithm and using the veneer defect dataset for model training experiments. Finally, the detection model is optimized according to the characteristics of the data set, and the experimental results are summarized.

2 System Architecture

The system is composed of hardware part and software part. The hardware part includes grinding platform equipment and industrial robot system, and the software part includes image processing algorithm and PLC control program. The specific system composition is shown in Fig. 2, and Table 1 shows the specifications of some equipment.

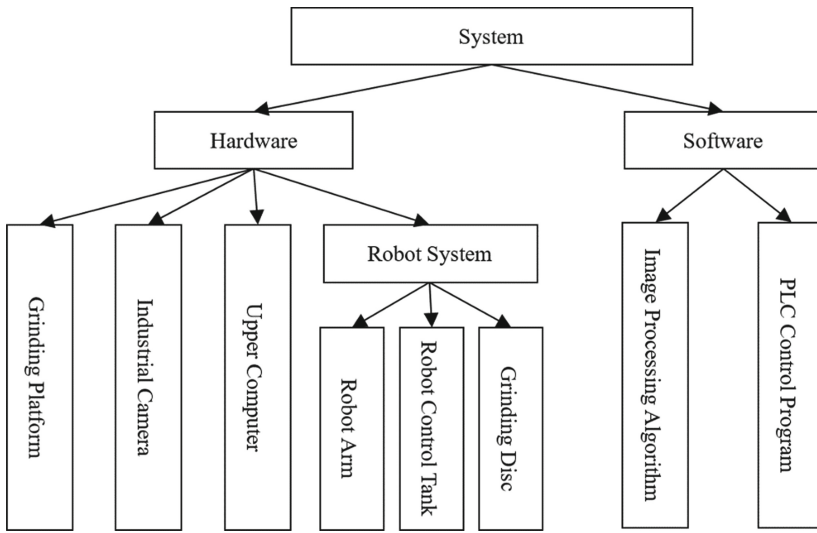


Fig. 2. System components.

Table 1. Models and specifications of some equipment.

Hardware	Specification	
Camera	Daheng MER-1810-21U3C	
PLC	Siemens S7-400	
Robot arm	FANUC M-10IA/8L	
Upper computer	CPU	Intel i5-6500
	Memory	8 G
	GPU	RTX 2080

Because the length of the veneer is very long, it is difficult to take a complete and clear picture of veneer with a single industrial camera. Therefore, two cameras are used

to shoot the left and right parts of the veneer at the same time to ensure that the entire veneer can be captured. In order to make the captured image bright and clear, which is good for image processing, a strip LED light source is installed above the grinding table (Fig. 3).



Fig. 3. Camera and light source layout.

Image processing system includes image processing algorithm and GUI (Graphical User Interface). Because the defect features, which in the picture of veneer, are complex and inconstant. Using traditional image processing methods cannot achieve better recognition results. Therefore, the image processing algorithm is an object detection model trained on RetinaNet. For veneer pictures collected from wood manufacturers, use horizontal flipping, vertical flipping [6] and other methods for data augmentation. Divide the data into training set and validation set proportionally. Use the training set to optimize the network parameters and train the optimal network model based on the evaluation effect of the validation set. In addition to the network model, the complete image processing algorithm also includes image preprocessing and coordinate transformation. The GUI of the image processing system is developed using PYQT [7], the following functions are mainly realized: of the image processing system is developed using PYQT, the following functions are mainly realized: Real-time display of the veneer on the grinding table and the effect of image processing; display information about defects that have been identified in the veneer.

3 System Workflow

When the system is actually running, the entire workflow is roughly shown in Fig. 4. After the camera receives the pulse signal sent by the PLC, it transmits the collected color image to the upper computer. The pre-processed image is used as the input of the neural network model, and the output is converted into robot coordinates and sent to the PLC to control the robot for grinding.

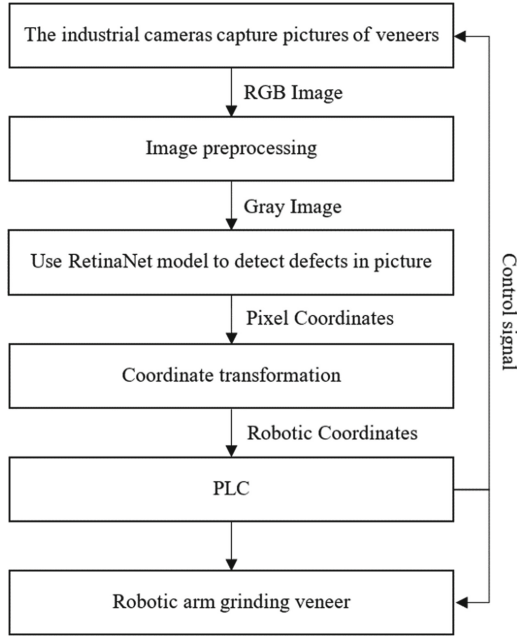


Fig. 4. Workflow of robot detection and grinding system for veneer defects.

3.1 Image Preprocessing

The image preprocessing process is shown in Fig. 5. The original image collected by the camera includes the environment outside the veneer range, and the detection object of the convolutional neural network is the entire picture, so the veneer part of the image should be cropped first. By observing the data, it can be found that most of the veneer defect features are related to its image texture information. And the background colors of different batches of data are also different. In order to remove the influence of the background colors during the training process, the images are converted into grayscale images. During the experiment, it was discovered that due to the large resolution of the images in the training data set, a large number of intermediate parameters would be generated during the training process. As a result, the training speed slows down and consumes a lot of video memory, and may even cause the training process to be interrupted. Under the condition of undistorted, it is necessary to downsample the image using bilinear interpolation [8].



Fig. 5. Image preprocessing process.

3.2 Hand-Eye Calibration and Coordinate Transformation

Since the position of the defect in the image is its pixel coordinates, the robot needs to receive the coordinates of the robot coordinate system during the grinding process. So after the grinding platform and robot are installed, the robot needs to be calibrated to find the transformation relationship of the defect from the image to the robot coordinate system. During the grinding process, the grinding tool at the end of the robotic arm only needs to work on the surface of the grinding table. Therefore, it is assumed that the XOY plane in the robot coordinate system is parallel to the grinding table, so the Z of all the points on the veneer is the same value. In this way, the transformational relation can be regarded as a coordinate conversion from one plane to another (Fig. 6). Perspective transformation [9] can project the image on a new picture plane. In this project, the point (u, v) on the pixel plane is projected to the point (x, y) on the plane of the grinding table. The transformation is given by the equation:

$$[x, y, 1] = [u, v, 1] \begin{bmatrix} a_{11} & a_{12} & a_{13} \\ a_{21} & a_{22} & a_{23} \\ a_{31} & a_{32} & a_{33} \end{bmatrix} \tag{1}$$

The calibration process is roughly as follows: mark four points on the veneer and place it on the grinding table, record the pixel coordinate value of each point. Use the FlexPendant to control end-of-arm tooling of robot to touches these four points respectively, and record the robot coordinate value of the marked points. The perspective transformation matrix M is solved by Eq. 1.

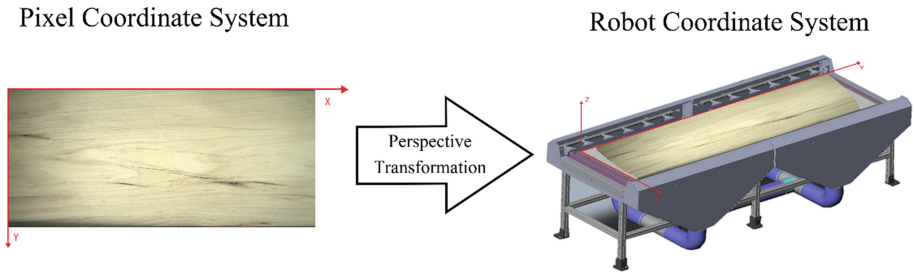


Fig. 6. Schematic diagram of coordinate transformation.

4 Object Detection Algorithm Based on RetinaNet

Object detection is an algorithm that can predict the class of an object and mark the bounding box of the object in the image, including traditional methods and deep learning methods. Traditional object detection algorithms are mostly based on sliding window mechanism for region selection. Algorithms such as SIFT [10] are commonly used to extract image features, and then classifiers such as SVM [11] are used for classification. However, this method has high time complexity and is not robust to images with highly

complex features. In recent years, with the development of deep learning, breakthroughs have been made in the application of object detection. Mainly divided into two categories, one is a two-stage algorithm based on region proposal; the other is a one-stage algorithm that uses an end-to-end neural network model to predict category and location at the same time. One-stage is better than two-stage in recognition speed but not in accuracy. The RetinaNet neural network used in this paper is a one-stage target detection algorithm. It uses the focal loss function to successfully solve the “category imbalance” problem in the one-stage algorithm. Its basic structure is shown in Fig. 7.

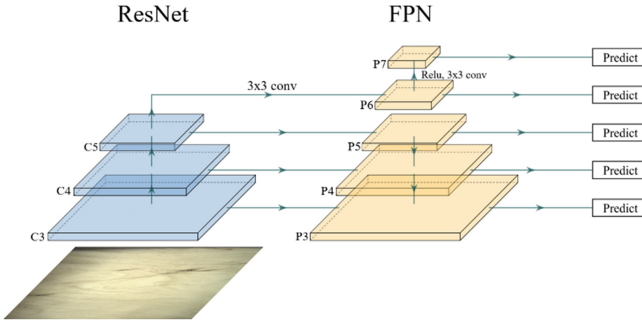


Fig. 7. Architecture of RetinaNet.

4.1 FPN

The general object detection algorithm only uses the top-level feature map as the predicted feature vector. Although this method can obtain rich semantic information in the picture, it cannot accurately locate objects of different scales. FPN [12] (feature pyramid networks) samples the image into feature maps of different scales through convolution, and each feature map can correspond to the object features of different scales in the image. Based on this feature of RetinaNet, the C3 – C5 layer of the backbone network ResNet [13] is used as a bottom-up route, and bilinear interpolation is used to upsample the C5 layer as a top-down route. The 1×1 convolution kernel is used to convolve the C3 – C5 feature maps to reduce its dimension, so that the feature maps of the same scale of the two routes can be fused, as shown in Fig. 7. P3 – P7 are feature pyramids, where P6 and P7 are obtained by convolution of C5 and P6 respectively, and the feature of every scale will be predicted independently.

4.2 Bounding Box Regression

The task of object detection is to identify and locate multiple targets appearing in the image. Anchor boxes [14] are often used as a benchmark to execute bounding box regression to determine the predicted bounding box of the final target. Based on a pixel in the image, a group of anchor boxes with N scale ratios and M aspect ratios can be listed. For each $W \times H$ feature map output by FPN, $W \times H \times N \times M$ anchor boxes can be

listed based on the basic area. In the training process, it is necessary to count the anchor boxes around each sample target, and mark them as a certain category or background according to the IOU value between anchor box and its nearby target. According to Eq. 2 [14], the offset (t_x , t_y , t_w , t_h) between the anchor box and the true box is calculated as the value of backpropagation. For each layer of feature maps output by FPN, connect two FCN [15], and the dimensions of the feature maps of the output layer are $K \times A$ and $4 \times A$ (K is the number of categories, A is the number of anchor boxes). SmoothL1 [16] (Eq. 3) loss function is used for bounding box regression training.

$$t_x = \frac{(G_x - P_x)}{P_w}, t_y = \frac{(G_y - P_y)}{P_h}, t_w = \log \frac{G_w}{P_w}, t_h = \log \frac{G_h}{P_h} \quad (2)$$

$$\text{SmoothL1}(x) = \begin{cases} 0.5x^2 & \text{if } |x| < 1 \\ |x| - 0.5 & \text{otherwise} \end{cases} \quad (3)$$

4.3 Focal Loss Function

In the object detection task, the two-stage algorithm performs better than the one-stage algorithm in detection accuracy. The reason is that two-stage first uses RPN to find some unclassified bounding boxes that may include true targets, and then performs bounding box regression and classification. In the one-stage algorithm, all anchor boxes are used as training samples, which greatly increases the number of anchor boxes that are easily classified as negative samples. It will reduce the proportion of positive samples when calculating loss, so that the model is not optimized in the expected direction. The focal loss balances this problem by adding weight factor based on the cross-entropy loss function. The formula is given by the equation [5]:

$$\text{FL}(P_t) = -\alpha_t(1 - P_t)^\gamma \log(P_t) \quad (4)$$

P_t and α_t are the estimated probabilities and balance coefficients of each category respectively. When the target is classified wrong during training ($P_t \rightarrow 0$), the loss is not greatly affected; on the contrary, it also reduces the influence of easily classified samples on loss calculation. The model is optimized in the direction of class balance. In this study, this greatly reduces the impact of a small number of defects on model optimization.

5 Experiments and Analysis

5.1 Experiment by Traditional Image Processing

Before using deep learning algorithms, try to use traditional image processing algorithms to process picture of veneer. First, adjust the brightness, contrast and gamma parameters of the picture to make the dark defects in the picture more obvious; then histogram equalization is used to enhance the global contrast of the image and convert it into a binary image; finally use morphological operations [6], closing and corrosion are used to extract the defects in the image. Figure 8 shows the effect of the image processing channel. For deep-colored defects, the segmentation effect is considerable. But the contrast color between knots and background is low, many knots can't be recognized. In pictures under different lighting conditions, the segmentation effect is quite different, and the robustness of the algorithm is poor.

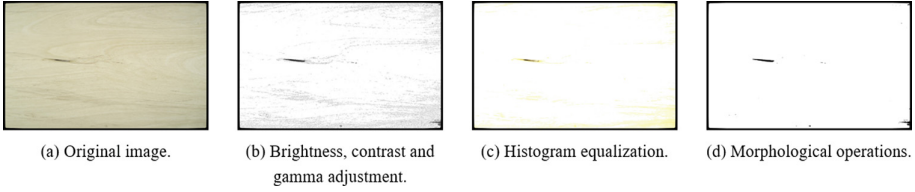


Fig. 8. Image processing flow of traditional method.

5.2 Experiments Based on RetianNet

(1) Data set and model training

Before the experiment, I used an industrial camera to collect about 400 original veneer pictures. Analyze the distribution of defects in these pictures, augment image data by vertical flipping or horizontal flipping. The augmented data set contains 929 images, which are divided into training set and test set at a ratio of 4:1, and the data is labeled by Labelme [17]. The size of the picture collected by the camera is 4985×3655 . In order to save video memory, the data is downsampled to 1/4 of the original size and Set batch_size to 1. The learning rate changes during training as shown in Eq. 5 and the curve where the training loss converges to 0 is shown in Fig. 9.

$$Lr = \begin{cases} epoch * 10^{-5} & epoch \leq 10 \\ 0.0001 & epoch > 10 \end{cases} \quad (5)$$

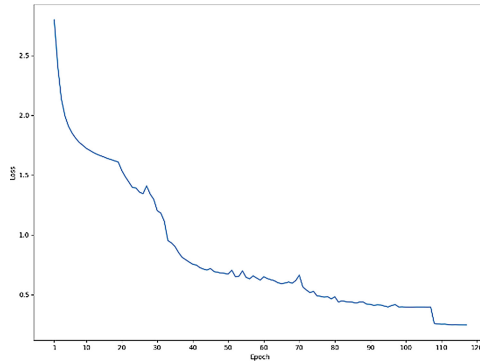


Fig. 9. Convergence of losses from training process

(2) Experiment on anchor boxes

During the training process, there will be cases where the loss of some data is abnormal. After processing these pictures separately, it is found that the number of anchor

boxes marked as foreground near the black line defect is small or even zero. Therefore, it is expected to set reasonable parameters of anchor boxes for the data set through experiments. In order to enumerate a sufficient number of anchor boxes for each defect in the data set, the experiment uses different parameters to generation anchor boxes. Keep $scale_ratios$ as $(1, 2^{\frac{1}{3}}, 2^{\frac{2}{3}})$ and $anchor_areas$ as $(20, 40, 80, 160, 320)$ unchanged, adjust the $aspect_ratios$ to different combinations. Calculate the average number of the anchor boxes marked as the class near each defect in each class of defect. The experimental results are given in Table 2. Experimental results show that only anchor boxes with a large aspect ratio can be marked as foreground boxes of black line. So set $aspect_ratios$ to $[1, 4, 5]$, indicates that the aspect ratio of the anchor boxes generated by the RPN during the training process is 1, 4, and 5. After modification, the loss value dropped normally during training. And the model can converge quickly.

Table 2. The mean number of anchor boxes near each type of defect.

Aspect_ratios	[1/2, 1, 2]	[2, 1, 3]	[3, 1, 4]	[2, 1, 5]	[5, 1, 6]
Knot	5.62	7.56	5.46	4.67	3.87
BL ¹	0.33	2.33	5.27	6.98	5.86
BLG ²	9.82	17.08	15.1	11.88	7.28
HW ³	9.48	17.51	15.91	11.73	6.44

1 Black line. 2 Black line group. 3 Hardwood.

(3) Experiment on weight factor

When the loss value didn't decrease during the training process. After testing the model, it is found that the knots have a good recognition effect. But only a few defects of other classes can be recognized. From the perspective of data distribution, compared with other classes of defects, the knot belongs to the category of easy classification. Try to adjust the weight factor of the focal loss function from 0.25 to 0.3, and retrain the model. The model is evaluated based on the verification data set. Figure 10 is the PR curves [18] of the detection results from two experiments. It can be seen from Fig. 10-a that the knot has a good recognition effect. And Fig. 10-b, c, d show that the number of other classes of defects recognized has increased significantly. After adjusting α , the learning performance of the model is significantly better than before. The average accuracy (AP) detected by the models is shown in Table 3.

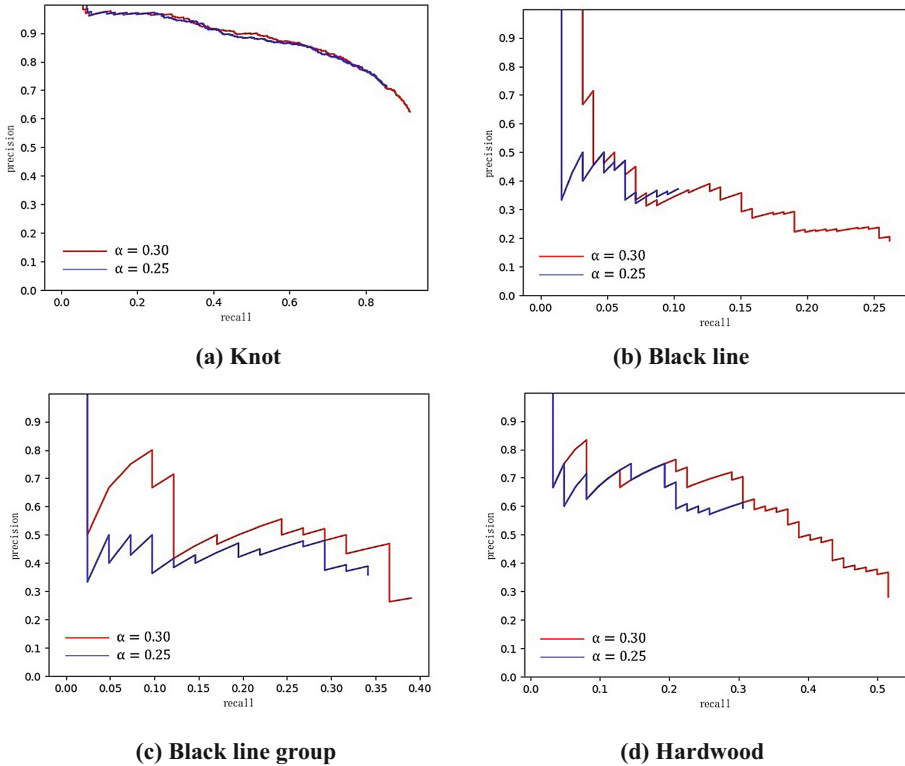


Fig. 10. PR curves of the detection results.

Table 3. Average accuracy of detections.

α	AP				
	Knot	BL ¹	BLG ²	HW ³	mAP
0.25	0.77	0.34	0.22	0.26	0.40
0.30	0.81	0.41	0.34	0.31	0.47

1 Black line. 2 Black line group. 3 Hardwood.

5.3 Analysis

Experimental results show that, compared with traditional image processing algorithms, the RetinaNet-based object detection model can effectively classify defects and detect infrequent defects. For the data set of this study, changing the generation parameters of the anchor boxes can make the model better training. After adjusting the weight factor of focal loss, the recognition effect is enhanced for defects with extreme shapes and a small number. The final detection effect of the model can meet the grinding requirements of the production workshop, and it is deployed to the industrial robot system. For the

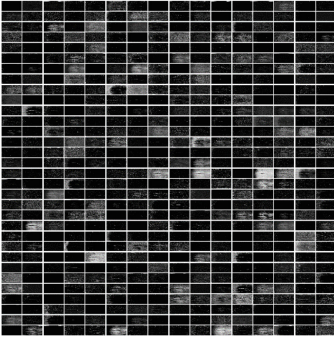
entire image processing channel, the picture after preprocessing and feature extraction is shown in the Fig. 11. For infrequent and new classes, the model's generalization ability can be enhanced by expanding the data set and retraining the model.



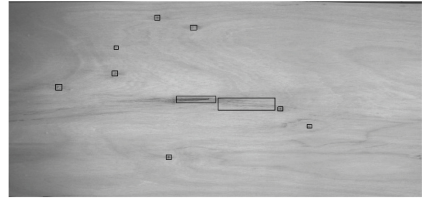
(a) Original image.



(b) Preprocessed image.



(c) Feature maps in convolutional neural networks.



(d) Image after detection.

Fig. 11. The effect of the picture in the image processing process, (c) is part of the feature maps of ResNet.

6 System Implementation

The system implements the functions of photographing, identifying and grinding the veneer. The whole scene of the system is shown in Fig. 12 and the design of GUI is shown in Fig. 13. When the robot system and the host computer are started, the PLC control system is also turned on. The operator clicks the “Open System” button in the GUI, the communication link will be established between the upper computer and PLC by TCP protocol, and system will turn on the camera and load the object detection model. At the beginning of a grinding period, the camera takes an image of veneer, which will be preprocessed before input neural network model. Use ResNet to extract feature maps

and RPN to find high score boxes. The NMS [19] is used to filter out the bounding boxes of predicted defects. For all bounding boxes of defects, the transformation matrices M1 and M2 need to be used to convert pixel coordinates into robot coordinates. For knots, the center of the bounding box is used as the grinding point; for other defects, the horizontal center line of the bounding box is used as the grinding track. Calculate the grinding points of all defects and send them to the PLC to control the robot arm.

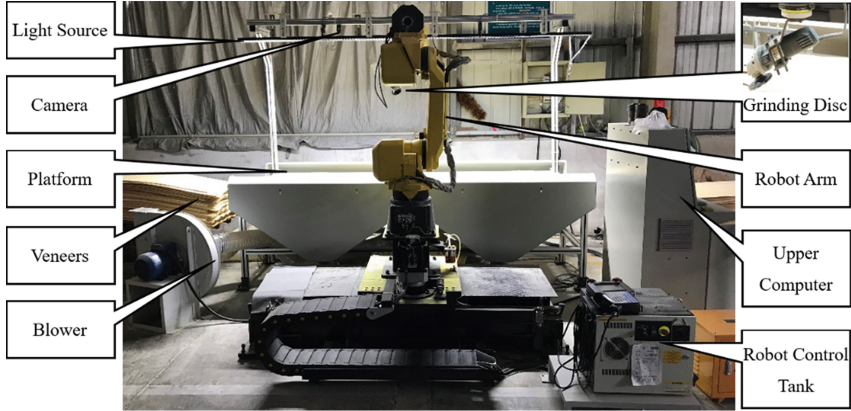


Fig. 12. Full view of system.

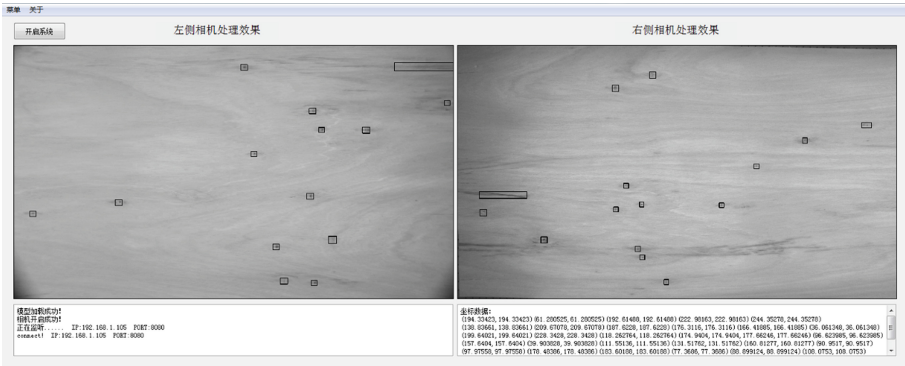


Fig. 13. Layout of GUI.

7 Conclusion

For the task of grinding veneer defects in the wood industry, this paper proposes a method based on vision detection combined with industrial robot to automatically grind veneer. Based on the experiments on anchor parameter and the weight factor of focal loss, an

optimized model for the detection of veneer defects was obtained, and a method for hand-eye calibration using perspective transformation was applied. Then, a complete robot detection and grinding system for veneer defects was implemented. From the experimental results, deep learning performs better than traditional methods on detecting veneer pictures. It has profound significance for the application of intelligent manufacturing to the wood industry, and proves the effectiveness of deep learning in the industrial field and its huge development potential.

Acknowledgment. The authors appreciate the support of National Natural Science Foundation of China (62076095, 61973120).

References

1. Rosenblatt, F.: The perceptron: a probabilistic model for information storage and organization in the brain. *Psychol. Rev.* **65**(6), 386–408 (1958)
2. Rumelhart, D.E., Hinton, G.E., Williams, R.J.: Learning representations by back propagating errors. *Nature* **323**(6088), 533–536 (1986)
3. Bottou, L.: Stochastic gradient descent tricks. *Lect. Notes Comput. Sci.* **7700**(1), 437–478 (2012)
4. Jiao, L., Zhao, J.: A survey on the new generation of deep learning in image processing. *IEEE Access* **7**, 172231–172263 (2019)
5. Tsung-Yi, L., Priya, G., Ross, G., Kaiming, H., Piotr, D.: Focal loss for dense object detection. *IEEE Int. Conf. Comput. Vis. (ICCV)*. **2017**, 2999–3007 (2017)
6. Gonzalez, R.C., Woods, R.E.: *Digital Image Processing*. Publishing House of Electronics Industry; Pearson Education, London (2002)
7. Boudewijn, R.: Python's PyQt toolkit. *Dr. Dobb's J.* **26**(1), 88 (2001)
8. Smith, P.R.: Bilinear interpolation of digital images. *Ultramicroscopy* **6**(2), 201–204 (1981)
9. Yuanjun, H.: Perspective and its projection transformation. *J. Comput. Aided Des. Comput. Graph.* **04**, 734–739 (2005)
10. Zhou, H., Yuan, Y., Shi, C.: Object tracking using SIFT features and mean shift. *Comput. Vis. Image Underst.* **113**(3), 345–352 (2009)
11. Moranduzzo, T., Melgani, F.: A sift-SVM method for detecting cars in UAV images. *IEEE Int. Geosci. Remote Sens. Symp. (IGARSS)*. **2012**, 6868–6871 (2012)
12. Lin, T.Y., Dollár, P., Girshick, R., et al.: Feature pyramid networks for object detection. In: *IEEE Conference on Computer Vision and Pattern Recognition (CVPR)* (2017)
13. He, K., Zhang, X., Ren, S., et al.: Deep residual learning for image recognition. In: *IEEE Conference on Computer Vision & Pattern Recognition*. IEEE Computer Society (2016)
14. Ren, S., He, K., Girshick, R., et al.: Faster R-CNN: towards real-time object detection with region proposal networks. *IEEE Trans. Pattern Anal. Mach. Intell.* **39**(6), 1137–1149 (2017)
15. Long, J., Shelhamer, E., Darrell, T.: Fully convolutional networks for semantic segmentation. *IEEE Trans. Pattern Anal. Mach. Intell.* **39**(4), 640–651 (2015)
16. Girshick, R.: Fast R-CNN. In: *International Conference on Computer Vision (ICCV)* (2015)
17. Russell, B.C., Torralba, A., Murphy, K.P., et al.: LabelMe: a database and web-based tool for image annotation. *Int. J. Comput. Vis.* **77**(1–3), 157–173 (2008)
18. Zhi-Hua, Z.: *Machine Learning*. Tsinghua University Press, Beijing (2016)
19. Neubeck, A., Gool, L.J.V.: Efficient non-maximum suppression. In: *International Conference on Pattern Recognition*. IEEE Computer Society (2006)

Author Index

C

Chen, Huabin, [56](#)
Chen, Shanben, [56](#)
Chen, Xiaohua, [43](#)
Chen, Zhonghao, [3](#)
Commins, Philip, [3](#)
Cui, Yanxin, [23](#)

F

Fan, Ding, [43](#)

H

He, Fengyang, [3](#)
He, Yinshui, [56](#)

L

Li, Yuxing, [3](#)
Liu, Huafeng, [82](#)

M

Mu, Haochen, [3](#)

P

Pan, Zengxi, [3](#)

S

Shi, Yonghua, [23](#)
Shi, Yu, [43](#)

W

Wang, Xuewu, [82](#)

X

Xia, Chunyang, [3](#)

Z

Zhang, Hulong, [43](#)
Zhang, Zhongwang, [82](#)
Zhou, Hao, [56](#)
Zhu, Ming, [43](#)